University of Alberta

Hybrid-Kinetic Modelling of Space Plasma with Application to Mercury

by

Jan Paral

A thesis submitted to the Faculty of Graduate Studies and Research in partial fulfillment of the requirements for the degree of

Doctor of Philosophy

Department of Physics

Spring 2013

Edmonton, Alberta

To

my parents

Abstract

A planet's magnetosphere is often very dynamic, undergoing large topological changes in response to high speed (∼400km/s) solar wind intervals, coronal mass ejections, and naturally excited plasma wave modes. Plasma waves are very effective at transporting energy throughout the magnetosphere, and are therefore of interest in the context of the coupling between solar wind and magnetosphere. Of relevance to this thesis is Kelvin-Helmholtz macro-instability. Kelvin-Helmholtz instability (KHI) is excited by shear of the flows. KHI is commonly observed at equatorial regions of the magnetopause where fast flowing magnetosheath plasma may interact with slow bulk velocities of magnetospheric plasma. The instability is responsible for exciting shear Alfvén waves which (at Earth) may be detected using the ground based magnetometers located at latitude of excited field lines. This thesis uses numerical modelling to understand and to explain the generation and propagation of the KHI in Mercury's magnetosphere. The instability is initiated close to the planet and convectively grows while being transported along the tail. When the wave amplitude reaches a nonlinear stage, the structure of the wave becomes complex due to the wrapping of the plasma into the vortex. A vortex structure is typical for KHI and it is used for identifying the wave in the data from satellites. The instability commonly occurs at the dawn or dusk flank magnetopause (MP) of Earth with approximately the same probability. But the data from NASA's MESSENGER spacecraft, currently in the orbit of the planet Mercury, suggest a strong asymmetry in the observations of KHI. It is shown that the KHI initiated near the subsolar point evolves into large-scale vortices propagating anti-sunward along the dusk-side MP. The simulations are in agreement with the third flyby of the MESSENGER spacecraft, where saw-tooth oscillations in the plasma density, flow, and magnetic field were observed. The observed asymmetry in the KHI between dawn and dusk is found to be controlled by the finite gyro-radius of ions, and by MP pressure gradients and the large-scale solar wind convection electric field.

Acknowledgements

I would like to acknowledge three people: my supervisor Prof. Robert Rankin, my wife Dr. Eunah Lee and my son Luca L. Paral. They helped me a great deal by providing me with their knowledge and by giving me moral support when needed. Many other people helped me throughout difficult times when I was working on my Ph.D. project and I believe they do not require specific mention of their name because they know who they are. My colleagues who helped me with the technical aspects of my work are acknowledged in the published papers and in the appropriate chapters.

Table of Contents

List of Tables

List of Figures

Chapter 1

Introduction

In this chapter we overview the basic space plasma physics which is relevant to work in this thesis. We give an overview of basic definition of three requirements for gas to be considered a plasma. We will review single particle motion in external electromagnetic (EM) fields which will provide insight into various trajectories of charged particles. We will use this information for analysis of particle-in-cell particle tracing numerical codes which use Lorentz force for moving particle. We will briefly review linear kinetic theory as a tool for data interpretation of wave-particle interactions. In the last sections, two the most relevant waves are surveyed: Kelvin-Helmholtz Instability and Electromagnetic Ion Cyclotron wave.

1.1 Space Plasma Physics

Plasma is a gas of charged particles. The charge distribution is not in equilibrium but in the following chapters we will assume that the physical system contains equal number of positive and negative charges so that on temporal and spatial scales of our interest plasma is neutral. In other words, sum of number densities n_s over all species times charge q_s of a species s is equal zero:

$$\sum_s n_s q_s = 0. \tag{1.1}$$

At what temporal and spatial scales the above condition is valid can be quantified by the following plasma criteria.

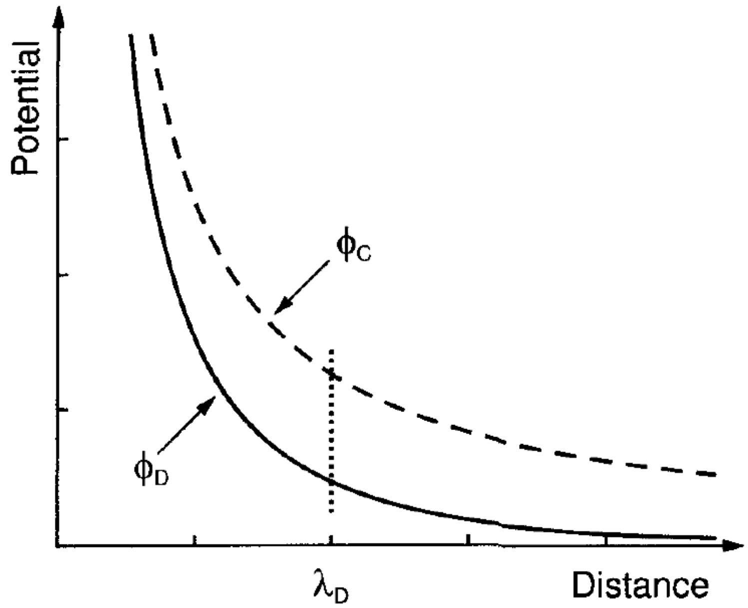

Figure 1.1: A difference between Coulomb and Debye shielding adopted from *Baumjohann and Treumann* [1996].

Spatial Scales

The potential of a single particle of charge q is given by the Coulomb potential

$$\Phi_c = \frac{q}{4\pi\epsilon_0 r}, \tag{1.2}$$

with ϵ_0 being the permittivity of free space. In the situation where other charged particles are present with approximately equal number of positive and negative charges, the potential of particle becomes shielded and it takes the form of the Debye potential:

$$\Phi_D = \frac{q}{4\pi\epsilon_0 r} \exp\left(-\frac{r}{\lambda_D}\right). \tag{1.3}$$

The difference between Coulomb and Debye shielding is represented by Figure 1.1. Exponential function in the expression above is a result of extra charges in the vicinity of the particle and it describes a cut off of Coulomb potential for distances larger than Debye length λ_D defined as:

$$\lambda_D^2 = \frac{\epsilon_0 k_B T_e}{n_e e^2}, \tag{1.4}$$

where k_B, T_e, n_e and e are the Boltzmann constant, electron temperature, electron density and electric charge respectively. A typical spatial length of a quasi-neutral system must be greater than the Debye length:

$$\lambda_D \ll L. \tag{1.5}$$

This plasma requirement represents the first criterion.

Kinetic Energy

The second criterion defines the kinetic energy necessary for particle to freely move through the plasma. A particle's kinetic energy must be sufficiently high to overcome potential energy of the nearest neighbor. This criterion can be expressed using a number of particles inside the sphere of radius λ_D which must be more than one. The total number of particles inside the Debye sphere is called the plasma parameter:

$$\Lambda = n_e \lambda_D^3 \gg 1. \tag{1.6}$$

Temporal Scales

A plasma oscillates on a natural frequency as a result of the electric field caused by electrons disturbed by some external force, and particle's inertia acting against the electric field trying to restore the particle to its neutral position. The plasma frequency ω_{pe} is defined as

$$\omega_{pe}^2 = \frac{n_e e^2}{m_e \epsilon_0}. \tag{1.7}$$

The third condition of a plasma states that

$$\omega_{pe} \tau_n \gg 1, \tag{1.8}$$

where τ_n is average time between collisions of electrons and neutrals. This condition guarantees that the plasma is not dominated by collisions with neutral particles but free charges can freely move around affected only by electromagnetic fields. The condition is satisfied in most regions of space plasmas except at high altitudes of the atmosphere and in the lower ionosphere.

1.2 Single Particle Motion

In this section, we will briefly describe motion of charged particle in external electromagnetic field. Motion of particle is important for interpretation of results from particle tracing code which we will use for study of Mercury's exosphere as well as hybrid code. Both codes solve equation of motion described in this section to advance particles in time. Equation of motion of charged particle in electromagnetic field is called Lorentz force and it is given by

$$\mathbf{F} = q(\mathbf{E} + \mathbf{v} \times \mathbf{B}). \tag{1.9}$$

Force $\mathbf{F}$ acts on charged particle of velocity $\mathbf{v}$ and charge q in external electromagnetic fields $\mathbf{E}$ and $\mathbf{B}$. If one omit electric field then equation simplifies to $\mathbf{F} = q(\mathbf{v}\times\mathbf{B})$ and after solving for position, we arrive at equations which describe simple circular motion. Proton (electron) rotate in clockwise (anticlockwise) direction around magnetic field line, respectively. Gyration frequency Ω_g of particle is also called cyclotron frequency and it is given by

$$\Omega_g = \frac{|q|B}{m}. \tag{1.10}$$

The radius of gyration is a function of perpendicular velocity $v_\perp$, mass, absolute value of charge of the particle and magnitude of the magnetic field:

$$r_g = \frac{mv_\perp}{|q|B}. \tag{1.11}$$

Gyroradius r_g is an important factor in determining whether resolving full particle motion is necessary for a given physical problem or simpler approximation can be used (for example gyro-center approximation).

Particle Drifts

A general equation of motion averaged over a single gyro-period is given by

$$v_F = \frac{1}{\Omega_g}\left(\frac{\mathbf{F}}{m} \times \frac{\mathbf{B}}{B}\right), \tag{1.12}$$

which describes motion of the gyro-center when external force $\mathbf{F}$ is applied on a particle. Force $\mathbf{F}$ can be substituted by electric field, gradient B, polarization, gravitation and centrifugal forces to obtain guiding center drifts and associated currents. The only

E × B	$\mathbf{v}_E = \dfrac{\mathbf{E}\times\mathbf{B}}{B^2}$	
Polarization	$\mathbf{v}_P = \dfrac{1}{\omega_g B}\dfrac{d\mathbf{E}_\perp}{dt}$	$\mathbf{j}_P = \dfrac{n_e(m_i+m_e)}{B^2}\dfrac{d\mathbf{E}_\perp}{dt}$
Gradient	$\mathbf{v}_\nabla = \dfrac{mv_\perp^2}{2qB^3}(\mathbf{B}\times\nabla B)$	$\mathbf{j}_\nabla = \dfrac{n_e(\mu_i+\mu_e)}{B^2}(\mathbf{B}\times\nabla B)$
Curvature	$\mathbf{v}_R = \dfrac{mv_\parallel^2}{qR_c^2 B^2}(\mathbf{R}_c\times\mathbf{B})$	$\mathbf{j}_R = \dfrac{2n_e(W_{i\parallel}+W_{e\parallel})}{R_c^2 B^2}(\mathbf{R}_c\times\mathbf{B})$

Table 1.1: Summary of particle drifts and associated currents.

exception which does not generate current is $E \times B$ drift because its velocity is not dependant on sign of charge. The drifts of particle are summarized in Table 1.2 adopted from *Baumjohann and Treumann* [1996].

1.3 Solar Wind

Solar wind is a hot conducting plasma which originates from the Sun. It is ejected at enormous speeds of about 500 km/s. As the plasma propagates though the solar system its density and temperature decrease. Solar wind consists mainly of protons and electrons. The other species are also present with the most common being helium ions of approximately 5%. Interplanetary magnetic field (IMF) which originates from the Sun is frozen in the solar wind and is dragged outward by expanding plasma. Due to the rotation of the Sun, magnetic field forms a spiral-like topology called Parker's spiral. The typical parameters of solar wind are summarized in the following chapter.

Solar wind maintains stable plasma parameters with a near Maxwellian distribution function until it encounters obstacle in the form of inhomogeneity or a planet. An example of plasma parameters common in space are summarized in Fig. 1.2 which represents the frequency of data observations from WIND/SWE missions as a function of two solar wind parameters: anisotropy $A = T_\perp/T_\parallel$; and plasma beta $\beta_{\parallel p} = 2\mu_0 n k_B T/B^2$. Only the data with solar wind velocity $v_{sw} \leq 600$ km/s are considered. The lines on the graph represent the maximal growth rate for various plasma instabilities: ion cyclotron (solid); firehose (dashed); mirror (dotted) and oblique Alfvén firehose (dashed dotted) instabilities. We can clearly see the role of micro-instabilities on the system. Once plasma reach a marginally unstable state the

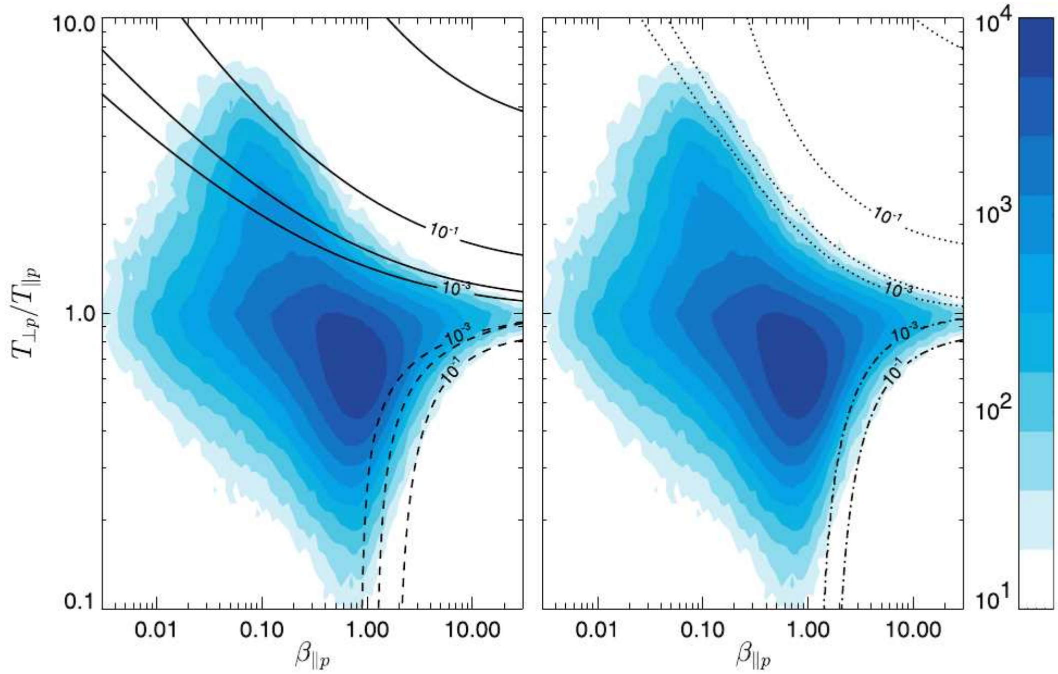

Figure 1.2: The number of measurements of solar wind WIND/SWE data (1995-2001) for the solar wind speed $v_{sw} \leq 600$ km/s on $\beta_{\parallel p}$ vs. A graph. The lines represent maximal growth rates (γ/Ω_p) for ion cyclotron (solid), firehose (dashed), mirror (dotted) and oblique Alfven firehose (dashed dotted) instabilities. Credit: *Hellinger et al.* [2006].

appropriate instability causes the plasma waves to grow and transport energy out of the unstable region. The loss of energy allows the system to return into the stable state. Fig. 1.2 represents only a simple model of solar wind protons but it demonstrates the role of instabilities on the evolution of solar wind. In magnetospheric plasma the dispersion relation becomes more complicated when the other species are introduced and dynamic interaction between planet's magnetic field and solar wind is taken into account.

1.4 Kinetic Theory

This section describes basics of kinetic theory with emphasis on linear theory. Kinetic theory was used successfully for description of plasma instabilities. By instability we refer to normal modes of system that grow in space and time. The term dispersion relation refers to the relationship between wave vector and $\mathbf{k}$ and frequency ω such that $\omega = \omega(\mathbf{k})$ where $\mathbf{k}$ is real and $\omega = \omega_r + i\omega_i$ is imaginary variable. It is common in literature and throughout this text to denote imaginary part of frequency ω_i as γ.

To understand plasma instabilities we use the linear Vlasov equation. To interpret results correctly, we must understand its limitations first. Linear theory will predict properly what modes (i.e. what wave numbers) will grow at what rate but it cannot provide us with information about amplitude, saturation or time evolution after the saturation. To study such phenomena one must use non-linear theory or employ self-consistent numerical modelling. In this text we will distinguish between micro and macro instabilities as follows: if a_i is gyro-radius of thermal population then macro-instability have maximum growth rate at $ka_i \ll 1$, while micro-instability have maximum growth rate at $ka_i \gtrapprox 1$. Distinction between micro and macro instability is somehow blurred by the fact that region of maximum growth rate changes together with plasma parameters. The distinction is useful as to what numerical model should be applied to a studied plasma phenomena. For micro-instability, kinetic theory is necessary while macro-instabilities are, in many cases, well described by fluid equations coupled together with Maxwell's equations.

Kinetic theory describes the time evolution of the distribution function $f_j(\mathbf{x}, \mathbf{v}, t)$ of particle population of the species j in phase space. By including information about particle distribution in velocity space we enable our model to properly treat wave-particle interactions. Such interactions are possible when Doppler shifted wave phase velocity is close to particle's velocity and particle distribution departs from equilibrium of Maxwellian distribution.

Kinetic equation for non-relativistic plasma is given by

$$\frac{\partial f_j}{\partial t} + \mathbf{v} \cdot \frac{\partial f_j}{\partial \mathbf{x}} + \frac{q_j}{m_j}(\mathbf{E} + \mathbf{v} \times \mathbf{B}) \cdot \frac{\partial f_j}{\partial \mathbf{v}} = \left(\frac{\partial f_j}{\partial t} \right)_{\text{collisions}}, \tag{1.13}$$

where q_j is the charge and m_j is the mass of the species j, which is usually either e for electron or p for proton. Right hand side of Equation 1.13 represents change of the function f due to the collisions. Function f can be interpreted as a density of probability that particle with velocity $\mathbf{v}$ is located at the position $\mathbf{x}$. We scale the function f in such a way that integral over the velocity space will give us number density

$$n_j = \int \mathrm{d}^3 v \; f_j. \tag{1.14}$$

This expression is called zeroth velocity moment of distribution function. General form of kth moment is given by

$$g_k = \int \mathrm{d}^3 v \; \mathbf{v}^k f_j. \tag{1.15}$$

First velocity moment, the particle flux density of the jth species is

$$\mathbf{\Gamma}_j = \int \mathrm{d}^3 v \; \mathbf{v} f_j. \tag{1.16}$$

From flux density we can calculate drift velocity $\mathbf{u}_j = \mathbf{\Gamma}_j / n_j$ which is also called bulk velocity. Second velocity moment defines the kinetic energy density tensor

$$\mathbf{W}_j = \frac{m_j}{2} \int \mathrm{d}^3 v \; \mathbf{v}\mathbf{v} f_j, \tag{1.17}$$

but more importantly, it provide us with perpendicular and parallel temperatures with respect to the background magnetic field given by expressions

$$T_{\parallel j} = \frac{m_j}{n_j} \int \mathrm{d}^3 v \; (v_\parallel - u_\parallel)^2 f_j \tag{1.18}$$

$$T_{\perp j} = \frac{m_j}{2 n_j} \int \mathrm{d}^3 v \; (v_\perp - u_\perp)^2 f_j. \tag{1.19}$$

Finally, the third velocity moment gives us heat flux density:

$$\mathbf{q}_j = \frac{m_j}{2}\int \mathrm{d}^3v\, \mathbf{v}v^2 f_j. \tag{1.20}$$

In this thesis, we will work under the assumption that plasma is collisionless which is true except of the atmosphere and low altitude ionosphere. In this case, the right hand side of Equation 1.13 can be neglected and we arrive at Vlasov equation given by

$$\frac{\partial f_j}{\partial t} + \mathbf{v}\cdot\frac{\partial f_j}{\partial \mathbf{x}} + \frac{q_j}{m_j}(\mathbf{E}+\mathbf{v}\times\mathbf{B})\cdot\frac{\partial f_j}{\partial \mathbf{v}} = 0. \tag{1.21}$$

Linear Kinetic Theory

The linear kinetic theory assumes that all physical variables oscillate with a small amplitude around a constant value. Under this assumption, we may expand distribution function, electric and magnetic fields using following approximations

$$\begin{aligned} f_j(\mathbf{x},\mathbf{v},t) &\approx f_j^{(0)}(\mathbf{x},\mathbf{v},t) + f_j^{(1)}(\mathbf{x},\mathbf{v},t), \\ \mathbf{E}(\mathbf{x},t) &\approx \mathbf{E}_0(\mathbf{x},t) + \mathbf{E}^{(1)}(\mathbf{x},t), \\ \mathbf{B}(\mathbf{x},t) &\approx \mathbf{B}_0(\mathbf{x},t) + \mathbf{B}^{(1)}(\mathbf{x},t). \end{aligned} \tag{1.22}$$

A procedure for developing linear theory can be summarized in two steps: (1) linear Vlasov equation is transformed using Fourier analysis into frequency domain which will result in expression for density oscillations; (2) this expression is inserted into Maxwell's equations to give us dispersion relation $\omega = \omega(\mathbf{k})$ solved as initial value problem assuming that $\mathbf{k}$ is real.

1.5 Kelvin-Helmholtz Waves

In magnetized plasma a shear of flows may be unstable to Kelvin Helmholtz Instability (KHI). A typical region where such conditions occur is magnetopause where magnetospheric plasma of low density and high temperature interacts with fast flowing and high density plasma of magnetosheath. Kelvin-Helmholtz waves are considered as a macroscopic phenomenon which can be described using magnetohydrodynamic theory because the typical wavelength is much longer than gyroradius.

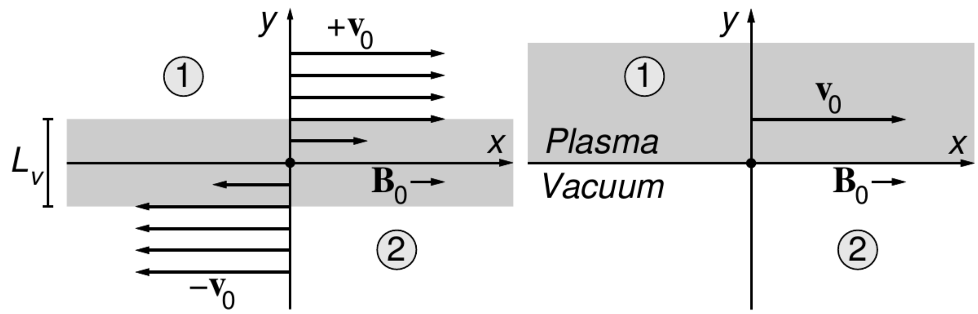

Figure 1.3: Cartoon of a typical set up of Kelvin-Helmholtz instability adopted from *Treumann* [1997].

Figure 1.3 shows a typical set up of Kelvin-Helmholtz instability problem in 2D. Numbers 1 and 2 refer to two media with the different plasma parameters of density, magnetic field and flow speed. Transition region of thickness L_v is a source of velocity shear. Although left and right panels seems to represent two different scenarios, we may think of right set up to be the same as the one in the left panel only shifted in the frame reference of the second media.

Assuming that all variables are only small amplitude oscillations around a constant value, we may approximate variables by:

$$\begin{aligned} \mathbf{B} &= \mathbf{B}_0 + \mathbf{B}^{(1)}, \\ \mathbf{x} &= \mathbf{x}_0 + \mathbf{x}^{(1)}, \\ n &= n_0 + n^{(1)}, \\ p &= p_0 + p^{(1)}. \end{aligned} \tag{1.23}$$

To solve for dispersion relation of KHI, we substitute above variables into the induction and momentum equations,

$$\begin{aligned} \frac{\partial \mathbf{B}}{\partial t} &= -\nabla \times \mathbf{E} \\ \rho \frac{\mathrm{d}}{\mathrm{dt}} \mathbf{v} &= \mathbf{J} \times \mathbf{B} - \nabla p. \end{aligned} \tag{1.24}$$

If electric field have a simple form $\mathbf{E} = -\mathbf{v} \times \mathbf{B}$ derived from one fluid approxi-

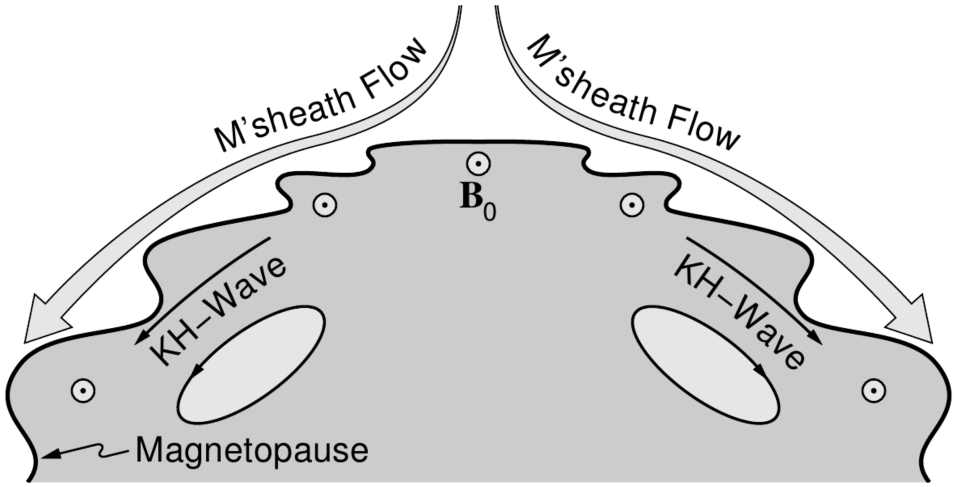

Figure 1.4: Schematic representation of Kelvin-Helmholtz instability in equatorial plane as seen from above north pole. Courtesy *Treumann* [1997].

mation then electric current is $\mathbf{J} = \nabla \times \mathbf{B}$ and total pressure is given by

$$\mu_0 p_{\mathrm{tot}}^{(1)} = \mu_0 p^{(1)} + \mathbf{B}_0 \cdot \mathbf{B}^{(1)}. \tag{1.25}$$

Combining Equations 1.23 and 1.25 with Eq. 1.24 we arrive at the expression for position $\mathbf{x}^{(1)}$:

$$m_i n_0 \left[(\mathbf{v}_A \cdot \nabla)^2 - \frac{\partial^2}{\partial t^2} \right] \mathbf{x}^{(1)} = \nabla p_{tot}^{(1)} + \mathbf{a}. \tag{1.26}$$

Here $\mathbf{v}_A = \mathbf{B}_0 / \sqrt{\mu_0 m_i n_0}$ is Alfvén velocity and vector $\mathbf{a}$ is defined as

$$\mathbf{a} = -\mathbf{B}^{(1)} \cdot \nabla \mathbf{B}_0 + \mathbf{B}_0 \cdot \nabla (\mathbf{B}_0 \nabla \cdot \mathbf{x}^{(1)} + \mathbf{x}^{(1)} \cdot \nabla \mathbf{B}_0). \tag{1.27}$$

For incompressible plasma and homogeneous flows on both sides of transition region, we can simplify the expression by setting $\nabla \cdot \mathbf{x}^{(1)} = 0$. The resulting expression is a surface wave representing ripples of the infinitesimally thin transition region:

$$\mathbf{x}^{(1)} = \frac{\nabla p_{tot}^{(1)}}{m_i n_0 [\omega^2 - (\mathbf{k} \cdot \mathbf{v}_A)^2]}. \tag{1.28}$$

Two variables $\mathbf{x}^{(1)}$ and $p_{tot}^{(1)}$ are plane waves with wavenumber $\mathbf{k} = k_x \hat{\mathbf{e}}_x + k_z \hat{\mathbf{e}}_z$ and frequency ω. Displacement across the boundary is continuous as well as total pressure. Using above property and the fact that frequency in region 1 is observed from region 2 Doppler-shifted to $\omega_1 = \omega - \mathbf{k} \cdot \mathbf{v}_0$, we can manipulate the expression into

$$\frac{1}{n_2[\omega^2 - (\mathbf{k} \cdot \mathbf{v}_{A2})^2]} + \frac{1}{n_1[(\omega - \mathbf{k} \cdot \mathbf{v}_0)^2 - (\mathbf{k} \cdot \mathbf{v}_{A1})^2]} = 0. \tag{1.29}$$

Equation 1.29 is a dispersion relation of the Kelvin-Helmholtz wave in incompressible plasma where $\mathbf{v}_{A1,2}$ is Alfvén velocity in the region 1 and 2. Interestingly, the expression describes two Alfvén waves as seen from the second media (non-streaming). KH instability is a source of Alfvén waves which is of importance to geophysical studies. Equation 1.29 yields the unstable solution

$$\omega_{KH} = \frac{n_1 \mathbf{k} \cdot \mathbf{v}_0}{n_1 + n_2}, \tag{1.30}$$

the instability criteria is satisfied when imaginary part of complex root becomes positive

$$(\mathbf{k} \cdot \mathbf{v}_0)^2 > \frac{n_1 + n_2}{n_1 n_2}[n_1(\mathbf{k} \cdot \mathbf{v}_{A1})^2 + n_2(\mathbf{k} \cdot \mathbf{v}_{A2})^2]. \tag{1.31}$$

Equation 1.31 is the condition for instability. As expected, streaming velocity $\mathbf{v}_0$ which acts as a source of free energy, is the important factor in driving the boundary unstable.

In this section we gave the overview of Kelvin-Helmholtz instability using ideal MHD treatment and stated that a typical location of KH unstable region is magnetopause boundary. Figure 1.4 is a schematic representation of equatorial plane observed from the north pole. Fast flows of plasma in magnetosheath generates ripples at the boundary and they travel tailward together with the bulk flows. As the KH wave convects along the flank, its amplitude grows because the instability conditions are still satisfied. Ultimately, the wave growth becomes nonlinear and the treatment we carried out here is not valid anymore. During the convection, KHI generates Alfvén waves propagating along the geomagnetic field lines. Alfvén waves of certain frequencies may trigger resonances in the magnetosphere which appear as pulsations.

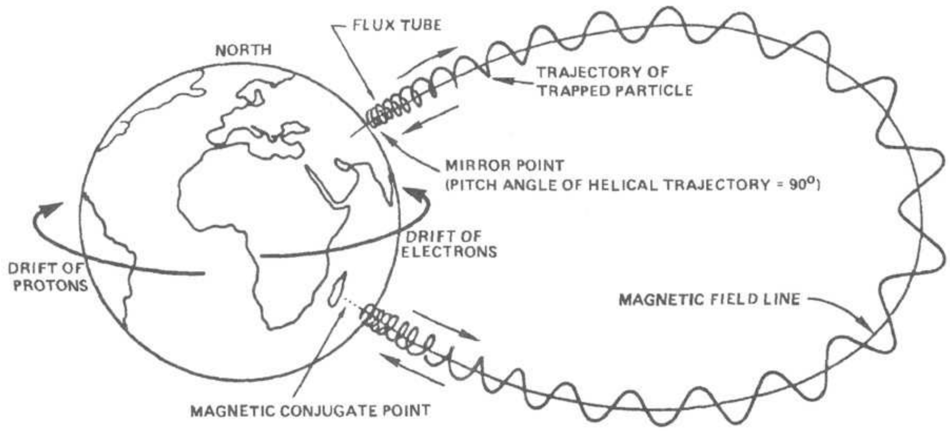

Figure 1.5: Cartoon of drift-bounce motion in the intrinsic magnetic field of Earth. Charged particles are bouncing between two conjugate mirror points while at the same time they undergo drifting motion around the planet. The direction of the drift is given by a charge of the particle.

1.6 EMIC Waves

1.6.1 Basic Parameters

Electromagnetic ion cyclotron (EMIC) waves are left-hand-polarized in the sense of wave propagation along the magnetic field. EMIC waves have a transverse fluctuation of magnetic field and plasma velocity, and they are driven unstable by temperature anisotropy through the ion-cyclotron instability.

Generation Region	L=2-7 $\lvert\mathrm{MLat}\rvert < 20$
Frequency	Pc1 - Pc2 $\sim \Omega_{O+} - \Omega_{H+}$
Pointing Flux	$0.1 - 25\mu$W/m^2
Amplitude	~ 1 nT

EMIC waves are continuous geomagnetic pulsations with frequencies below the proton gyrofrequency Ω_p. They are responsible for heating of MeV energetic electrons by Landau damping. This heating causes an increase in the electron flux into the ionosphere, which can be observed as stable red auroral arcs [*Thorne and Horne*, 1992]. Most importantly, it is believed that EMIC waves are an important loss mechanism of ring current protons. EMIC waves are observed in the range of Pc1 (0.2 -

5 Hz) pulsations. Typical parameters of EMIC waves are summarized in Table 1.6.1. Using satellite observations, ***Anderson et al.*** [1992a] identified that EMIC waves are present at specific regions in the magnetosphere, with the most typical location being L>7, although they also occur at L=2-7. The typical latitude range is $|\text{MLat}| < 20°$. The properties of EMIC waves are described in the paper by ***Anderson et al.*** [1992b]. EMIC waves can be observed on the ground as well as in the space. It is found that these waves have peak-to-peak amplitude of ~ 1 nT.

1.6.2 Dispersion Relation

The linear dispersion relation for plasma describes frequency as a function of wave vector k for various types of plasma collective modes. Using linear kinetic theory it is possible to study the dispersion relation as a function of plasma parameters like magnetic field strength, particle temperature, etc. The solution of Eq. 3.33 for different anisotropy parameters is illustrated in Fig. 1.6. Blue lines represent the real part of frequency ω_r scaled to the proton gyrofrequency $|\Omega_P|$. Green line represents imaginary part of the frequency γ. In Fig. 1.6 all plasma parameters are kept the same except for the temperature anisotropy. We can see that as the anisotropy ($T_\perp/T_\parallel$) increases from 1 to 3, the peak of the imaginary frequency γ increases. Positive frequency γ can be interpreted as wave growth in time due to the unstable plasma conditions.

More complex conditions which are closer to the magnetospheric parameters are considered by ***Horne and Thorne*** [1993]. They consider the plasma dispersion relation for a mixture of H^+, He^+ and O^+ in the ratio of 79/20/1% propagating in parallel as well as perpendicular direction. Fig. 1.7 summarizes EMIC wave propagation in the parallel direction. By identifying the cut-off and resonance/bi-ion frequencies we can provide an explanation of the polarization change that occurs during wave propagation at the cross-over frequencies. Note that bi-ion frequencies are resonances (i.e. $N = kc/\omega_p =$ infinity) occurring in multi-species plasmas. Adding more species and solving the dispersion relation adds even more complexity through the appearance of stop bands and cut offs. ***Thorne and Horne*** [1993] studied the interaction of EMIC waves with a small concentration of O^+ ions. They found that waves propagating oblique to the geomagnetic field are absorbed at the bi-ion frequency when oxygen ions are relatively hot ($T > 1$ keV). This may lead to heating of oxygen in the outer radiation belt. Also, the gradient of magnetic field and density, for waves travelling poleward, causes a rapid change of the propagation angle. This large propagation

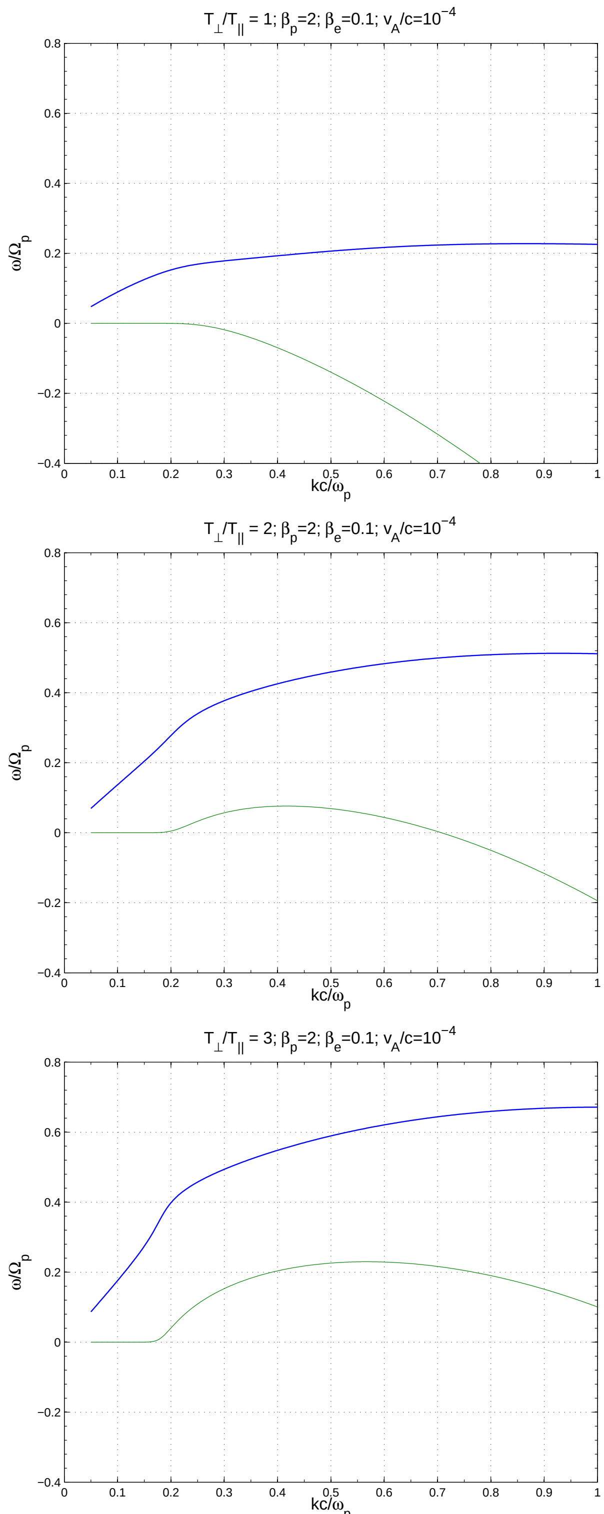

Figure 1.6: Ion-cyclotron instability dispersion relation and growth rates for various anisotropy ratios. The blue and green curves represent real part and imaginary part of frequency, respectively.

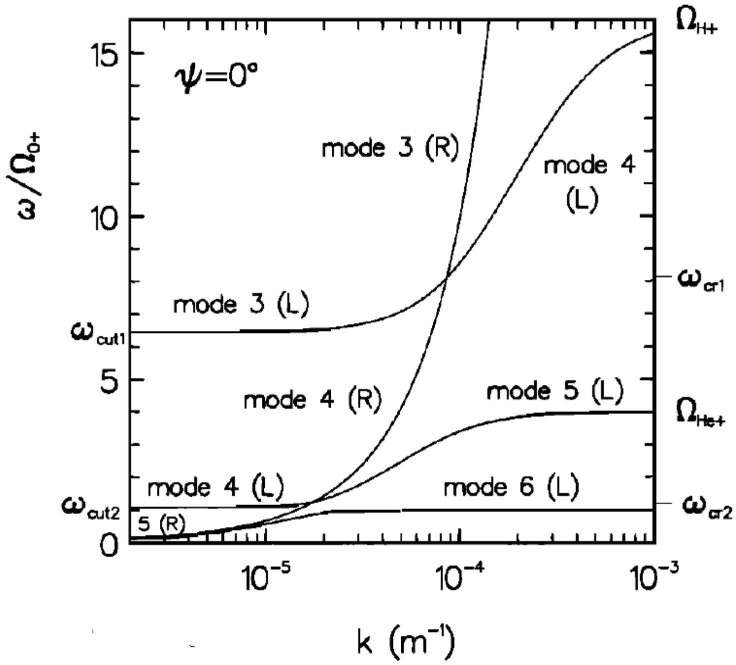

Figure 1.7: Dispersion relation of ions cyclotron waves in multispecies plasma in magnetosphere. Credit: *Horne and Thorne* [1993].

angle causes waves to be damped by electron Landau damping.

1.6.3 Numerical Modelling and Observations

Horne and Thorne [1994] studied EMIC wave propagation in the magnetosphere using wave tracing techniques to find the most common location of waves. They studied a convective instability (i.e. $k_i = -\gamma/|v_g|$) at the location of $|\text{MLat}| < 5°$ and L~ 7 and concluded that several regions are preferential for growth. The typical location of EMIC wave growth is found to be in the region of $L > 7$, which is in agreement with observations *Anderson et al.* [1992a, b]. Also, they found that the plasmapause can act as waveguide, allowing EMIC waves to bounce between bi-ion surfaces and pass through the instability region several times before being lost. Other regions are not favourable for growth due to the low plasma beta or high magnetic field. Although, their results partially agree with the observations, the model omits important aspects of physics, for example nonlinear effects when amplitude of the wave breaks the linear theory assumption of small perturbation.

Another driver of EMIC waves can be solar wind dynamic pressure pulses as studied by *Usanova et al.* [2008], who analyzed the relation between EMIC wave generation and magnetospheric compression due to solar wind pressure. Using both THEMIS satellite data and CARISMA ground-based observations they localized the EMIC wave source region to be spatially confined inside of the plasmasphere but very close to the plasmapause. The amplitude of the waves reach ~ 0.3 nT on the ground and $\sim 3-7$ nT in THEMIS observations.

1.6.4 Bouncing Wave Packet Theory

Many recent publications explain long-lived EMIC waves using the notion of a bouncing wave packet (BWP) [*Khazanov et al.*, 2002, 2006]. In this interpretation, a wave originating from the unstable region travels along the field line and is reflected on bi-ion resonant surfaces that are present in the multi-ion species plasmas. The loss of energy that occurs through this non-perfect reflection is then compensated by another passing through the unstable region. This theory is not fully supported by observations. For example, *Loto'aniu et al.* [2005] analyzed EMIC wave pointing flux using CRRES data that covered the range $L = 3.5-8$, |MLat$< 30°$, and MLT 1400 - 0800. They found an energy average of 1.3 μW/m^2 with a peak at 25 μW/m^2, and concluded that the Poynting vector was bidirectional for $|\text{MLat}| < 11°$ but unidirectional for

$|\mathrm{MLat}| > 11°$. On the other hand, the theory of BWP is supported by simulation efforts in the past *Khazanov et al.* [2002, 2006] as well as observations *Anderson et al.* [1992a, b].

The above mentioned numerical models are based on ray-tracing in a prescribed spatial distribution of magnetic field, density, and temperature. Wave growth and damping is computed using the linear kinetic dispersion relation and the waves are propagated using the local wave group velocity. The ray-tracing techniques raise several questions (i.e. *Thorne and Horne* [2007]; *Khazanov et al.* [2007]) as to whether it is sufficient to describe EMIC waves spatial distribution. Some of the questions ray-tracing models cannot answer are summarized as follows:

- The role of non-Maxwellian distribution functions on the interaction of EMIC waves with the ion cyclotron instability. Decomposition of particle distribution function into several bi-Maxwellian functions is necessary but it could fail in the case of non-Maxwellian distributions. Hybrid-kinetic ion codes can work with arbitrary distribution functions, which allows us to study complex plasma conditions.

- Ray-tracing models are unable to model the non-linear effects of wave growth. Also, such models do not contain feedback of the wave on the particle population. By omitting this feedback plasma cannot relax into an equilibrium state.

- Due to the neglect of self-consistent wave-particle interaction, solution of wave reflection at bi-ion surfaces may lead to errors in the results from ray-tracing model.

Bibliography

Anderson, B. J., R. E. Erlandson, and L. J. Zanetti, A Statistical Study of Pc 1-2 Magnetic Pulsations in the Equatorial Magnetosphere, 1. Equatorial Occurrence Distributions, *J. Geophys. Res.*, *97*, 3075–3088, 1992a.

Anderson, B. J., R. E. Erlandson, and L. J. Zanetti, A Statistical Study of Pc 1-2 Magnetic Pulsations in the Equatorial Magnetosphere, 2. Wave Properties, *J. Geophys. Res.*, *97*, 3089–3101, 1992b.

Baumjohann, W., and R. A. Treumann, *Basic Space Plasma Physics*, Imperial College Press, London, 1996.

Hellinger, P., P. M. Trávníček, J. C. Kasper, and A. J. Lazarus, Solar wind proton temperature anisotropy: Linear theory and WIND/SWE observations, *Geophys. Res. Lett.*, *33*, L09,101, 2006.

Horne, R. B., and R. M. Thorne, On the Preferred Source Location for the Convective Amplification of Ion Cyclotron Waves, *J. Geophys. Res.*, *98*, 9233–9247, 1993.

Horne, R. B., and R. M. Thorne, Convective Instabilities of Electromagnetic Ion Cyclotron Waves in the Outer Magnetosphere, *J. Geophys. Res.*, *99*, 17,259–17,273, 1994.

Khazanov, G. V., K. V. Gamayunov, V. K. Jordanova, and E. N. Krivorutsky, A self-consistent model of the interacting ring current ions and electromagnetic ion cyclotron waves, initial results: Waves and precipitating fluxes, *J. Geophys. Res.*, *107*, 2002.

Khazanov, G. V., K. V. Gamayunov, D. L. Gallagher, and J. U. Kozyra, Self-consistent model of magnetospheric ring current and propagating electromagnetic ion cyclotron waves: Waves in multi-ion magnetosphere, *J. Geophys. Res.*, *111*, A10,202, 2006.

Khazanov, G. V., K. V. Gamayunov, D. L. Gallagher, and J. U. Kozyra, Reply to comment by R. M. Thorne and R. B. Horne on Khazanov et al. [2002] and Khazanov et al. [2006], *J. Geophys. Res.*, *112*, A12,215, 2007.

Loto'aniu, T. M., B. J. Fraser, and C. L. Waters, Propagation of electromagnetic ion cyclotron wave energy in the magnetosphere, *J. Geophys. Res.*, *110*, A07,214, 2005.

Thorne, R. M., and R. B. Horne, The contribution of ioncyclotron waves to electron heating and SARarc excitation near the stormtime plasmapause, *Geophys. Res. Lett.*, *19*, 417, 1992.

Thorne, R. M., and R. B. Horne, Cyclotron absorption of ioncyclotron waves at the biion frequency, *Geophys. Res. Lett.*, *20*, 317, 1993.

Thorne, R. M., and R. B. Horne, Comment on Khazanov et al. [2002] and Khazanov et al. [2006], *J. Geophys. Res.*, *112*, A12,214, 2007.

Treumann, R. A., *Advanced space plasma physics*, Icp, 1997.

Usanova, M. E., I. R. Mann, I. J. Rae, Z. C. Kale, V. Angelopoulos, J. W. Bonnell, K.-H. Glassmeier, H. U. Auster, and H. J. Singer, Multipoint observations of magnetospheric compression-related EMIC Pc1 waves by THEMIS and CARISMA, *Geophys. Res. Lett.*, *35*, L17S25, 2008.

Chapter 2

Spacecraft Missions to Mercury

Because of its proximity to the Sun, the planet Mercury is difficult to observe in the optical frequency range as well as it is technically challenging to design a space probe able to withstand the heat and the radiation at the orbital distance of 0.39 AU. Until recently, the only "in situ" available data were from the three flybys of Mariner 10 which visited Mercury in 1974-75 and gave us a first glimpse into the intrinsic magnetic field. It took another 35 year to revisit the planet using the NASA's MESSENGER spacecraft. Currently, European Space Agency (ESA) is preparing the third mission called BepiColombo named after the Italian engineer who designed the orbit of Mariner 10 and it is scheduled to arrive at Mercury in 2022 after the expected launch in 2015. In the following sections we will describe the all three missions chronologically but we will concentrate in a full detail only on MESSENGER mission as it is the most relevant to our work.

2.1 Mariner 10

Mariner 10 was launched by NASA on November 1, 1973 with the objectives to survey planets Venus and Mercury by performing several close flybys. The two out of three Mercury's flybys encountered the intrinsic magnetic field (for example *Ness et al.* [1975]) of the planet and sparked an increased scientific interest in Mercury. The data from Mariner 10 revealed Earth-like topology of the magnetic field including the same orientation of the magnetic dipole moment. The three flybys of Mariner 10 are summarized in the following table:

- **1st Flyby:** On March 29, 1974 (20:47 UT) passed the planet on the shadow side

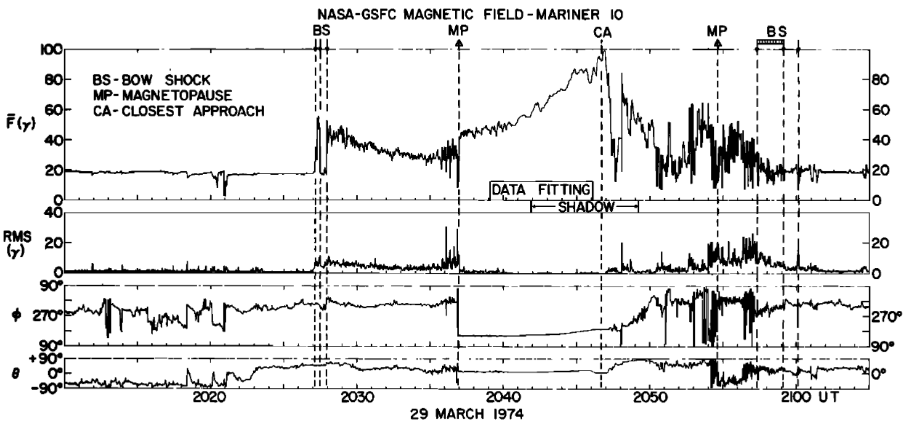

Figure 2.1: First flyby of Mariner 10 spacecraft revealed intrinsic magnetic field of planet Mercury. From *Ness et al.* [1975].

at a range of 703 kilometers (437 mi).

- **2nd Flyby:** On September 21, 1974 passed the planet at the dayside below the southern hemisphere at a more distant range of 48,069 km (29,869 mi). This flyby did not encounter the planet's own magnetic field.

- **3rd Flyby:** On March 16, 1975 passed the planet almost over the north pole at a range of 327 km (203 mi).

2.2 MESSENGER

In July 1999, NASA selected MESSENGER as the seventh Discovery Program mission. The MErcury Surface, Space ENvironment, GEochemistry, and Ranging (MESSENGER) space probe is a low cost mission to orbit Mercury with the orbital phase to last for two years (the mission was extended by one more year on November 2011) and possible extension by one more year. The 485 kg spacecraft was designed to survey the most inner planet of our solar system and to study a chemical composition, the magnetic field and a geological history of the planet. MESSENGER is the second mission after Mariner 10 to visit Mercury and to improve the previous estimates of the magnetic dipole strength to be 195 ± 10 nT R_M^3 by *Anderson et al.* [2011] where $R_M = 2440$km. They concluded that the magnetosphere is smaller than that of Earth by a factor of 8 but very similar in the terms of the overall structure.

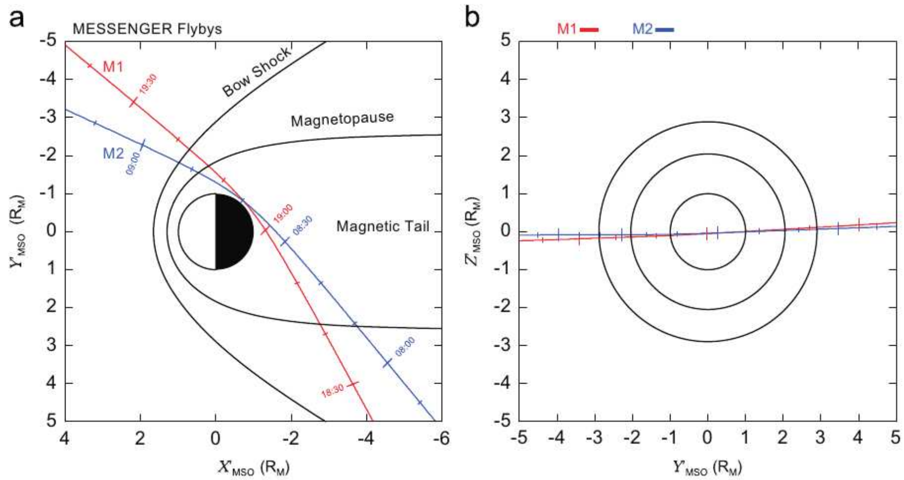

Figure 2.2: The first and the second flybys of MESSENGER through the magnetosphere of Mercury. Credit: *Raines et al.* [2011].

2.2.1 Trajectory

MESSENGER performed the three flybys in the near equatorial plane prior to the orbit insertion on March, 18 2011. The all flybys (see Figure 2.2) entered Mercury environment in the dusk flank and left in the morning sector. The flybys were designed to slow down the spacecraft and to prepare it for the orbital phase of the mission. The flybys provide us with wealth of data including the magnetic field; the exosphere measurements and the spectrometer data. Table 2.2.1 presents a summary of the three flybys.

Flyby	Date	Closest approach [km]
1st	14 January 2008	201
2nd	6 October 2008	199
3rd	29 September 2009	228

Table 2.1: A summary of the MESSENGER's flybys.

An orbit was chosen as a compromise between observational opportunities and design constrains of temperature, power, downlink bandwidth, etc. The 12 hours orbit and altitude ranking between 200 and 15193 km is sufficient to produce high quality of a data coverage from the inner magnetosphere up to the bowshock crossings in the far tail regions. Eccentricity of the orbit is 0.7396 with inclination 80° from the equator. The schematic of the orbit is in Figure 2.3 and to maintain its parameters every 88 days

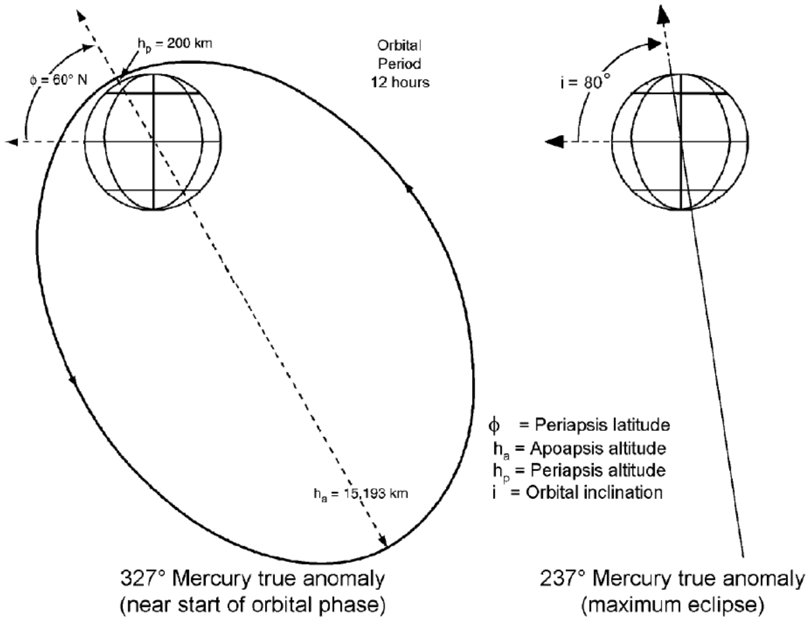

Figure 2.3: An orbit of MESSENGER mission around the planet Mercury. Credit: *Santo* [2001].

(one Mercury year) a sequence of two burns is executed. The planet does not obstruct the Earth-MESSENGER line of sight so that the time for data transfer is maximized.

2.2.2 Instruments

Figure 2.4 depicts schematics of MESSENGER spacecraft with annotated locations of the instruments. Because of a planet's proximity to the surface of the Sun, temperatures can reach up to 450 degrees Celsius. To protect the spacecraft from direct exposure to the Sun, the body and the instruments are hidden behind a sunshade made of a heat-resistant ceramic cloth. The following instruments were chosen to study the mission objectives (Note the text was adopted from website of the MESSENGER mission):

- **Mercury Dual Imaging System (MDIS):** This instrument consists of wide-angle and narrow-angle imagers that will map landforms, track variations in surface spectra and gather topographic information. A pivot platform will help point it in whatever direction the scientists choose. The two instruments will enable MESSENGER to ”see” much like our two eyes do.

- **Gamma-Ray and Neutron Spectrometer (GRNS):** This instrument will detect

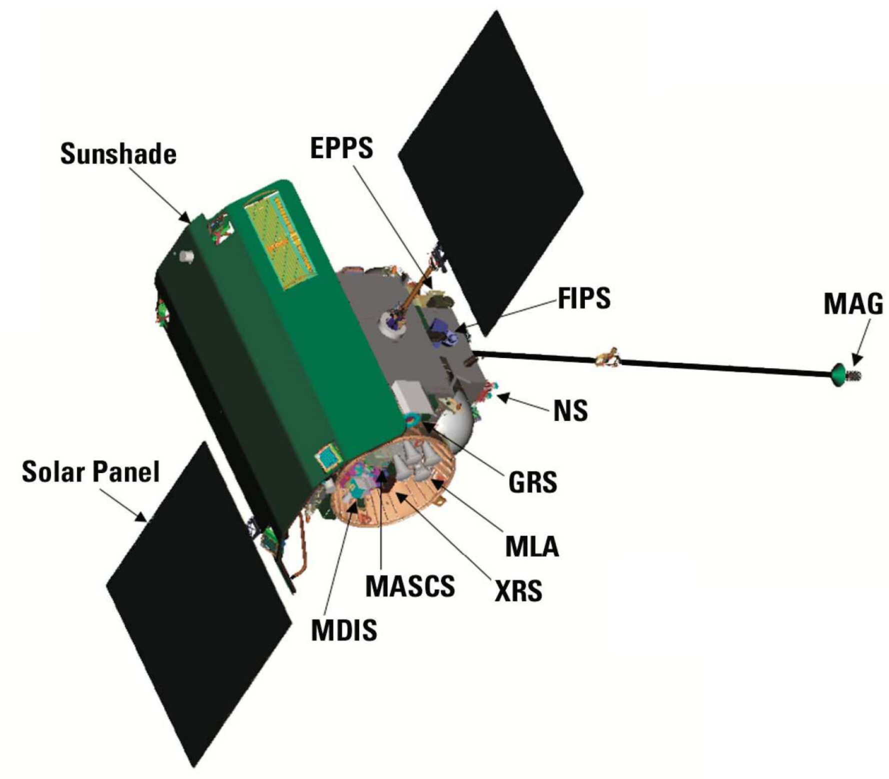

Figure 2.4: Computer rendered MESSENGER spacecraft with location of important instruments.

gamma rays and neutrons that are emitted by radioactive elements on Mercury's surface or by surface elements that have been stimulated by cosmic rays. It will be used to map the relative abundances of different elements and will help to determine if there is ice at Mercury's poles, which are never exposed to direct sunlight.

Gamma rays and high-energy X-rays from the Sun, striking Mercury's surface, can cause the surface elements to emit low-energy X-rays. XRS will detect these emitted X-rays to measure the abundances of various elements in the materials of Mercury's crust.

- **Magnetometer (MAG):** This instrument is at the end of a 3.6 meter (nearly 12-foot) boom, and will map Mercury's magnetic field and will search for regions of magnetized rocks in the crust.

- **Mercury Laser Altimeter (MLA):** This instrument contains a laser that will send light to the planet's surface and a sensor that will gather the light after it has been reflected from the surface. Together they will measure the amount of time for light to make a round-trip to the surface and back. Recording variations in this distance will produce highly accurate descriptions of Mercury's topography.

- **Mercury Atmospheric and Surface Composition Spectrometer (MASCS):** This spectrometer is sensitive to light from the infrared to the ultraviolet and will measure the abundances of atmospheric gases, as well as detect minerals on the surface.

- **Energetic Particle and Plasma Spectrometer (EPPS):** EPPS measures the composition, distribution, and energy of charged particles (electrons and various ions) in Mercury's magnetosphere.

- **Radio Science (RS):** RS will use the Doppler effect to measure very slight changes in the spacecraft's velocity as it orbits Mercury. This will allow scientists to study Mercury's mass distribution, including variations in the thickness of its crust.

Only two instruments are directly relevant to the topic of this thesis. The details of Magnetometer (MAG) and Energetic Particle and Plasma Spectrometer (EPPS) are provided in *Gold et al.* [2001].

Instrument	Mass [kg]	Power [W]	Data rate
MAG		2.0	
Fluxgate magnetometer	1.5		14.2 b/s
3.6-m boom	2.0		1.2 Mb/d
EPPS		2.0	
Energetic particle spectrometer			140 b/s
Fast imaging plasma spectrometer	2.25		12.1 Mb/d

Table 2.2: Magnetic field and particles instruments on board of MESSENGER mission. Note that data rates are mission averages during the orbital phase.

MAG Instrument

MAG characteristics	
Detector	3-axis, ring-core fluxgate
Mounting	3.6-m boom
Ranges	± 1024 nT, $\pm 65,536$ nT
Quantization	16 bits
Internal sample rate	40 Hz
Averaging intervals	0.025-1 s
Readout rates	0.01; 0.1; 1; 10; 20; 40 Hz
AC channel	1-10 Hz

Table 2.3: Characteristics of magnetometer instrument on board of MESSENGER.

The new data from the MAG instrument on MESSENGER provides time series of magnetic fluctuations that will be investigated using the models presented later in the thesis. For example, sawtooth oscillations in the magnetic field have been interpreted observationally as signatures of the KH instability along the dusk flank of the magnetosphere. In chapter 5 we will show comparisons between MESSENGER observations and predictions of the model, and provide a detailed explanation of the physical processes that excite KH instabilities in the Mercury's magnetosphere.

The MAG instrument is mounted on the 3.6 m long boom which is in the anti-sunward direction. Although MAG can measure in the two ranges of ± 1024 and $\pm 65,536$ nT, only the smaller range is used during the orbital phase of the mission. Digital signal processing unit uses 16 bit resolution which provides quantization approximately 0.03 nT. Nominal sampling of 0.1 Hz changes during the orbit. Sampling is increased to 10 Hz near the perigee and samples of 40 Hz are taken at crossings of magnetospheric boundary which is predicted by an empirical model. The changes of

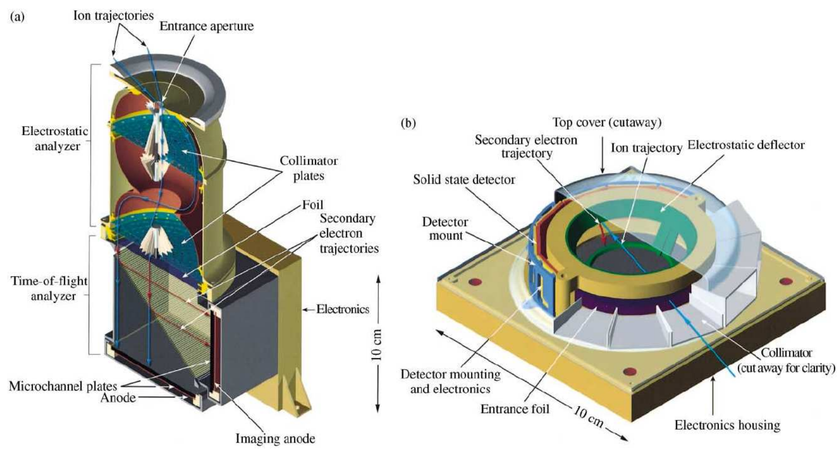

Figure 2.5: Energetic Particle and Plasma Spectrometer (EPPS) combine Energetic Particle Spectrometer (EPS) and a Fast Imaging Plasma Spectrometer (FIPS) sensors. Adopted from *Gold et al.* [2001].

sampling frequency guarantee the optimal usage of available data link.

EPPS Instrument

The data from the EPPS instrument will be used to estimate the plasma parameters which are necessary to initialize the global numerical model in Chapter 5. More importantly, we will compare direct observation of the FIPS instrument with the particle tracing simulations of the Mercury's exosphere in Chapter 7 to study the source and the sink processes of heavy ions.

Energetic Particle and Plasma Spectrometer (EPPS) (Figure 2.5) combine Energetic Particle Spectrometer (EPS) and a Fast Imaging Plasma Spectrometer (FIPS) sensors. The instrument package is designed to capture the low-energy ions from the surface, pickup ions, particles accelerated in the magnetosphere and partially even the solar wind particles when the spacecraft leaves the environment of Mercury. Both instruments use the time-of-flight technique to measure the charge/mass ratio of incoming particles. The EPPS electronics processes the time-of-flight data to provide $\pm$50 ps timing resolution for only 50 mW of power.

The EPS spectrometer measures the energy spectra, atomic composition and pitch angle distributions of energetic ions in the range 10 keV/nuc to $\approx$ 5 MeV and electrons from 20 to 700 keV. Ion energy is measured by time-of-flight technique of secondary electrons produced by ions passing through the entrance and exit foils. Energy range

EPPS characteristics	
FIPS	
Measured species	H, ^{3}He, ^{4}He, O, Ne, Na, K, S, Ar, Fe
Field-of-view	360° azimuth × 70° elevation
Geometrical factor	$\approx$ 0.05 cm^{2}sr
Entrance foil	$\approx$ 1.0 μg/cm^2 carbon
TOF range	50 ns - 500 ns
Defection voltage	0.0 - 8.0 kV
Energy/charge range	0.0 - 10.0 keV/q
Voltage scan period	1 min
EPS	
Measured species	H, He, CNO, Fe, electrons
Field-of-view	160° azimuth × 12° elevation
Geometrical factor	$\approx$ 0.1 cm^{2}sr
Foils	Aluminized polyimide; 9 μg/cm^2
TOF range	0 - 200 ns, $\pm$200 ps (1σ)
Peak input rate	1 MHz
Detectors	6 Si, 500 μm thickness, 2 cm^2 each
Energy range	10 keV/nuc-5 MeV total energy
Integration period	Variable, 36 s average

Table 2.4: Characteristics of magnetometer instrument on board of MESSENGER.

is determined by allowed time range of the instrument. The measurement of the events is recorded, on average, every 36 seconds. Electrons are measured only by two out of six sensor segments.

The FIPS instrument is targeted at low-energy plasma in the range of few eV/q up to $\approx$ 10 keV/q and the data are relevant to the study of the ion exosphere. The FIPS uses an electrostatic analyzer which covers the full hemisphere. By applying the deflection voltage only a narrow range of E/q is allowed to enter the instrument. The deflection voltage is stepped from 0 to 8 kV over 1 minute interval and covers 0 to 10 keV/q energy of particles. From the information of E/q energy and the distance which particles travel, the instrument assemble distribution function of mass/charge species.

2.3 BepiColombo

BepiColombo is a joint mission of the European Space Agency (ESA) and the Japan Aerospace Exploration Agency (JAXA) which will consist of two components designed to study the magnetosphere and the exosphere of Mercury in tandem, complementing each other. The both probes will be carried by Mercury Transfer Module with no scientific payload and during the manoeuvre of the orbit insertion it will separate into Mercury Planetary Orbiter (MPO) and Mercury Magnetospheric Orbiter (MMO). The launch of the mission is scheduled on August 15, 2015 using Ariane 5 launch vehicle. A one year long orbital mission is predicted to start on January, 2022 after gravitational assist from Earth (1x), Venus (2x) and Mercury (4x). The information about the orbit is summarized in Table 2.3.

	MPO	MMO
Orbital Period [h]	2.3	9.2
Apogee [km]	1508	12000
Perigee [km]	400	400

Table 2.5: The basic information of orbit for Mercury Planetary Orbiter (MPO) and Mercury Magnetospheric Orbiter (MMO).

The MPO will contain 11 scientific instruments, including imagers, laser altimeter and X-Ray spectrometer for mapping the surface at different wavelengths to identify presence of water. The possible regions which will be surveyed are polar craters which are in permanent shadow from Sun's radiation. The mission objectives are to study:

- The evolution of planet and consequences of its proximity to the Sun.
- Geology and composition from interior to the surface.
- The exosphere and its role to the global dynamics.
- The origin of Mercury's magnetic field.

Bibliography

Anderson, B. J., C. L. Johnson, H. Korth, M. E. Purucker, R. M. Winslow, J. A. Slavin, S. C. Solomon, R. L. McNutt, J. M. Raines, and T. H. Zurbuchen, The global magnetic field of Mercury from MESSENGER orbital observations., *Science*, *333*, 1859–62, 2011.

Gold, R. E., S. C. Solomon, R. L. McNutt, A. G. Santo, M. H. Acuña, J. B. Abshire, B. J. Anderson, R. S. Afzal, G. B. Andrews, P. D. Bedini, J. C. Cain, A. F. Cheng, L. G. Evans, W. C. Feldman, R. B. Follas, G. Gloeckler, J. O. Goldsten, S. E. Hawkins, N. R. Izenberg, S. E. Jaskulek, E. A. Ketchum, M. R. Lankton, D. A. Lohr, B. H. Mauk, W. E. McClintock, S. L. Murchie, C. E. Schlemm, D. E. Smith, R. D. Starr, and T. H. Zurbuchen, The MESSENGER mission to Mercury: scientific payload, *Plan. Space Sci.*, *49*, 1467–1479, 2001.

Ness, N. F., K. W. Behannon, R. P. Lepping, and Y. C. Whang, Magnetic field of Mercury confirmed, *Nature*, *255*, 204–205, 1975.

Raines, J. M., J. A. Slavin, T. H. Zurbuchen, G. Gloeckler, B. J. Anderson, D. N. Baker, H. Korth, S. M. Krimigis, and R. L. McNutt, MESSENGER observations of the plasma environment near Mercury, *Plan. Space Sci.*, *59*, 2004–2015, 2011.

Santo, A. G., The MESSENGER mission to Mercury: spacecraft and mission design, *Plan. Space Sci.*, *49*, 1481–1500, 2001.

Chapter 3

Numerical models

3.1 A Hybrid-kinetic multi-species model

This section describes the development of a hybrid-kinetic model that forms basis for studies of Electro-Magnetic Ion Cyclotron (EMIC) waves in Earth's magnetosphere and a global model of the planet Mercury. Several different techniques of plasma simulation are available to researchers today. Depending on a physical problem, temporal and spatial scales, we need to select appropriate tool which describes studied phenomenon correctly. The two of the most common techniques are particle-in-cell (PIC) and magnetohydrodynamics (MHD) approach (Fig. 3.1). The former one (PIC) uses a single point in the phase-space which represents a cloud of particles with very similar velocities at a similar location. The PIC approach is used for both ions as well as electrons. Selected numerical model enforce a limit on a range of time steps $\triangle t$ for particle advancing (i.e. $\triangle t \ll \Omega_e^{-1}$) where Ω_e is an electron gyrofrequency. The latter approach (MHD) approximates the plasma by the equation for fluids coupled together with the Maxwell equations through the Lorentz force and thus called magneto-hydrodynamic.

In many cases, ions play a dominant role in the plasma physical processes and in such regime we can neglect the kinetic contribution of electrons. The technique where each species is treated using a different method is called a hybrid model. A common scenario is for ions to be treated using the PIC approach and electrons as a charge neutralizing fluid. This is the approach used in our work. For an overview of other possibilities see the summary of hybrid codes by *Lipatov* [2002].

3.1.1 Introduction

Several different techniques are used to advance the hybrid codes into the next time level (i.e. *Winske* [1985]; *Winske and Omidi* [1993, 1996]). In this work, the Current Advance and Cyclic Leapfrog (CAM-CL) method *Matthews* [1994] is used, which have the advantage of cycling through the particles in a single pass. Another possibility involves pre-pushing of the particles in order to obtain the electric field [*Harned*, 1982]. The various implementations of the hybrid codes leverage different available numerical techniques: *Harned* [1982] uses a predictor-corrector scheme [*Press et al.*, 1992]; *Winske* [1985] uses a moment method and *Horowitz et al.* [1989] uses sub-stepping of the magnetic field. The CAM-CL implementation uses field sub-stepping to increase the temporal resolution of electromagnetic fields. CAM-CL approach was used in 3D by *Trávníček et al.* [2007] to explore the magnetosphere of Mercury.

CAM-CL hybrid code has several unique features compared to other hybrid code implementations:

- Multiple ion species are treated in a single computational pass through data arrays.
- CAM advances ionic current density instead of fluid velocity.
- Velocity is collected a half time step ahead, before equation of motion is applied.

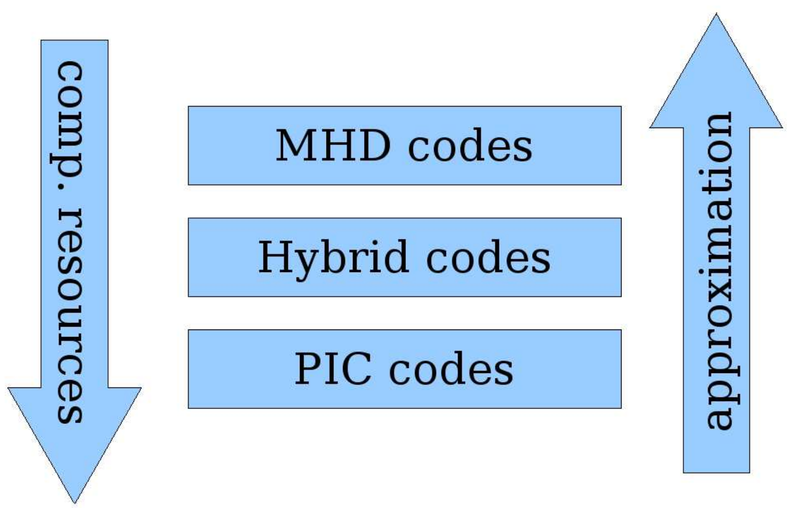

Figure 3.1: Plasma codes.

- Magnetic field is sub-stepped using modified midpoint method [*Press et al.*, 1992] for better time resolution and to prevent dispersion.

Because solving the Vlasov equation directly is often intractable we can discretize the distribution function f into a set of particles which represent f sufficiently well. It is possible to go even further by exploiting that electrons are much lighter than ions and thus very mobile. Then, their only function is to maintain the plasma charge-neutral for which a fluid-electron description is adequate. Such a system is governed by Vlasov-fluid equations given by:

$$\frac{\mathrm{d}\mathbf{x}_s}{\mathrm{d}t} = \mathbf{v}_s \tag{3.1}$$

$$\frac{\mathrm{d}\mathbf{v}_s}{\mathrm{d}t} = \frac{q_s}{m_s}(\mathbf{E} + \mathbf{v}_s \times \mathbf{B}) \tag{3.2}$$

$$\frac{\partial \mathbf{B}}{\partial t} = -\nabla \times \mathbf{E} \tag{3.3}$$

$$\nabla \times \mathbf{B} = \mu_0 \mathbf{J} \tag{3.4}$$

$$n_e m_e \frac{\mathrm{d}\mathbf{u}_e}{\mathrm{d}t} = -n_e e\mathbf{E} + \mathbf{J}_e \times \mathbf{B} - \nabla p_e \tag{3.5}$$

$$p_e = n_e k_B T_e, \tag{3.6}$$

where the symbols in the above represent: ion position $\mathbf{x}_s$; ion velocity $\mathbf{v}_s$; ion mass m_s; ion charge q_s; electric field $\mathbf{E}$; magnetic field $\mathbf{B}$; magnetic permeability μ_0; current density $\mathbf{J}$; electron number density n_e; electron mass m_e; electron fluid velocity $\mathbf{u}_e$; magnitude of electronic charge e; electronic current density $\mathbf{J}_e = -n_e e \mathbf{u}_e$; electron fluid pressure p_e; Boltzmann's constant k_B; and electron temperature T_e. The subscript s refers to the ion species. Darwin's approximation is used so that the displacement current is neglected in Maxwell's equation 3.4 and a massless electron fluid is assumed so that the left-hand term of equation 3.5 can be neglected. By adding a term $\eta\mathbf{J_e}$ on the right-side of equation 3.5, where η is resistivity of plasma, an artificial resistivity can be introduced into the system which causes damping of high frequency waves that would interact with electrons. In the real situation, Eq. 3.6 describing isotropic and isothermal plasma is not valid and the adiabatic approximation is made by substituting electron temperature T_e by $T_e = T_{e0}(n_e/n_{e0})^{\gamma-1}$, where γ is an adiabatic index.

Note that the electric field can be evaluated as a function of current density, magnetic field, charge density and electron pressure if we combine 3.4 and 3.5 and substitute electron current density by $\mathbf{J} = \mathbf{J}_e + \mathbf{J}_i$ and charge density by $\rho_c = n_s q_s$

$$\mathbf{E} = -\frac{\mathbf{J}_i \times \mathbf{B}}{\rho_c} + \frac{(\nabla \times \mathbf{B}) \times \mathbf{B}}{\mu_0 \rho_c} - \frac{\nabla p_e}{\rho_c} + \mu(\nabla \times \mathbf{B}). \tag{3.7}$$

Note that we added last term on the right side, representing artificial resistivity, to model magnetic field diffusion. This term will smooth short wavelength of magnetic field. Constant μ is typically less than 0.1. In the low density regions (e.g. tail of the planet) the density may drop bellow a critical value which results in the very strong electric field. When such situation occurs we turn off the terms which have ρ_c in the denominator because they become non-physical. Substituting above equation into equation 3.3 gives the method for advancing the magnetic field given by

$$\frac{\partial \mathbf{B}}{\partial t} = \nabla \times \frac{\mathbf{J}_i \times \mathbf{B}}{\rho_c} - \nabla \times \frac{(\nabla \times \mathbf{B}) \times \mathbf{B}}{\mu_o \rho_c} \tag{3.8}$$

The other variables used in CAM-CL code are defined as follows

$$n_s = \int f_s(\mathbf{x}_s, \mathbf{v}_s)\ \mathrm{d}\mathbf{v}_\mathrm{s}, \tag{3.9}$$

is the density and f is distribution function. The bulk velocity, charge density, mass density, current of ion species and total current are given, respectively, by:

$$\mathbf{u}_s = \frac{1}{n_s} \int \mathbf{v}_s f_s(\mathbf{x}_s, \mathbf{v}_s)\, \mathrm{d}\mathbf{v}_\mathrm{s} \tag{3.10}$$

$$\rho_c = \sum_s n_s q_s \tag{3.11}$$

$$\rho_m = \sum_s n_s m_s \tag{3.12}$$

$$\mathbf{J}_s = q_s n_s \mathbf{u}_s \tag{3.13}$$

$$\mathbf{J}_i = \sum_s \mathbf{J}_s \tag{3.14}$$

$$\mathbf{J} = \mathbf{J}_i + \mathbf{J}_e. \tag{3.15}$$

All variables are calculated at the corner of the computational cell except of electric field which is stored at the centre of the cell. In the following subsections we will describe all numerical methods used to advance the code into the next time level. Note that all methods are second order accurate.

3.1.2 Particle advancing

Only the ion velocity $\mathbf{v}_s$ is kept and its position $\mathbf{x}_s$ in the different time levels t and $t + 1/2\triangle t$, respectively, which allows use of the leapfrog algorithm as follows: First, the velocity is evaluated a half timestep ahead to obtain a best estimate for velocity

$$\mathbf{v}_s^{1/2} = \mathbf{v}_s^0 + \frac{\triangle t}{2}\frac{q}{m}\left(\mathbf{E}^{1/2} + \mathbf{v}_s^0 \times \mathbf{B}^{1/2}\right) \tag{3.16}$$

and then the solution over an entire step is obtained by using the best estimate of velocity $\mathbf{v}_s^{1/2}$ as follows

$$\mathbf{v}_s^1 = \mathbf{v}_s^0 + \triangle t\frac{q}{m}\left(\mathbf{E}^{1/2} + \mathbf{v}_s^{1/2} \times \mathbf{B}^{1/2}\right). \tag{3.17}$$

When the velocity is known in time step 1 the position of the particle can be advanced in time using

$$\mathbf{x}_s^{3/4} = \mathbf{x}_s^{1/2} + \triangle t\mathbf{v}_s^1, \tag{3.18}$$

where $\mathbf{v}_s^1$ is already known from the previous step.

3.1.3 Magnetic field and current density advancing

In the hybrid code, the magnetic field is advanced using equation 3.8. The same leapfrog technique is used as in the velocity advancing described in *Press et al.* [1992], which is a modified midpoint method. Two copies of the magnetic field vector are kept in order to leapfrog one over the other. We substep magnetic field with time step $\triangle t_B = \triangle t/n$, where n is typically 10. This allows us to resolve higher frequency changes in the magnetic field. Because the magnetic field is a function of the electric field we need to evaluate the electric field in each sub-step. So the magnetic field is advanced by

$$
\begin{aligned}
B_1 &= B_0 - \triangle t_B \nabla \times E_0 \\
B_2 &= B_1 - 2\triangle t_B \nabla \times E_1 \\
&\dots \\
B_{p+1} &= B_{p-1} - 2\triangle t_B \nabla \times E_p \\
&\dots \\
B_n &= B_{n-2} - 2\triangle t_B \nabla \times E_{n-1} \\
B_p^* &= B_{n-1} - \triangle t_B \nabla \times E_n,
\end{aligned} \tag{3.19}
$$

where odd subscripts together with B^* represents one copy of the field and even subscripts represent the second copy of the magnetic field. At the end of the field advancing step we can average two copies of the field or use the difference between B^* and B_n as a measure of the error and change the number of substeps dynamically.

To evaluate electric field during the processes of advancing

$$E_p = E(\rho_c^{1/2}, J_i^{1/2}, B_p, T_e), \tag{3.20}$$

we require current density J_i to be known at the time level 1/2. Because velocity of particles is not known at time level 1/2, it is necessary to approximate the current density by advancing it from $J_i^* = J(v_i^0, x_i^{1/2})$ into $J_i^{1/2}$ using moment equation

$$J_i^{1/2} = J_i^* = \frac{\triangle t}{2}(\Lambda E^* + \Gamma B^{1/2}), \tag{3.21}$$

where Λ and Γ are defined as

$$\Lambda = \sum_s \phi_{sj}^{1/2} \frac{q_s^2}{m_s} \tag{3.22}$$

$$\Gamma = \sum_s \phi_{sj}^{1/2} \frac{q_s^2}{m_s} v_x^0, \tag{3.23}$$

and ϕ is a weighting function $\phi(\mathbf{x}_s)$. Weighting function, in most cases, is a linear

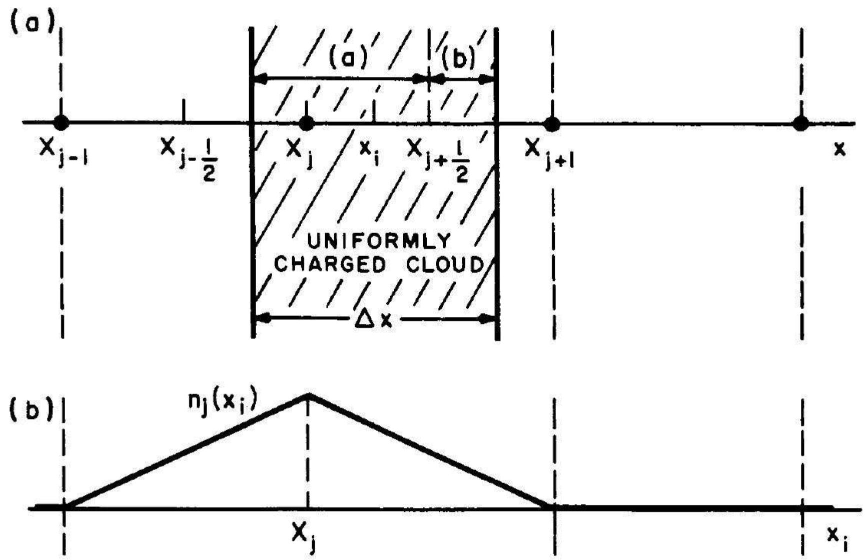

Figure 3.2: Example of weighting functions a) delta function, b) linear weighting function. Courtesy by *Birdsall and Langdon* [1985].

basis function depicted on Fig. 3.2b) and defined in the case of 2D by

$$
\begin{aligned}
\phi(0,0) &= (1-x)(1-y) \\
\phi(1,0) &= x(1-y) \\
\phi(1,1) &= xy \\
\phi(0,1) &= (1-x)y. \qquad (3.24)
\end{aligned}
$$

Variables x and y are normalized distance $(x, y) \in [0,1] \times [0,1]$ and parameter 0 and 1 represent the vertex of the computational cell. The other weighting functions commonly used include the Gaussian function which can improve energy conservation and lower the noise in exchange for more expensive calculations which involves evaluation of exponential function.

3.1.4 Main Loop

Fig. 3.3 is a schematic representation of the steps described above. Lets assume we are given these variables at the beginning of the simulation: $x^{1/2}$, v^0, ρ_c^0, $\rho_c^{1/2}$, J_i^0, Λ, Γ and $J_i^+ = J_i^*(x^{1/2}, v^0)$ where electron temperature T_e is a constant. To advance

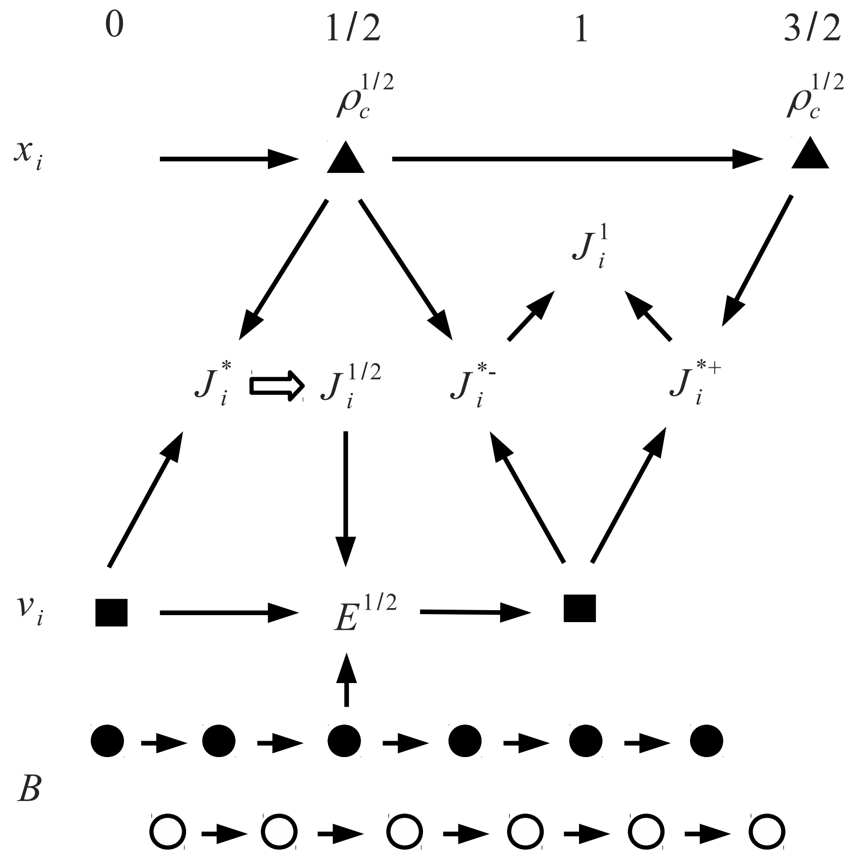

Figure 3.3: Schematic representing loop of CAM-CL code.

simulation into next time step we need to perform following operations.

Advance magnetic field B^0 into $B^{1/2}$, make an estimate of current density by advancing J_i^* into $J_i^{1/2}$ to get electric field $E^{1/2}$

$$
\begin{aligned}
B^{1/2} &= B^0 - \int_0^{\triangle t/2} \nabla \times E(\rho_c^0, J_i^0, B(t), T_e)dt \\
E^* &= E(\rho_c^{1/2}, J_i^0, B^{1/2}, T_e) \\
J_i^{1/2} &= J_i^* + \frac{\triangle t}{2}(\Lambda E^* + \Gamma \times B^{1/2}) \\
E^{1/2} &= E(\rho_c^{1/2}, J_i^{1/2}, B^{1/2}, T_e).
\end{aligned}
$$

Advance particles (v^1, $x^{3/2}$) and collect moments of distribution function.

$$\begin{aligned}
v_s^{1/2} &= v_s^0 + \frac{\triangle t}{2}\frac{q}{m}(E^{1/2} + v_s^0 \times B^{1/2}) \\
v_s^1 &= v_s^0 + \triangle t \frac{q}{m}(E^{1/2} + v_s^{1/2} \times B^{1/2}) \\
x_s^{3/4} &= x_s^{1/2} + \triangle t v_s^1
\end{aligned}$$

$$\begin{aligned}
\rho_c^{3/2} &= \rho_c(x^{3/2}) \\
J_i^- &= J_i^*(x^{1/2}, v^1) \\
J_i^+ &= J_i^*(x^{3/2}, v^1) \\
\Gamma &= \Gamma(x^{3/2}, v^1) \\
\Lambda &= \Lambda(x^{3/2}, v^1).
\end{aligned}$$

From these variables we can easily obtain ρ_c^1 and J_i^1 by taking average and finish advancing of magnetic field into time level B^1

$$\begin{aligned}
\rho_c^1 &= \frac{1}{2}(\rho_c^{1/2} + \rho_c^{3/2}) \\
J_i^1 &= \frac{1}{2}(J_i^- + J_i^+) \\
B^1 &= B^{1/2} - \int_{\triangle t/2}^{\triangle t} \nabla \times E(\rho_c^1, J_i^1, B(t), T_e) dt.
\end{aligned}$$

Because we expected the position at the beginning of the main loop to be already at $x^{1/2}$ we have to perform initial and the final steps before and after each output of variables into the file. The initial step is

$$
\begin{aligned}
\rho_c^0 &= \rho_c(x^0) \\
J_i^0 &= J_i^*(x^0, v^0) \\
x_s^{1/2} &= x_s^0 + \frac{\triangle t}{2} v_s^0 \\
\rho_c^{1/2} &= \rho_c(x^{1/2}) \\
J_i^+ &= J_i^*(x^{1/2}, v^0) \\
\Gamma &= \Gamma(x^{1/2}, v^0) \\
\Lambda &= \Lambda(x^{1/2}, v^0),
\end{aligned}
$$

and the final step is

$$
\begin{aligned}
x_s^1 &= x_s^{3/2} - \frac{\triangle t}{2} v_s^1 \\
\rho_m^1 &= \rho_m(x^1) \\
u_i^1 &= u_i(x^1, v^1).
\end{aligned}
$$

3.1.5 Model Scaling

It is convenient to scale the simulation in physically correct units (i.e. *hybrid units*). By taking protons of the solar wind as a reference species to express the variables in hybrid units. If we mark the simulation units by index H and physical units by SI then each variable x can be expressed $[x]_{\mathrm{H}} = [x]_{\mathrm{SI}}/u$ where u is physical unit of interest. We can adopt mass of the proton m_p as a unit of mass and charge e as unit of charge. All other *hybrid units* can be expressed as follows: unit of magnetic field B_0 (magnetic field of solar wind); unit of speed v_A the Alfvén velocity; unit of time Ω_{p0} (solar wind proton cyclotron time); unit of length $\Lambda_{p0} = c/\omega_{pi} = v_A/\Omega_{p0}$ (inertial length); unit of charge density $n_{p0}e$; unit of electric field $v_A B_0$; unit of energy $\rho_m (c/\omega_{p0})^3 v_A^2$ where c is the speed of light, $\Omega_{p0} = eB_0/m_p$ is solar wind proton gyrofrequency, and $\omega_{pi}^2 = n_0 e^2/\epsilon_0 m_p$ is ion plasma frequency. Note that in hybrid units we keep magnetic permeability $\mu_0 = 1$, ion beta

$$
\beta_s = \frac{p_s}{p_B} = \frac{v_{th,s}^2\, \rho_{m,s}}{v_A^2\, \rho_m}, \tag{3.25}
$$

electron beta $\beta_e = 2\tau_e$, and the speed of sound

$$c_s^2 = \frac{p_i + p_e}{\rho_m} = \frac{1}{2}(\beta_i + \beta_e)^2 v_A^2, \tag{3.26}$$

where $\tau_e = k_B T_e/e$ is a measure of the electron temperature. The Alfvén velocity v_A is defined as

$$v_A^2 = \frac{B^2}{\mu_0 \rho_m}. \tag{3.27}$$

3.1.6 Electric diffusion term

In order to avoid the artifacts of increased electric field on the grid size scale we incorporated electric diffusion term into the Equation 3.7 for electric field calculation in the form:

$$(-1)^{n+1}\mu_v \nabla^n \mathbf{E}, \tag{3.28}$$

where n is the order of diffusion and μ_v is constant determining the strength of damping. In our code we implemented 4^{th} order diffusion because only 2 grid cells are available at the edge of computation domain of each processor. Note that constant μ_v has spatial units so we have to adjust the value for different spatial resolution manually.

3.1.7 Boundary conditions

Open boundary conditions (BC) are hard to implement in the hybrid code because we are required to impose the BC on both the electric field as well as the particle population. Here, we choose to follow the suggestion of *Umeda et al.* [2001] to implement a field masking in order to attenuate the wave perturbations at the boundaries. The idea is to allow advancing the EM fields only in the internal region of the simulation box and keep the initial values of the field close to the border. This method creates a buffer around the boundary which is successful to damp the most of the power of the incoming waves.

We can rewrite the Equation 3.3 in the discretized form using the finite difference method as follows

$$\mathbf{B}^1 = \mathbf{B}^0 - dt f_m (\nabla \times \mathbf{E})^{1/2}, \tag{3.29}$$

where dt is the time step and f_m is a masking function. *Umeda et al.* [2001] suggested to use a polynomial function of second order

$$f_m = 1 - \left(r \frac{|x| - L/2}{L_D} \right)^2, \tag{3.30}$$

with r and L_D parameters determine a shape of the buffer region. In our experience, a polynomial dependence is not sufficient to damp the incoming waves and thus we used an exponential function which is more effective but also more computationally expensive.

$$f_m = 1 - \exp \left[- \frac{L_x - x}{L_D} \right]^n. \tag{3.31}$$

We obtain the good results with $n = 1$ and $L_D = 10c/\omega_p$. The same masking function is used around the planet of the global simulations but with the smaller parameter L_D of 2.

A similar procedure can be applied to the electric field calculation. If we set a newly calculated electric field from equation 3.7 as E^* then the newly calculated electric field E^{new} can be expressed from the old value E^{old} as follows

$$E^{\text{new}} = E^{\text{old}} + f_m(E^* - E^{\text{old}}), \tag{3.32}$$

where masking coefficient f_m represents the same function which was defined above.

3.1.8 Implementation

We implemented the code using the C++ programming language and we used the template programming technique to write a single source code for all three variants (1D-3D) of the code. It is left to the compiler to generate an executable for the requested version based on the input from a user. It is important to use a compiler which can optimize the code for speed.

We support both OpenMP and Message Passing Interface (MPI) types of the parallelization, although for the large-scale simulations, like the global model of Mercury, only MPI is feasible. The MPI parallelization is implemented using a domain decomposition paradigm. After the code execution, the total number of available CPUs is determined and it is split semi-equally along all spatial axis in such a way that every CPU is assigned an equal size of the spatial sub-domain. This approach requires the particles to move freely across the boundaries of the domain and to communicate the boundary values of all field variables. The advantage of this approach is simple and straight forward implementation. The disadvantage is a poor load balancing. In the situation when the plasma accumulates at one spatial region (e.g. in front of the planet), the CPU which is assigned to that region becomes overloaded compared to the rest of the CPUs which are idly waiting during a synchronization routine.

The code stores the important variables to the disk for the later data analysis at a specified time interval. For each of the following variables a separate file is created: the magnetic and electric fields, the density, the bulk velocity and the perpendicular and parallel temperatures with respect to the background magnetic field. Unfortunately, the code does not store the distribution function of the particles but this information could be retrieved from the checkpoint data files used for restart of the simulation. All variables are stored using the HDF5 data format designed specifically for storage of scientific data. An advantage of using HDF5 file format is the computer architecture independence and the ability to write to the file in parallel or apply compression algorithms seamlessly. An another important advantage over the standard binary output is that the format is supported by all major data analysis packages (like Matlab, IDL, etc.).

3.2 Linear theory solver

A validation of the numerical code described in the previous sections is an important prerequisite for a successful application. In this section we will outline a simplified analytic model of wave particle processes captured by our hybrid model. The mathematical model will be useful in the following chapter for testing of the code.

Linear kinetic theory allows a study of the plasma waves and their interaction with particles (i.e. wave-particle interaction). Here, we briefly summarize the equations which are needed to describe the case of a propagating wave in the direction parallel to constant and the uniform magnetic field. The standard approach, followed here, involves solving the linearized system of the Maxwell's equations and the particle phase space density $f(\mathbf{v}, \mathbf{x}, t)$. The latter is defined by the Vlasov equation, which is the equation derived from the Boltzmann's equation under the assumption of collisionless plasma. This assumption is valid in the majority of space plasma, especially in the magnetospheric region of interest (L>2). The Vlasov equation is given by

$$\frac{\partial f}{\partial t} + \mathbf{v} \cdot \nabla_x f + \frac{q}{m}(\mathbf{E} + \mathbf{v} \times \mathbf{B}) \cdot \nabla_v f = 0. \tag{3.33}$$

When $\mathbf{k} \times \mathbf{B}_0 = 0$ we can incorporate the effects of the temperature anisotropy and the drift velocity into a single dispersion relation given by Equation 3.34. Here we assumed that the particle distribution function f is bi-Maxwellian. We followed approach and notation of *Gary* [1993] to obtain the dispersion relation:

$$\omega^2 - k^2c^2 + k^2c^2 \sum_j S_j^{\pm}(\mathbf{k}, \omega) = 0, \tag{3.34}$$

where

$$S_j^{\pm}(\mathbf{k}, \omega) = \frac{\omega_j^2}{k^2c^2}\left[\zeta_j^2 Z(\zeta_j^{\pm 1}) - \frac{1}{2}\left(\frac{T_{\perp j}}{T_{\| j}} - 1\right) Z'(\zeta_j^{\pm 1})\right], \tag{3.35}$$

ζ is the doppler-shifted wave phase speed given by

$$\zeta_j^m = \frac{\omega - \mathbf{k}\cdot\mathbf{v}_{0j} + m\Omega_j}{\sqrt{2}|k_z|v_j}. \tag{3.36}$$

Here $T_\perp$ and $T_\|$ are the perpendicular and the parallel temperature directions with respect to the background magnetic field, respectively, Ω_j is gyro-frequency of species j and v_j is a thermal velocity. Function Z is the plasma dispersion function, defined as

$$Z(\zeta) = \frac{1}{\sqrt{\pi}} \int_{-\infty}^{\infty} \mathrm{d}x \frac{\exp(-x^2)}{x - \zeta}. \tag{3.37}$$

Note that ζ is a complex variable and the integration follows the Landau contour, i.e. the path of integral passes below singularity at $x = \zeta$. Derivative of plasma dispersion function is given by

$$Z'(\zeta) = -2[1 + \zeta Z(\zeta)]. \tag{3.38}$$

We solved Equation 3.34 numerically by searching for the complex roots ($\omega = \omega_r + i\gamma$) assuming $k_\| > 0$ using "hybrids" multidimensional solver GNU GSL library (http://www.gnu.org/software/gsl/). Dispersion relation 3.34 include all anisotropy, bump-on-tail and electromagnetic waves and instabilities for multi-species plasma when $\mathbf{k} \times \mathbf{B}_0 = 0$, i.e. waves propagating parallel to background magnetic field. Equation 3.34 can be solved analytically only in the limit of $|\gamma| \ll |\omega_r|$ when plasma has (bi)Maxwellian distribution.

In the next chapter we will present the simulation runs with the initial parameters chosen to excite the plasma waves which can be tested against the linear dispersion relation described in this section. The test of the code against well known physical processes is a necessary step towards the more elaborate simulations like the global model of Mercury. Because the above mathematical model describes only the waves with parallel propagation, we will test the perpendicular properties of the code against the result published in literature.

Bibliography

Birdsall, C. K., and A. B. Langdon, *Plasma Physics via Computer simulations*, Graw-Hill, New York, 1985.

Gary, S. P., *Theory of Space Plasma Microinstabilities*, Cambridge Univ. Press, 1993.

Harned, D. S., Quasineutral hybrid simulation of macroscopic plasma phenomena, *J. Comput. Phys.*, *47*, 452–462, 1982.

Horowitz, E. J., D. E. Shumaker, and D. V. Anderson, QN3D: A three-dimensional quasi-neutral hybrid particle-in-cell code with applications to the tilt mode instability in field reversed configurations, *J. Comput. Phys.*, *84*, 279–310, 1989.

Lipatov, A. S., *The Hybrid Multiscale Simulation Technology: an introduction with application to astrophysical and laboratory plasmas*, Springer, 2002.

Matthews, A., Current advance method and cyclic leapfrog for 2D multispecies hybrid plasma simulations, *J. Comput. Phys.*, *112*, 102–116, 1994.

Press, W. H., S. A. Teukolsky, W. T. Vetterling, and B. P. Flannery, *Numerical Recipes*, Cambridge Univ. Press, Oakleigh, 1992.

Trávníček, P. M., P. Hellinger, and D. Schriver, Structure of Mercury's magnetosphere for different pressure of the solar wind: three dimensional hybrid simulations, *Geophys. Res. Lett.*, *34*, L05,104, 2007.

Umeda, T., Y. Omura, and H. Matsumoto, An improved masking method for absorbing boundaries in electromagnetic particle simulations, *Comput. Phys. Comm.*, *137*, 286–299, 2001.

Winske, D., Hybrid simulation codes with application to shocks and upstream waves, *Space Sci. Rev.*, *42*, 53–66, 1985.

Winske, D., and N. Omidi, Hybrid codes: Methods and application, in *Computer Space Plasma Physics: Simulation Techniques and Software*, edited by H. Matsumoto and Y. Omura, pp. 103–160, Terra Scientific Publishing Company, Tokyo, 1993.

Winske, D., and N. Omidi, A nonspecialist's guide to kinetic simulations of space plasmas, *J. Geophys. Res.*, *101*, 17,217–287,304, 1996.

Chapter 4

Code Testing

In this chapter we discuss the tests which validate the hybrid numerical code described in the previous chapter. The following aspects of the codes are tested against the linear kinetic theory and the results published in the technical literature: (1) we start with validating an analytic model of the plasma waves based on the linear dispersion function which includes several ion species against the results of *Li and Habbal* [2005] paper which discuss the generation of ectromagnetic waves of coronal plasma; (2) the ion cyclotron and the bump-on-tail plasma micro-instabilities which test the code's performance against well established the linear dispersion relation derived from the kinetic theory and energy conservation over time; (3) The Kelvin-Helmholtz instability (KHI) was chosen to better understand the results from global modelling of the planet Mercury. The KHI is set up and tested against the results from *Rankin et al.* [1993]; (4) the stability of magnetic dipole moment placed in stationary, isotropic and uniform plasma which we will require for global numerical modelling; and (5) in the last section, we will explore the properties of numerical heating to probe the input parameter space in search for the initial conditions which are physically correct. To validate the code against the published work and theoretical predictions is a crucial step in using numerical model to study physical processes.

4.1 Linear Dispersion Solver Test

In this section we will validate a numerical solver of linear dispersion relation derived from the kinetic theory. The mathematical model is described in the Section 3.2. The correct behaviour of the linear dispersion solver will be necessary to validate the nu-

species	m/m_p	q/e	n/n_e	$\beta_\parallel$	$T_\perp/T_\parallel$	$v_{0\parallel}/v_A$
e^-	1/1836.15	-1	1.0	0.005	1	0
H^+	1	1	0.92495	0.005	1	0
O^{+5}	15.9994	5	0.00001	0.005	1	0
Li^+	6.941	1	0.075	0.5	9	1

Table 4.1: Parameters for linear theory solver and hybrid code simulation.

merical results from the hybrid-kinetic model. Here, we will analyze a stability of multi-species plasma by reproducing the work of ***Li and Habbal*** [2005]. They studied the interaction of protons with admixture of heavy ion species and electromagnetic ion-cyclotron (EMIC) waves. The article cited above used linear dispersion solver to study the plasma mixture consisting of protons H$^+$, Oxygen O^{+5} with $n_{O^{+5}}/n_e = 10^{-5}$ and Lithium Li$^+$ with $n_{Li^+}/n_e = 0.075$ and the temperature anisotropy $T_\perp/T_\parallel$= 9 and $v_{0\parallel}/v_A$= 1. Other parameters are summarized in the Table 4.1. The authors set up the model as a 1D simulation box with the magnetic field B_0 aligned along the spatial axis and they assumed that lithium species with large anisotropy will excite EMIC waves through the ion-cyclotron instability which in turn will interact with the isotropic protons and the oxygen ions. Since the oxygen has very low density, O^{+5} will act solely as the test particles and will not contribute to the wave generation. The lithium ions have nonzero parallel velocity so that only the parallel propagating waves have strong interaction with the oxygen but the anti-parallel waves interact only weakly.

First, we solved for the dispersion relation using the linear theory solver developed earlier and described in the section 3.2. Figure 4.1 represents real solution ω (solid curve) and the growth rate γ (dashed curve). From the linear theory prediction, we concluded that the waves with kc/ω_p< 1.6 will be unstable. The maximal growth rate of the waves is expected for kc/ω_pin the range between 0.2 and 0.3. The curves of $w = w(k)$ are in good agreement with the results of ***Li and Habbal*** [2005] and thus in the later sections we will use our linear dispersion solver unless stated otherwise.

4.2 Micro-instabilities

To validate physical behavior of the hybrid code we run the simulations using unstable plasma conditions and compare the results with predictions of the linear kinetic theory solver which we described in Chapter 3. Our implementation of hybrid code resolves

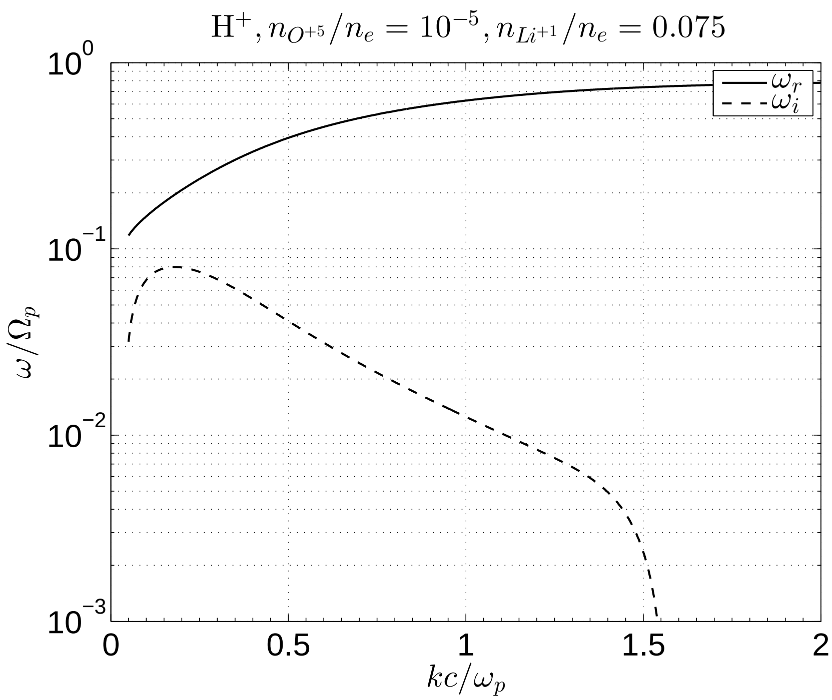

Figure 4.1: Dispersion relation using linear theory for plasma consisting of protons H^{+}, Oxygen O^{+5} with $n_{O^{+5}}/n_e = 10^{-5}$ and Lithium Li^{+} with $n_{Li^{+}}/n_e = 0.075$ and the temperature anisotropy $T_{\perp}/T_{||}$= 9. Solid line represents real solution ω and dashed line represents a growth rate γ.

the wave-particle interactions self-consistently and thus non-linear effects are fully included. Initial evolution of the system can be described mathematically using linear kinetic theory. This allows us to compare the hybrid code against the well-known problems of micro-instabilities which play an important role in study of space plasma.

Here we choose the ion cyclotron and the bump-on-tail instabilities because of its simplicity to set up the initial conditions by changing the values in the input file without need to recompile the source code. The parameters of two simulation runs are summarized in Table 4.2 and they have been chosen to allow only slow growth of the instability over time. To evolve the simulation into the non-linear stage we run the code for longer simulation times (i.e. $t_{\max}\Omega_p = 200$). This procedure allowed us to examine the energy conservation properties of the code by recording the kinetic energy of the particles and compare the value with the energy stored in the electromagnetic fields.

	Ion Cyclotron	Bump-on-Tail	
$\triangle t\ \Omega_p$	0.02	0.02	
$\triangle x\ \omega_p/c$	0.1	0.1	
$L_x\ \omega_p/c$	1024	1024	
β_e	0.1	0.00055	
$\beta_{\parallel p}$	2.0	1.0	0.1
$T_\perp/T_\parallel$	2.0	1.0	1.0
n_s/n_e	1.00	0.97	0.03
q_s/m_s	1	1	1
v_{0x}	0	0	5
# particles/cell	500	3000	1000

Table 4.2: Parameter of 1D test simulations of micro-instabilities performed to test the code against the linear prediction.

4.2.1 Ion Cyclotron Instability

The ion cyclotron instability is driven by the positive temperature anisotropy (i.e. $T_\perp/T_\parallel > 1$) of the ion particle population. During the interaction between the anisotropic ions and the electromagnetic wave, free kinetic energy of the particles is transferred into the wave which carry energy further away from unstable region. This process consequently decrease the anisotropy of the particle distribution and forces the system into equilibrium. The ion cyclotron instability excite the left and the right hand polarized modes of the electromagnetic waves. While the left hand polarized branch is strongly resonant with the ions gyrating in the same sense the right hand branch is of no interest because of the weak interaction. We started with 1D simulation box and uniform bi-Maxwellian plasma, the proton anisotropy $A = 2$ and the proton plasma beta $\beta_{\parallel p} = 0.1$. To resolve large wave vectors we set the resolution to be $\triangle x\ \omega_p/c = 0.1$. We analyzed the results by performing 2D Fast Fourier transform (FFT) of the perpendicular component of the magnetic field with respect to the background field $\mathbf{B}_0$ oriented in the direction of the only spatial X-axis.

Figure 4.2 shows a result of 1D simulation initialized with the parameters from Table 4.2. Upper panel represents evolution of the magnetic field transformed into (ω, k) space using FFT. The lower (upper) solid line represents left (right) hand polarized EMIC wave, respectively and the dashed line represents a complex root γ of the left hand polarized branch (i.e. the growth rate). The bottom plot of Fig. 4.2 represents time evolution of energy stored in the magnetic field. The linear part of the curve (up to time $60\ \Omega_P^{-1}$) represents linear evolution of the instability when energy is

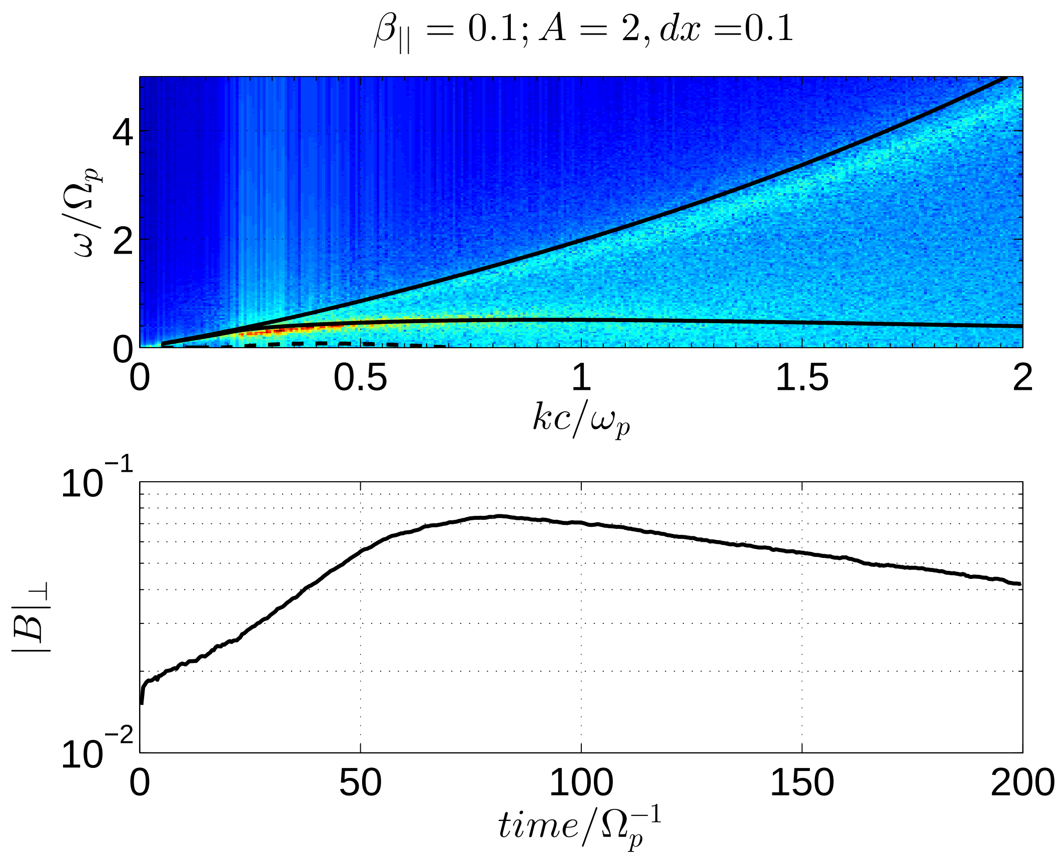

Figure 4.2: Simulated power spectrum of ectromagnetic wave excited by ion-cyclotron instability which was initialized with bi-Maxwellian plasma with $A = 2$; $\beta_{\|p} = 0.1$ and resolution $\triangle x = 0.1$

being converted from the particles into the wave energy by wave-particle interaction. Performing the simulations with different spatial resolution we found that the upper branch of the instability requires higher spatial resolution. By incrementally increasing the resolution we found that $\triangle x\ \omega_p/c = 0.1$ is sufficient to resolve the right hand polarized branch of EMIC waves correctly even for large k values.

4.2.2 Bump-on-Tail Instability

A second micro-instability which we choose to test our numerical code is the bump-on-tail instability. A bump on the tail of the distribution function is achieved by combining two species of equal charge and mass but different number density, temperature and most importantly bulk flow velocity. The resulting distribution function presented in

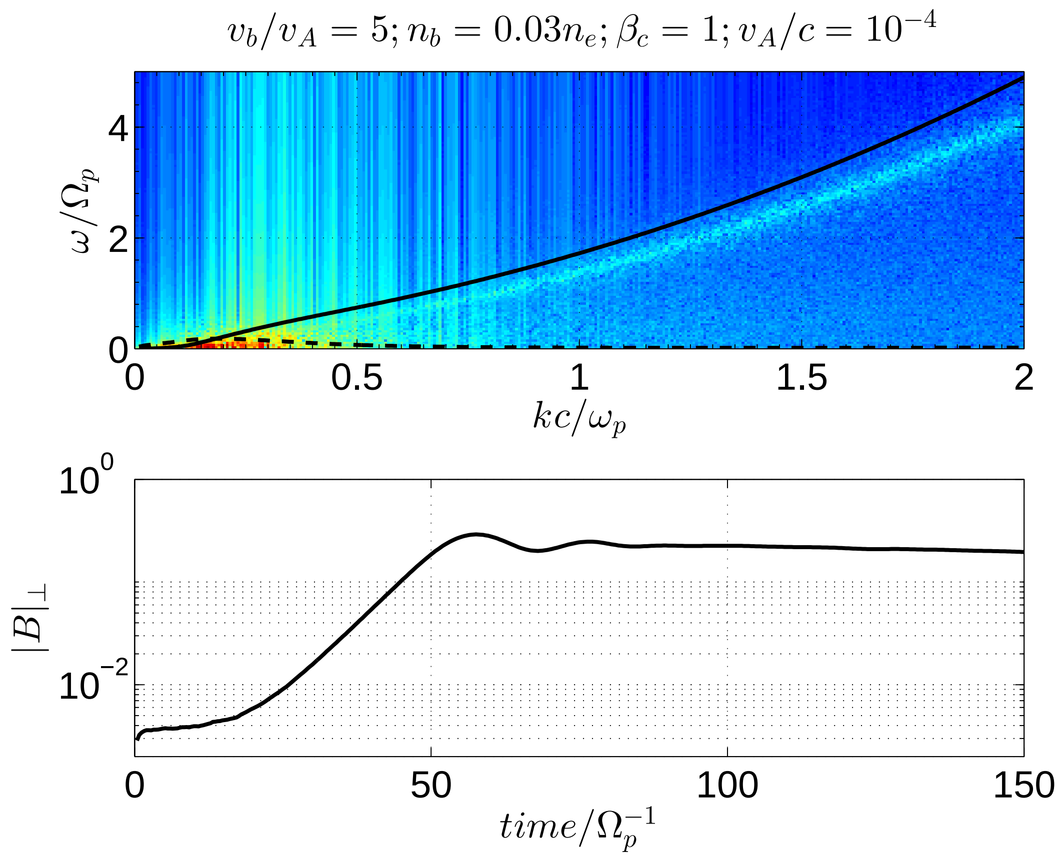

Figure 4.3: Power spectra of Bump-on-Tail 1D simulation initialized with core and bump components of Maxwellian plasma. The parameters are: $n_b/n_e = 0.03$; $v_b/v_A = 0.5$; and spatial resolution $\triangle x = 0.1$.

Fig. 4.4 is composed of a high density core and a beam populations. The quasi-neutrality condition requires us to keep the total number density of all ion species equal to the number density of electrons.

The initial parameters which we considered below satisfy the following conditions of maximal growth rate for right-hand resonant instability: core distribution has zero bulk velocity; number density of the beam is much smaller than the total density $n_b \ll n_e$ and velocity of the beam is higher than local Alfvén speed $v_A < v_b$. For beam instabilities with density of the beam in the range $0.01 \lessapprox n_b/n_e \lessapprox 0.1$, there is $\omega_r \approx \gamma$ near the wavenumber of maximal growth [*Gary*, 1993]. When the conditions above are satisfied we can approximate the growth rate of the right-hand resonant instability

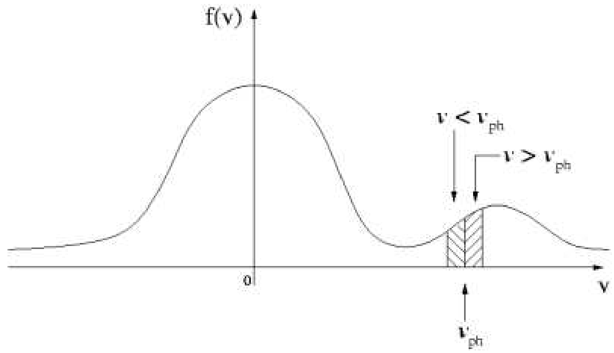

Figure 4.4: Example of distribution function used to set up Bump-on-Tail instability.

as

$$\frac{\gamma}{\Omega_i} \approx \left(\frac{n_b}{2n_e}\right)^{(1/3)}. \tag{4.1}$$

Fig. 4.3 summarize the results of Bump-on-Tail instability test. We initialized the simulation with core proton population of density $n_c/n_e = 0.97$; a beam with bulk velocity of $v_b/v_A = 5$ and the density $n_b/n_e = 0.03$. Note that the temperature of electron and core populations satisfy the condition $T_e = T_c$. The rest of the parameters is given in Table 4.2.

From the top contour plot of Fig. 4.3 we can see that the simulation follows the trend of linear prediction (a solid line) but it deviates for larger wave numbers. The reason can be either insufficient resolution (in this case $\triangle x = 0.1$) of the simulation box or non-linear effects are important and alter the dispersion relation. We can make following conclusions after the successful test simulations:

- The ion-cyclotron instability simulation proves that the code is capable of resolving anisotropy instability as predicted by linear kinetic theory.
- The results of bump-on-Tail simulation confirm correct implementation of support for multi-ion species. The multi-ion implementation is essential in simulating realistic plasma mixture of H^+, He^+, O^+.

4.3 Kelvin-Helmholtz Instability

We performed a 2D hybrid simulation of shear flow in uniform plasma which is unstable to the Kelvin-Helmholtz (KH) waves. Understanding the evolution of KH instability was helpful during the analysis of numerical results from global numerical model of magnetized bodies. The initial conditions were adopted from the manuscript by ***Rankin et al.*** [1993] to validate our code against the numerical results of MHD code. We expected only a weak wave-particle interaction because the instability was in the MHD regime and so the exponential growth rate closely followed the results from ***Rankin et al.*** [1993]. Note that more details on the structure of vortexes and the energy transfer between the wave and the kinetic energy of the fluid is given in a later paper ***Rankin et al.*** [1997].

Following the initial conditions from ***Rankin et al.*** [1993], we initialized our simulation with velocity profiles given by Equations 4.2 with the following parameters: $k_{xR} = 0.3\mathrm{R}_{\mathrm{E}}^{-1}$, $k_x = 6.8\mathrm{R}_{\mathrm{E}}^{-1}$, $v_A = 280$km/s, $\sqrt{2}v_0/e^{1/2}k_{xR}\triangle = 90$km/s, $\triangle = 0.18\mathrm{R}_{\mathrm{E}}$, $\varepsilon = 1.7$, $n_P = 10\mathrm{cm}^{-3}$, $|\mathbf{B}| = 40$nT, and $T_p = 100$eV.

$$
\begin{aligned}
v_x &= -\frac{v_0}{\triangle^2}\frac{2y}{k_{xR}}\exp\left(\frac{-y^2}{\triangle^2}\right) \\
v_y &= v_0\varepsilon\exp\left(\frac{-y^2}{\triangle^2}\right)\cos(k_x x).
\end{aligned} \tag{4.2}
$$

The authors choose the above parameters to study the interaction of Kelvin-Helmholtz instability with field line resonances. The magnitude of the shear flow was deduced from the projection of ionospheric flow observations onto the equatorial plane. Although proton temperature is lower than the one used in the article cited above, the numerical results are not affected because of the growth rate has a weak dependence on proton temperature T_p.

Although we used relatively high number of particles per single computation cell $N_p/N_c = 300$, a small constant ε limiting initial perturbation of velocity was not sufficiently high and we increased its value from 0.02 used by ***Rankin et al.*** [1993] to 1.7. This value was large enough to overcome higher numerical noise associated with hybrid codes. We used a 2D simulation box with periodic boundary conditions in both directions and fine spatial resolution of $dx = 0.2c/\omega_p$which is required to attenuate numerical noise. The numerical grid was composed of $N_x \times N_y = 250 \times 1000$ computational cells. The background magnetic field was uniform $\mathbf{B}_0 = B_z$ pointing out of the plane of the simulation. The density was also initialized uniformly in the entire simulation box.

Figure 4.5 is a graphical representation of Equations 4.2. We scaled the velocity

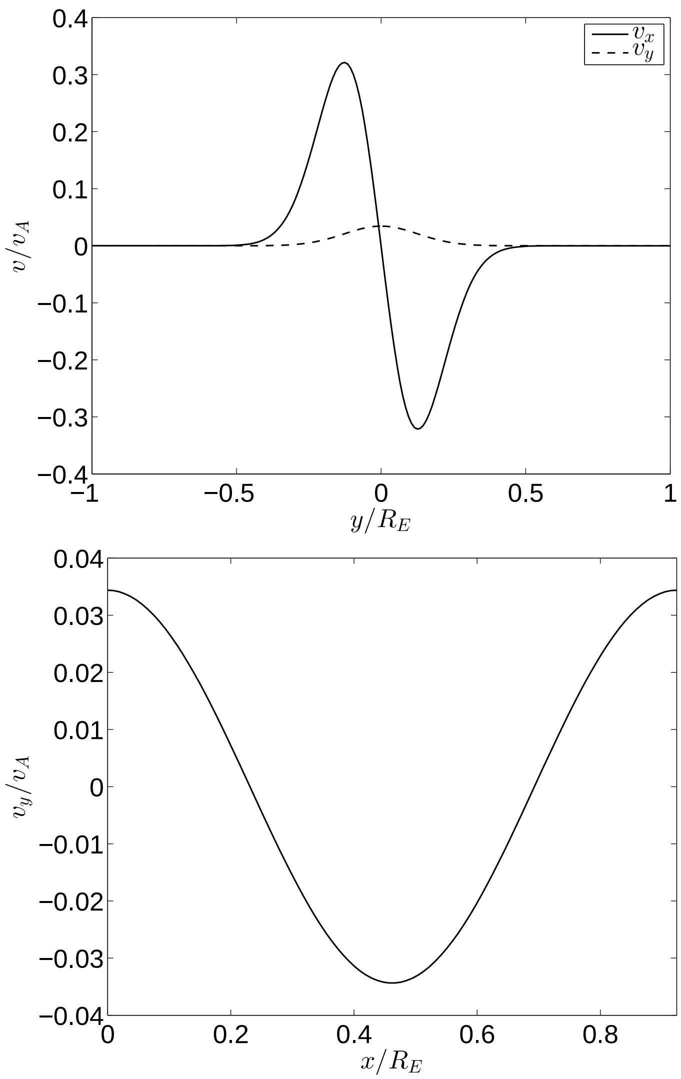

Figure 4.5: The initial bulk velocity profiles used to initialize Kelvin-Helmholtz instability based on ***Rankin et al.*** [1993]. All values are scaled to Alfvén velocity $v_A = 280$ km/s.

axis by Alfvén velocity $v_A = 280$km/s and thus max(v_x) = 90km/s. Note that a component of shear velocity v_x is a function of y-axis only but $v_y = v_y(x, y)$. A chosen velocity profile has three regions of velocity shear although only the central region is perturbed in y-direction.

Figure 4.6 presents the snapshots of numerical results at the simulation times t=26, 52, 78, 104, 130s. Top panels represent a perpendicular perturbation of the magnetic field $|B_\perp|$. Bottom panels show the perpendicular temperature $T_\perp$ with respect to the background magnetic field $\mathbf{B}_0$. Note that $T_\perp$ vary only slightly (between 0.185 and 0.205) during the simulation which suggests that wave-particle interactions are weak and thus support the conclusions of work by ***Rankin et al.*** [1993] which neglected kinetic processes by using MHD numerical model.

Figure 4.7 represents evolution of the physical system in time by inspecting variable max(v_y). Top panel shows the instability growth during the entire simulation time. The onset of the instability at the initial time is driven by a seed value ε. At the end of the linear stage $t\Omega_p = 60$, the instability saturates at a maximum value given by available free energy. Saturation and oscillatory behavior is characteristic for non-linear interactions. The bottom panel represents the initial time of exponential growth of the top curve on a logarithmic scale interpolated by a straight line. Slope of the best fit provides us with the growth rate of 0.034 s^{-1} which was in perfect agreement with the value reported by ***Rankin et al.*** [1993]. Please note that much lower proton temperature of 100 eV and kinetic effects included in our simulation were not important.

4.4 Equilibrium test

This test provide us with information about stability of the boundary conditions imposed on the edges of the simulation box and a surface of the planet which are particularly important for the global numerical model due to limited size of the simulation box. Long simulation runs require the boundary conditions to remain numerically stable with minimal non-physical interference to avoid contamination of the results. Although the planet's surface is discretized using the finite grid cells, the particles perceive the planet as a smooth sphere when they are reflected. We choose the sufficient resolution to minimize numerical instability caused by the discretization. Assuming the isotropic plasma and a stationary state, we can write the plasma equilibrium equation as

$$(\nabla \times \mathbf{B}) \times \mathbf{B} = \nabla P, \tag{4.3}$$

where $\nabla \times \mathbf{B} = \mathbf{J}$. When we substitute the magnetic dipole field for $\mathbf{B}$, the left hand side of the equation 4.3 becomes zero. Because $\nabla P = \nabla(nk_BT) = 0$, the dipole magnetic field, the uniform number density, and the plasma temperature are the sufficient conditions for the simulation to remain stable and stationary. More information on anisotropic configuration of plasma equilibrium can be found for example in

Cheng [1992] and *Cheng* [2003]. Figure 4.8 represents a color coded proton number density of the simulation at late simulation time of $t\Omega_{pi} = 300$. The density fluctuations visible in figure are only statistical noise which is a result of distribution function sampling. Over-plotted are the traces of the magnetic field lines which maintained its original topology over three hundred gyro-periods.

4.5 Numerical Heating

When running a numerical code for long period of time we must be cautious about numerical heating caused by inappropriate simulation parameters. Understanding a parameter space where the code operates without introducing artificial heating is of vital importance when interpreting the results. We performed several numerical tests of flowing uniform plasma in a 2D simulation box to estimate the correct parameters for the long simulation runs which are required for global modelling. In equilibrium plasma, the numerical heating may be observed as exponentially growing waves in all physical variables with a plateau at some maximal value. *Ueda et al.* [1994] estimated that amount of the numerical heating depends proportionally to the number of particles N_p per computational cell N_x as $(N_p/N_x)^{-1}$ and the spatial resolution $(\lambda_D/\triangle x)^{-3}$. Although the study above used an electrostatic particle code the relations are applicable to our model as well when we substitute λ_D for ion gyro-radius r_L, which is a typical spatial scale used in the hybrid code.

In this section we will use 2D simulation box filled with the isotropic Maxwellian plasma streaming in the positive x direction and the plasma parameters used for the global numerical model of Mercury. The following parameters are common to all simulation runs in this section: $\beta_e = 0.5$, $\beta_{\|p} = 0.4$, $T_\perp/T_\| = 1$, $n_s/n_e = 1$, $q_s/m_s = 1$, $v_{0x}/v_A = 7.39$. In theory, plasma with the above parameters is stable and it should remain constant over the time. The top panel of Figure 4.9 represents the proton number density at the late simulation time of $t/\Omega_p = 200$ in the $X - Y$ plane. Here, we used the initial parameters from the first simulation run of Table 4.5. It is clear that the waves observed in the density develop as the plasma propagates along the x axis. The bottom panel represents the same information in the $X - t$ plane. Initially uniform plasma develops a perturbation in the proton density.

Following *Ueda et al.* [1994], we performed 6 numerical simulations while keeping the plasma parameters same as in Figure 4.9 and changing the time step and the spatial resolution. The parameters of all simulation runs are given in Table 4.5. Figure

Run Number	$\triangle t\ \Omega_p$	$\triangle x\ \omega_p/c$	$L\ \omega_p/c$	# particles/cell
1	0.008	0.5	1000×200	140
2	0.008	0.5	1000×200	280
3	0.004	0.5	1000×200	280
4	0.004	0.25	2000×400	280
5	0.008	0.25	2000×400	140
6	0.008	0.5	1000×200	560

Table 4.3: The initial parameters for the study of the numerical heating. The other parameters which are common for all simulation runs include: $\beta_e = 0.5$, $\beta_{\|p} = 0.4$, $T_\perp/T_\| = 1$, $n_s/n_e = 1$, $q_s/m_s = 1$, $v_{0x}/v_A = 7.39$.

4.10 represents the results from all 6 simulations by measuring the perpendicular temperature over time. In the case of no artificial heating, the perpendicular temperature should remain constant at its initial value because the simulation is initialized with the plasma in equilibrium state. In Figure 4.10 we can see the perpendicular temperature being constant for the times $t/\Omega_p < 40$ which is equal to its initial value. Except of the runs 5 and 6, the temperature starts to grow exponentially up to $t/\Omega_p \approx 70$ and plateau at some maximal value determined by the length of the simulation box in the direction of the plasma flow. The results are in perfect agreement with *Ueda et al.* [1994] who concluded that increased spatial resolution is the most effective in reducing the numerical heating as follows $(r_L/\triangle x)^{-3}$.

4.6 Benchmark

In Section 3.1.8 we briefly described the parallel implementation of our hybrid code. Here, we will measure a performance of the code by performing the numerical simulations with increasing number of processors. We run a simple 2D simulation of the magnetic dipole in the solar wind on the grid of 640x640 cells.

Figure 4.11 represents speed up of the total execution time with increasing number of the processors compared to the first run of 64 processors. The test was performed on the IBM BlueGene/P supercomputer with 64, 256, 400, and 512 processing cores. Good scaling of the numerical code is important for global numerical model which require enormous computer power. For example, the simulations presented in the Chapter 5 were performed in IBM T.J. Watson Research Lab in Yorktown, NJ. We used 4096 computing cores of the BlueGene/P supercomputer to run the numerical model of the planet Mercury.

The code scaled better than linearly (represented by a dashed line) due to the efficient use of the CPU cache. This is true especially in initial phase of the simulation when the plasma is distributed uniformly. From our experience, the code's performance suffers when particles redistribute in space non-uniformly. In the case of the global model of Mercury, plasma accumulates at the nose of the planet which causes the processing cores which are assigned to that location to become overloaded due to the lack of load balancing.

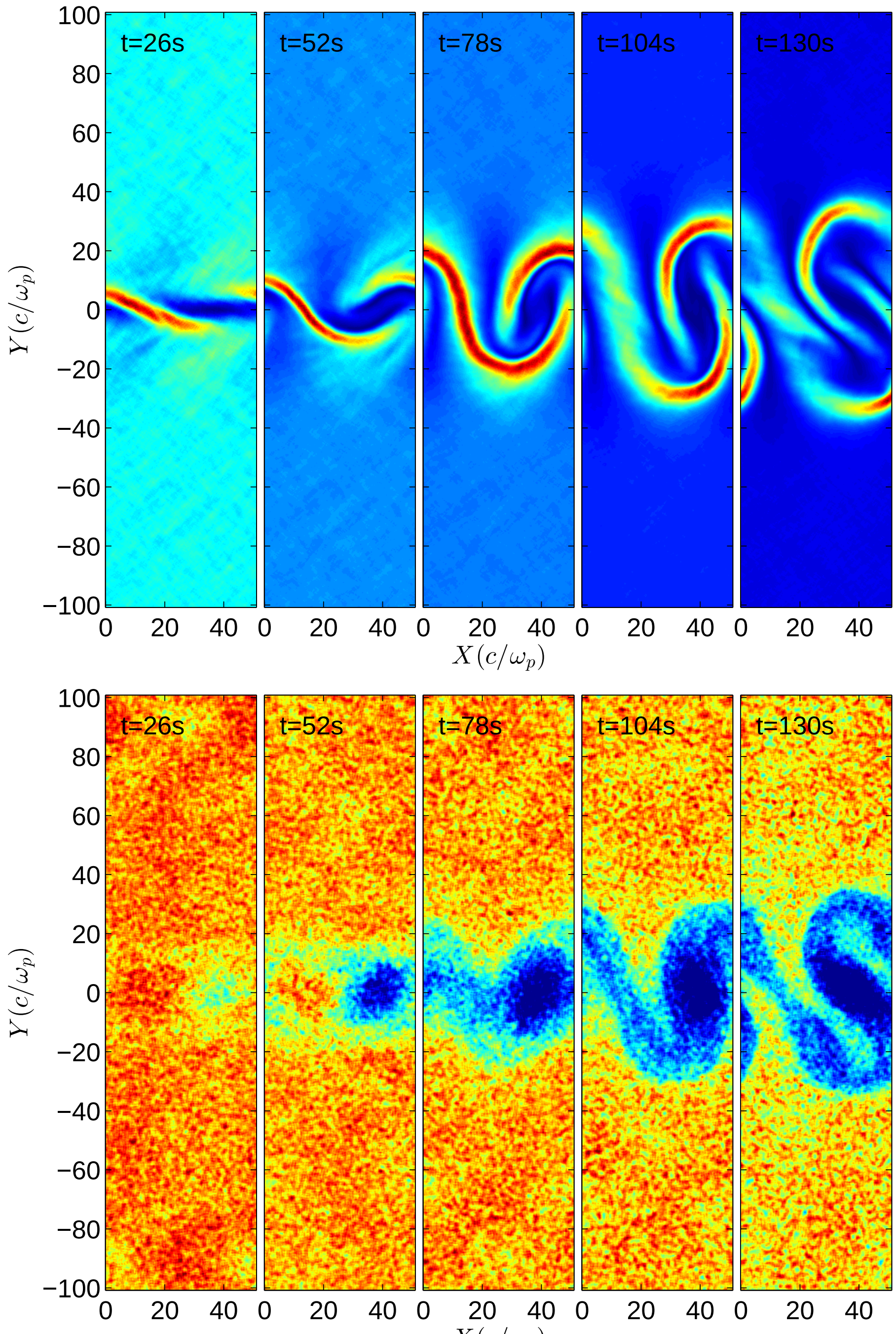

Figure 4.6: Top: Magnitude of the magnetic field perpendicular to the velocity shear $|\mathbf{B}_\perp|$ at different time steps. Bottom: A color coded perpendicular temperature $T_\perp$ in the range between 0.185 and 0.205 at different times. Horizontal axis is parallel with shear flow velocity. The values on both axes are expressed in hybrid units $c/\omega_p = v_A/\Omega_p$.

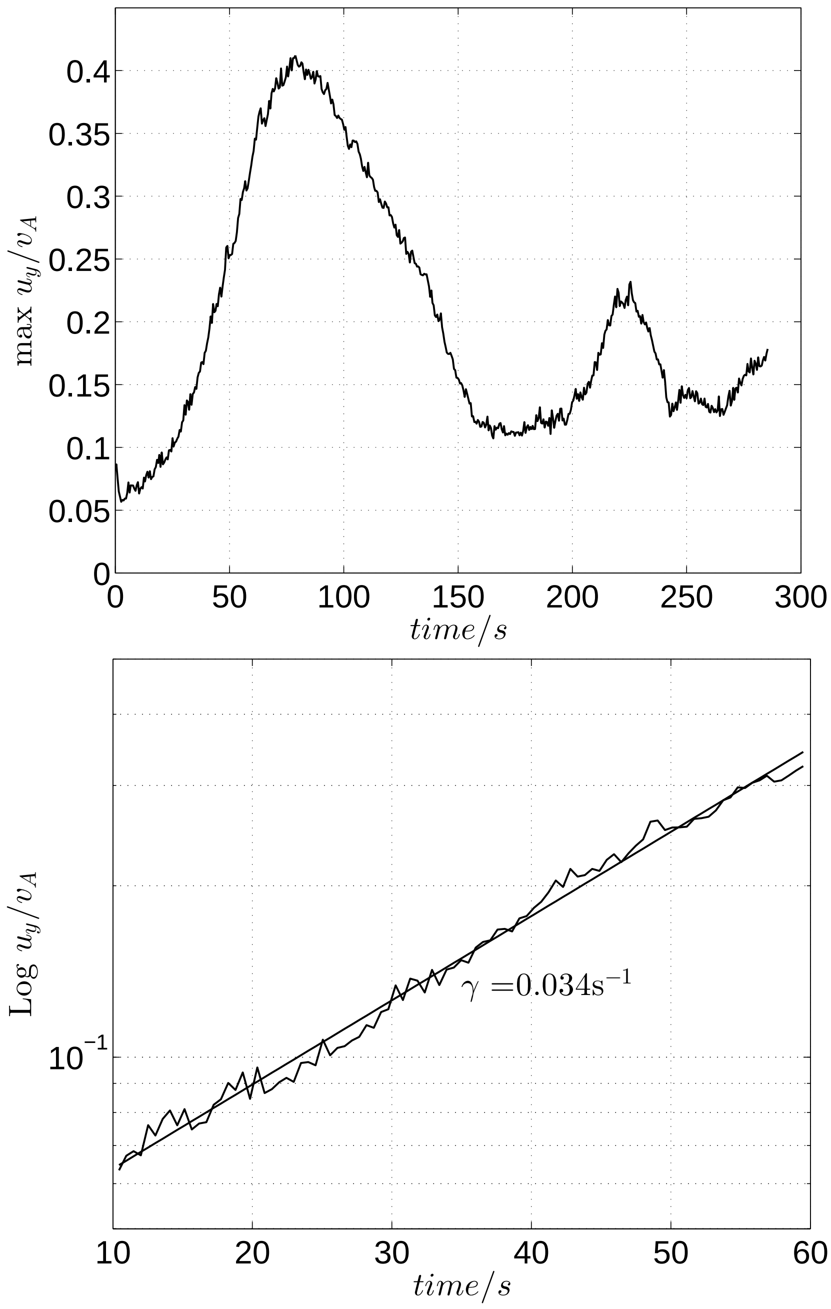

Figure 4.7: Growth of $\max(u_y)$ component of the bulk velocity over the simulation time at the top and expanded view in the bottom figure. Estimated exponential growth rate is 0.034 s^{-1} which is in perfect agreement with the value predicted by ***Rankin et al.*** [1993] using MHD model.

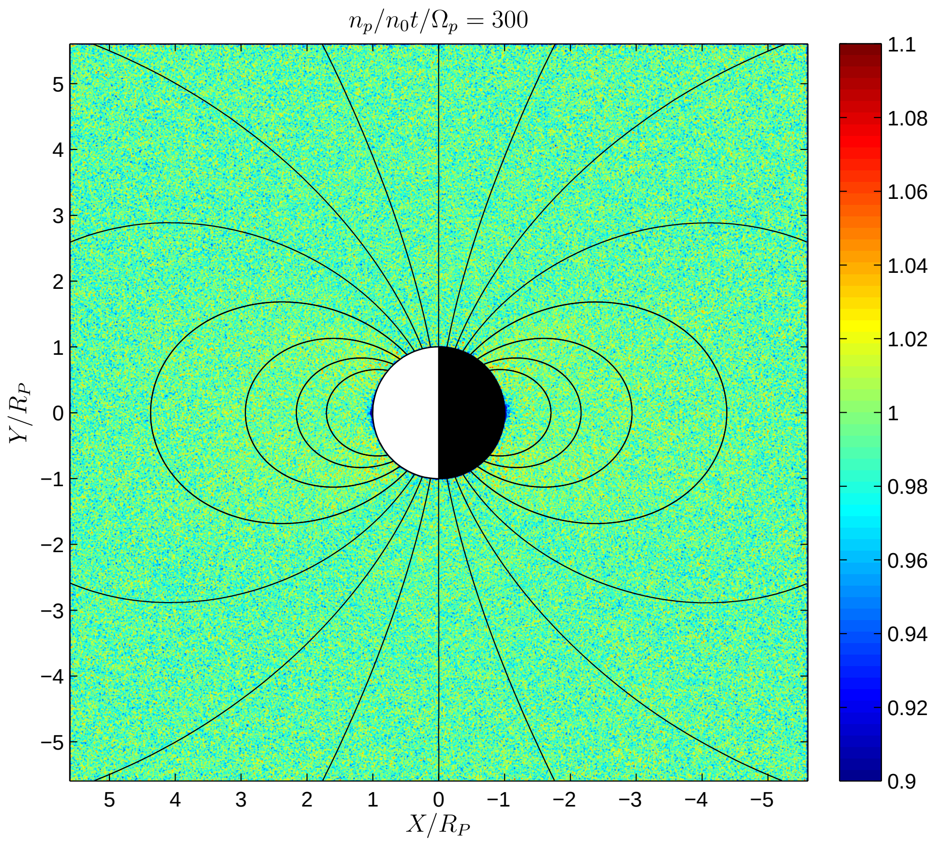

Figure 4.8: This figure represents proton density at late simulation time $t\Omega_{pi} = 300$ of following code set up: the open boundary conditions are applied at both directions; the magnetic field is initialized with the dipole placed inside of the conducting sphere; particles are specular reflected from the surface; and we impose free slip plasma conditions on bulk velocity.

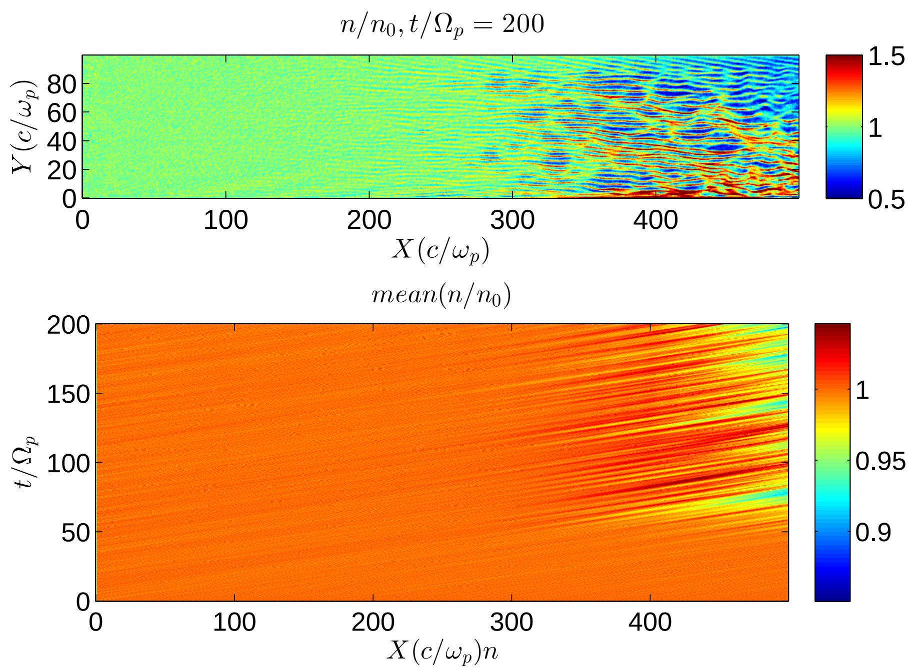

Figure 4.9: Number density in the X-Y plane at the simulation time $t/\Omega_p = 200$ (top panel) and evolution of the mean value of the number density over time (bottom panel).

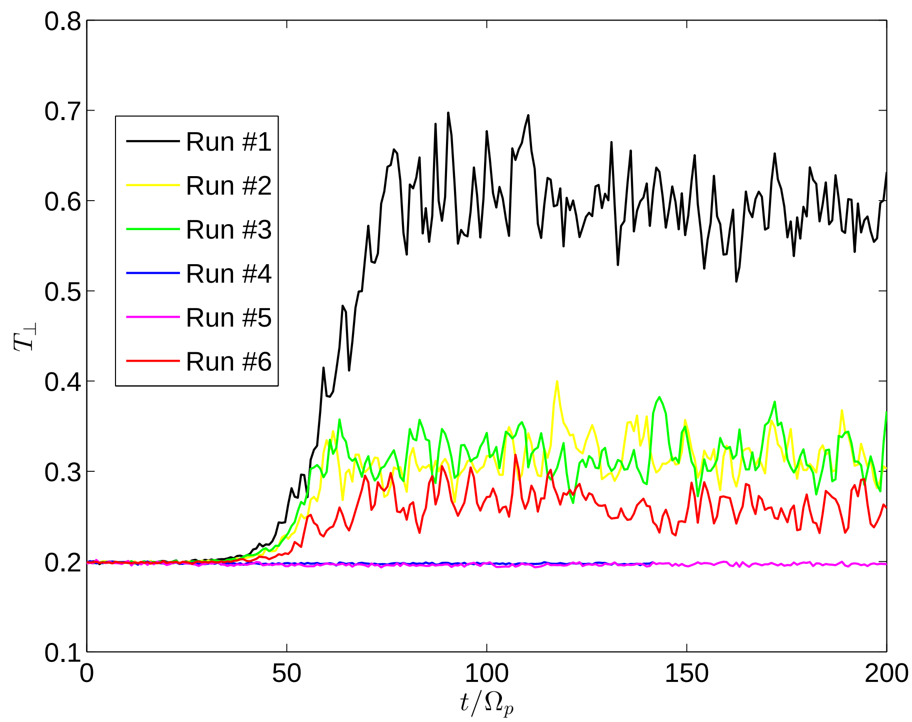

Figure 4.10: The numerical heating of freely streaming plasma. The curves represent $T_\perp$ as a function of time for the initial parameters from Table 4.5.

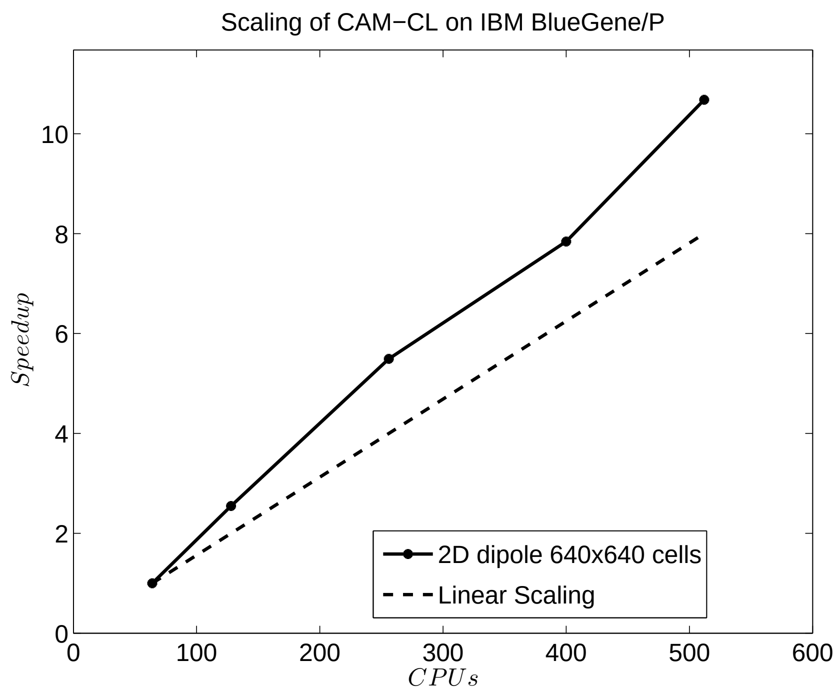

Figure 4.11: Scaling of the code with increasing number of processor is better than linear.

Bibliography

Cheng, C. Z., Magnetospheric Equilibrium with Anisotropic Pressure, *J. Geophys. Res.*, *97*, 1497–1510, 1992.

Cheng, C. Z., MHD field line resonances and global modes in three-dimensional magnetic fields, *J. Geophys. Res.*, *108*, 2003.

Gary, S. P., *Theory of Space Plasma Microinstabilities*, Cambridge Univ. Press, 1993.

Li, X., and S. R. Habbal, Hybrid simulation of ion cyclotron resonance in the solar wind: Evolution of velocity distribution functions, *J. Geophys. Res.*, *110*, A10,109, 2005.

Rankin, R., B. G. Harrold, J. C. Samson, and P. Frycz, The Nonlinear Evolution of Field Line Resonances in the Earths Magnetosphere, *J. Geophys. Res.*, *98*, 5839–5853, 1993.

Rankin, R., P. Frycz, J. C. Samson, and V. T. Tikhonchuk, Shear flow vortices in magnetospheric plasmas, *Phys. Plasmas*, *4*, 829, 1997.

Ueda, H., Y. Omura, H. Matsumoto, and T. Okuzawa, A study of the numerical heating in electrostatic particle simulations, *Comput. Phys. Comm.*, *79*, 249–259, 1994.

Chapter 5

Planet Mercury

In this section we summarize the observations of the planet Mercury provided by NASA's MESSENGER spacecraft using the Fast Imaging Plasma Spectrometer (FIPS) *Zurbuchen et al.* [1998] and the Magnetometer (MAG) *Andrews et al.* [2007] instruments. The in situ measurements are crucial for study of the exosphere and the magnetosphere interactions with the solar wind. Information from the MAG instrument provides us with information about magnetosphere structure while the FIPS instrument gives us insight into the energy distribution of particles. Note that FIPS data interpretation is difficult due to the obstructed field of view (FOV) of the instrument by the Sun-shield. Only the transverse particle distribution, in respect to Sun-Mercury line, have direct access to the instrument. The flyby results from the FIPS instrument are summarized in *Zurbuchen et al.* [2008]. The particle data are also used to determine the magnetopause crossings *Sundberg et al.* [2012].

5.1 Introduction

Although extended amount of research exists on a subject of coupling between the magnetosphere of Earth and the solar wind, Mercury introduce some unique aspects. Unlike the magnetosphere of Earth which is rooted in the ionosphere, Mercury's magnetosphere is firmly rooted in the regolith. The atmosphere which is an important source of ions and a major sink of energy from the solar wind is nonexistent at Mercury. Instead, the exosphere which is filled with neutrals and ions from the regolith by sputtering substitutes the Earth-like atmosphere.

Sufficient amount of data from the MESSENGER spacecraft suggests that the

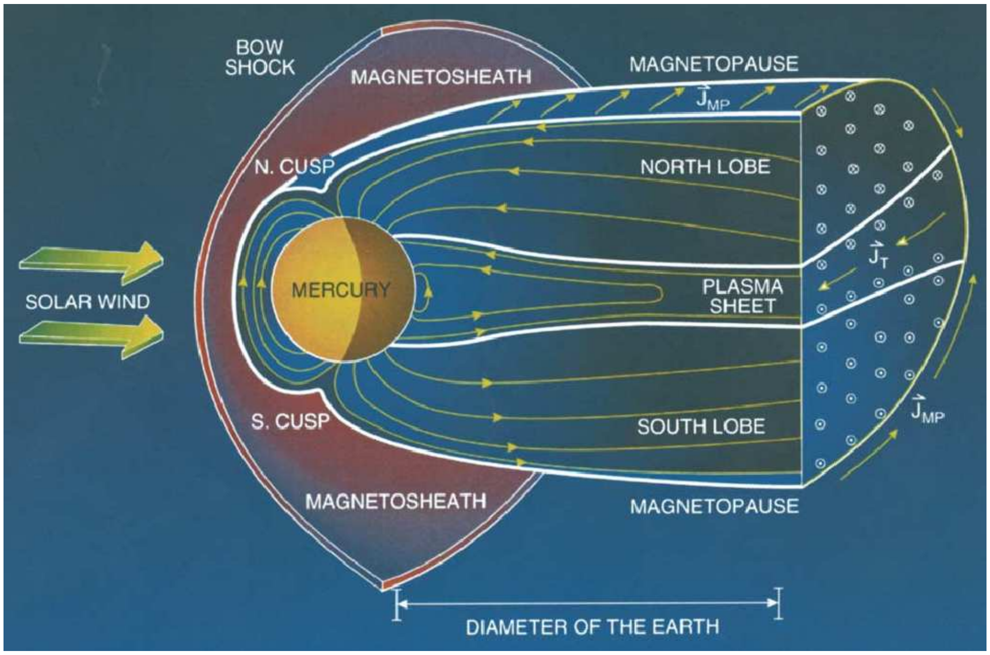

Figure 5.1: A schematic depiction of a magnetosphere structure deduced from the linearly scaled down magnetosphere of Earth. Adopted from *Slavin* [2004].

strength of the magnetic dipole is sufficient to stand off the solar wind most of the time. The magnetopause stand off distance was estimated to be 0.5 R_M from the planet's surface simply by linearly scaling the Earth's magnetosphere [*Ogilvie et al.*, 1977]. Figure 5.1 summarize the structure of the Mercury-Sun interaction system. Because of small size of the planet, the formation of a plasmasphere or the trapped radiation belts is impossible. But from the observations we may recognize the three distinct regions of the plasma: (1) The magnetosphere, the most inner region of closed field lines, is compressed to within 0.5 R_M at the dayside of the planet due to the high ram pressure of the fast solar wind. (2) The nightside magnetosphere consists of the north and south lobes of extruded field lines into the far tail region. (3) The plasmasheet is sandwiched between the lobes and it is composed of less dense but high temperature (1-2 keV) plasma. The discontinuity layer of the space which wraps around the magnetosphere is the magnetopause. When the solar wind reaches the planet and starts to interact with the intrinsic magnetic field it slows down from super to sub-sonic speeds and forms a shock wave called the bowshock due to its shape. The region of space between the bowshock and the magnetopause is the magnetosheath and it consists of fast flowing and high density but low temperature plasma.

5.2 Solar wind conditions at Mercury

Numerical models are necessary to predict space weather at Mercury because the MESSENGER's instruments cannot provide us with all solar wind parameters. The harsh environment at an orbital distance of Mercury requires the spacecraft to be hidden behind the sun-shield at all times. The knowledge about the solar wind parameters upstream of the planet is important for initialization of our global numerical code.

Baker et al. [2009] used the Wang-Sheeley-Agre (WSA) model to estimate solar wind conditions of the first flyby on January 14, 2008. The WSA model [*Agre et al.*, 2004] is the improved Wang-Sheeley [*Wang and Sheeley, N. R.*, 1992] model which is combination of empirical and physical model of the inner heliosphere. The model combines ground-based observations of the magnetic field at the surface of the Sun with an ideal MHD numerical code which calculates solar wind propagation. *Baker et al.* [2009] carried out the simulation from 0.1 AU to 1.1 AU and validated the results against the spacecrafts STEREO-A/B and ACE. They concluded a good temporal and spatial agreement of the observations with the model. Figure 5.2 represents an example of the solar wind parameters predicted for time period of two months. A grey region represents time when MESSENGER was directly interacting with the environment of Mercury. Although solar wind peaked at 600 km/s during the flyby the speed remained stable at 400 km/s most of the times.

In a subsequent paper, *Baker et al.* [2011] covered the second and the third flybys using the same WSA model to predict the solar wind parameters upstream of Mercury. We summarized all the parameters from the references above in Table 5.2.

Event	$\lvert B\rvert$ [nT]	n_p [cm^{-3}]	v_r [km/s]	Mach	P_{dyn} [nPa]	T [eV]
1st Flyby	18	60	420	7.5	20	10.34
2nd Flyby	15	60	380	9	15	17.24
3rd Flyby	20	50	390	5	10	8.62

Table 5.1: The upstream solar wind parameters for the planet Mercury from the global solar system model by *Baker et al.* [2009, 2011]

5.3 Exosphere

The size of the magnetospheric cavity of Mercury does not allow the formation of the atmosphere or the ionosphere similar to Earth but instead the planet possess the

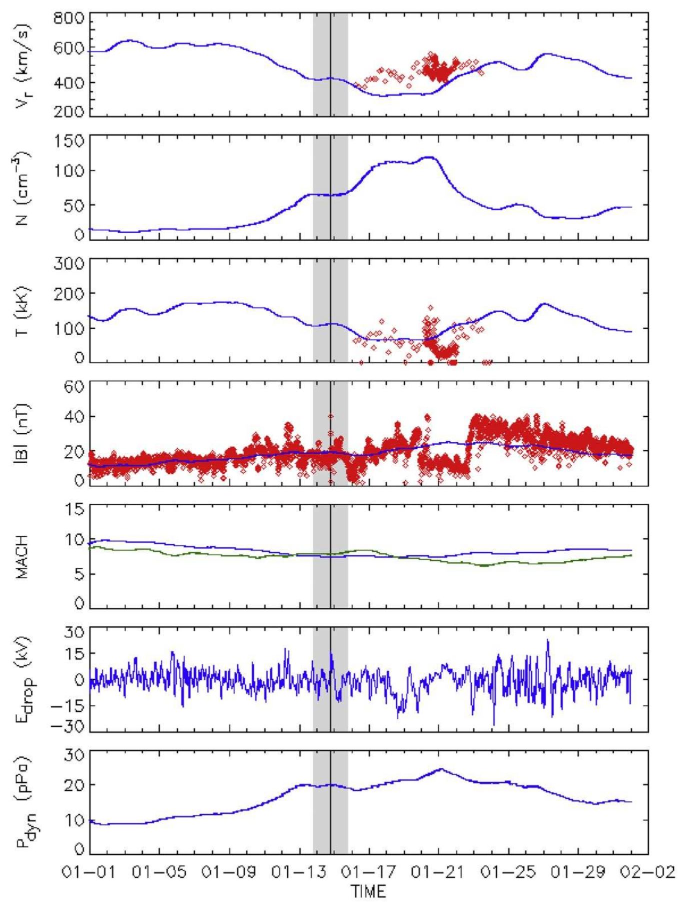

Figure 5.2: The solar wind parameters during the first flyby of MESSENGER as predicted by the WSA model. The red stars represent the direct measurements of the MESSENGER spacecraft. From *Baker et al.* [2009].

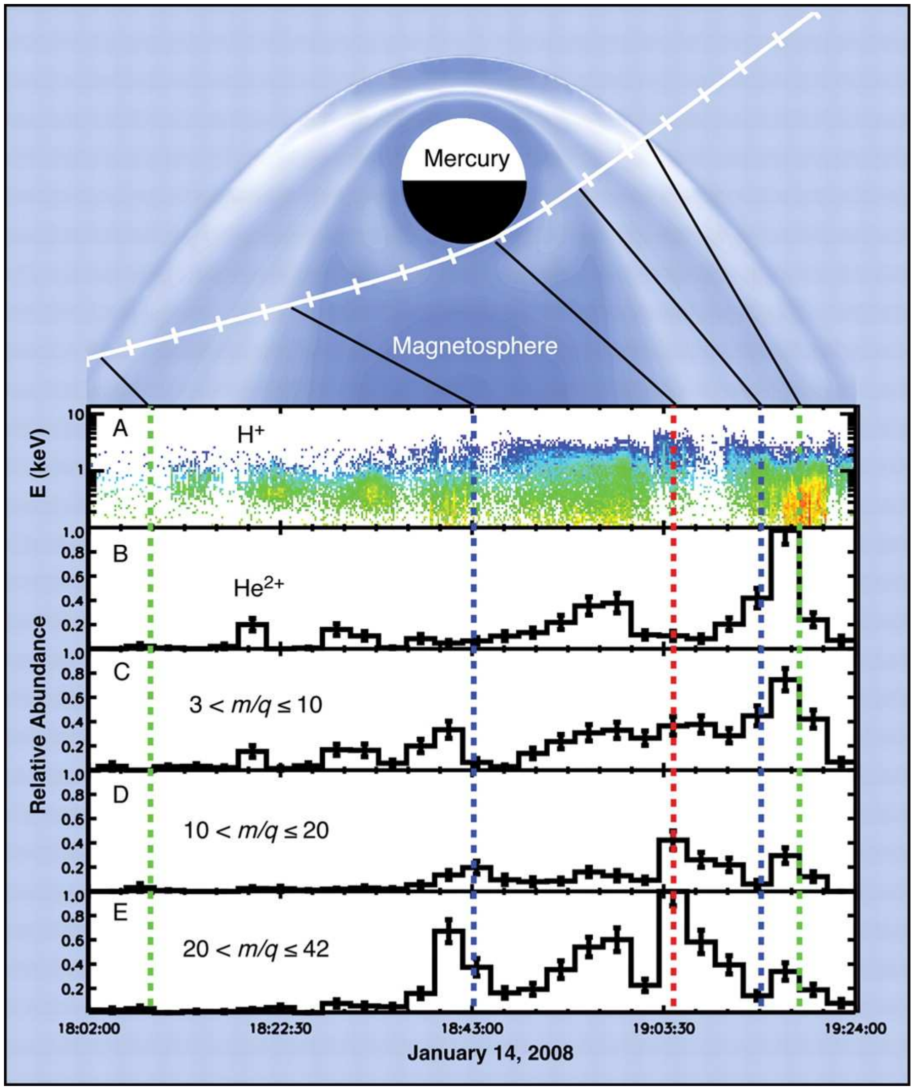

Figure 5.3: The data measurements by the FIPS instrument during the first flyby of MESSENGER on the background of proton density predicted by the MHD model. The different plates represent different range of m/q ratios. Adopted from *Zurbuchen et al.* [2008].

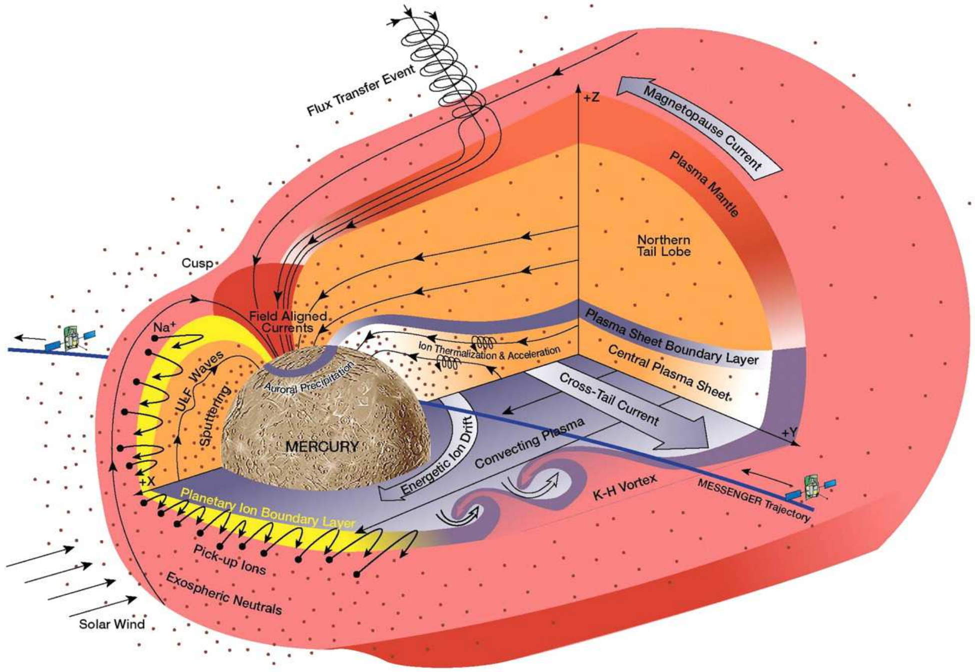

Figure 5.4: A cartoon representing global structure of the magnetosphere of Mercury as interpreted after the first flyby of MESSENGER. Adopted from *Slavin et al.* [2008].

exosphere which is a mixture of solar wind plasma and plasma of planetary origin. *Zurbuchen et al.* [2008] describes the data acquired during the first flyby from the particle instrument (FIPS). The results yielded Na^+, O^+ and K^+ abundances which were consistent with the remote observations of the neutral species. The spacecraft recorded the fluxes of the heavy ion species like sodium and oxygen, concentrated near the surface of the planet . Figure 5.3 shows a spatial distribution of ion species separated into the different ranges of m/q ratios. In the Chapter 7 we will present the numerical results from the particle tracing code developed for the purpose of studying exosphere of the planet Mercury. The data in the bottom panel, which include sodium ions Na^+ measurements, are in a perfect agreement with our numerical model.

5.4 Magnetosphere

The work of *Anderson et al.* [2011] answered the long standing question of strength and topology of the intrinsic magnetic field of Mercury. They concluded that the magnetic field of the planet can be described by a dipole with offset of 484$\pm$11 km north of the geographic equator and with the amplitude of 195±10 nT R_M^3. Because Mariner 10 measured a similar value more than 30 years ago, *Anderson et al.* [2011] concluded that the strength did not change from time of the first observations.

Slavin et al. [2010] were interested in a dynamic structure of the magnetosphere and they reported the observations of 6 flux transfer events (FTE). FTE is an event of the magnetic field lines being transported from the dayside of the planet to the tail. This restructuring of the magnetosphere is caused by magnetic reconnection. Such physical process may occur after a change in orientation of the interplanetary magnetic field from north to south direction (anti-parallel with the magnetic field of the planet). Time duration of FTEs is on the order of seconds and diameter of the observed flux tubes is $\approx$ R_M. Note that FTEs were already reported from the observations of Mariner 10 in the work of *Russell and Walker* [1985].

Raines et al. [2011] summarized the basic plasma parameters from the first two flybys of Mercury. During the first flyby on January 14, 2008 IMF was in north direction. The following plasma parameters were derived from the FIPS instrument: The plasmasheet was quiet with the proton density ranging n_P = 1-10 cm^{-3}. The proton temperature $T_P \approx 2 \times 10^6$ K and the plasma beta was $\beta \approx 2$. The night side boundary layer was characterized by the following parameters: n_P = 4-5 cm^{-3}, $T_P \approx 4 - 8 \times 10^6$ K and $\beta \approx 2$. The second flyby on 6 October 2008 with south IMF had a very similar trajectory with the fist flyby. *Raines et al.* [2011] estimated the following plasmasheet parameters from the FIPS instrument: n_P = 4-5 cm^{-3}, $T_P \approx 8 \times 10^6$ K which was attributed to reconnection which took place in the tail region and $\beta \approx 20$. The night side boundary layer had very similar plasma density n_P = 4-5 cm^{-3} but the temperature was 50% higher at $T_P \approx 8 \times 10^6$ K and $\beta \approx 20$ again attributed to the reconnection.

5.5 Kelvin-Helmholtz Observations

Boardsen et al. [2010] reported the results of a data survey of 15 magnetopause crossings which occurred during the inbound of the third MESSENGER's flyby on September 29, 2009. This was a first observational evidence of the Kelvin-Helmholtz waves at Mercury. They investigated two minutes (roughly 0.2 R_M) of data and showed a typical saw-tooth like pattern in the magnetic field which was result of steepening at the leading edge of the surface waves excited by the KHI. A close analysis revealed $\approx$ 16s period between the pairs of the crossings. They concluded, from the thickness of the boundary, that kinetic effects are important in the study of the Kelvin-Helmholtz in-

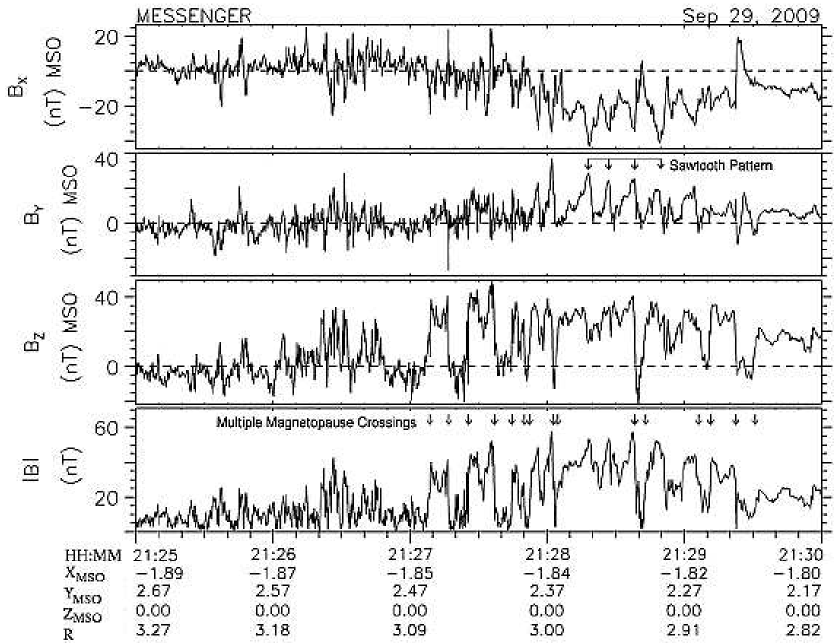

Figure 5.5: The magnetic field measurements from the third flyby of MESSENGER. The spacecraft recorded 16 magnetopause crossings at the dawn flank. Adopted from *Boardsen et al.* [2010].

stability at Mercury. Although the magnetic field was southward before the spacecraft entered the magnetosheath it underwent a change from south to north while the spacecraft was in the magnetosheath which is an orientation favouring the KHI. Figure 5.5 shows time series of the magnetic field for the analyzed event with arrows indicating 16 magnetopause crossings.

Sundberg et al. [2012] surveyed first year of MESSENGER's orbital data in search for the signatures of the KH waves. Interestingly, they found the KH waves to be frequently present in the post-noon sector which they interpreted as a result of higher growth rates present at Mercury compared to Earth. The interplanetary magnetic field was predominantly northward for the reported events and the waves were characterized by amplitude on the order of 100 nT and the wave periodicity of $\approx$ 10 - 20 s. During the events, they reported increased plasma transport from the magnetosheath to the magnetosphere. Figure 5.6 is one the examples of the investigated events which shows a clear signature of the Kelvin-Helmholtz wave in the y-component of the magnetic field accompanied by an increased proton flux as the spacecraft crossed the magnetopause. In Chapter 6 we will investigate an asymmetry of the KH wave observations

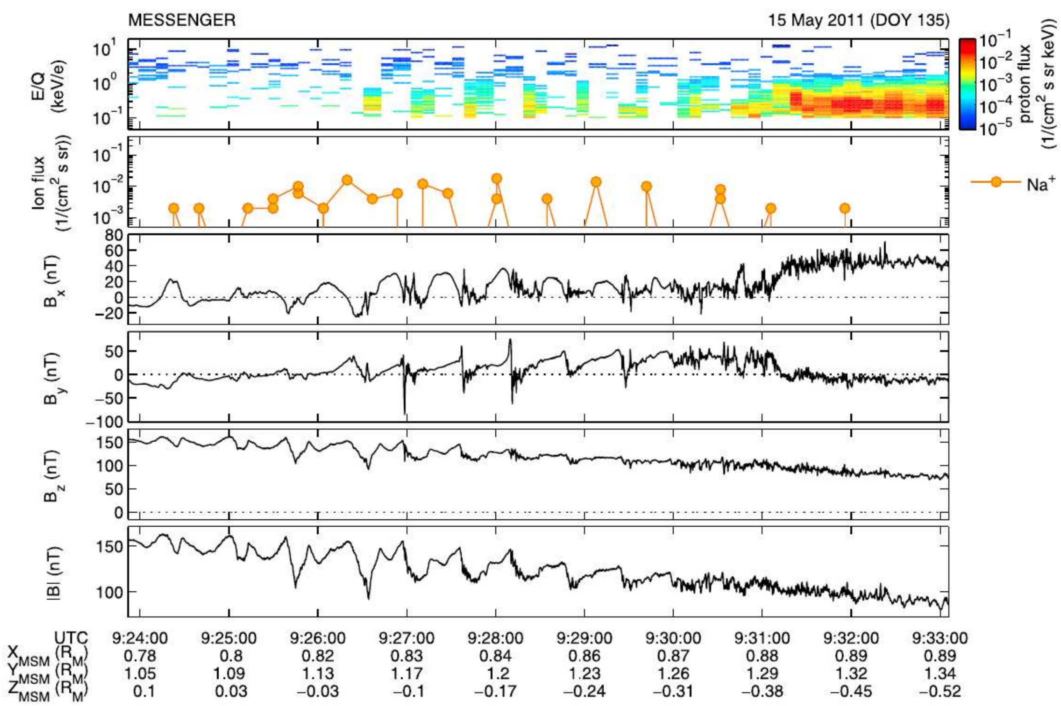

Figure 5.6: One of the events which shows a typical signature of the Kelvin-Helmholtz wave in B_y component of the magnetic field. Adopted from ***Sundberg et al.*** [2012].

in detail using the global numerical model.

5.6 Modelling

In Chapter 3 we introduced a numerical schema used to solve the set of equations on a uniform rectangular grid. Every physical problem of our interest requires unique boundary and initial conditions. User of the code can achieve this functionality by sub-classing the main class which holds the implementation of the code and overwrite the functions which are relevant to the given problem. The rest of the common parameters which may change between the runs can be altered through the input file. Such parameters include the orientation of magnetic field, number of the spatial cells, number of the particles per cell, the resolution, etc. User can also specify a type of the boundary conditions (periodic or open).

The initial and boundary conditions are unique for each physical problem. The initial conditions allow a user to specify the following variables: the magnetic field, the bulk velocity, the parallel and perpendicular temperature of the bi-Maxwellian particle distribution in the velocity space. The boundary conditions are executed during every computational step and they can be applied to the following variables: the magnetic field, the electric field, the resistivity, particle's position and velocity, the moments of the distribution function (density and bulk velocity).

5.6.1 Initial Conditions

The code requires to specify spatial distribution of the plasma and the magnetic field at time $t = 0$. The initial state of the system is then evolved by allowing the plasma to interact with the boundary conditions described in the next section.

The magnetic field is initially set to be a superposition of the interplanetary magnetic field (IMF) and the dipole field of the planet $\mathbf{B} = \mathbf{B}_{\mathrm{IMF}} + \mathbf{B}_{\mathrm{dip}}$. The IMF represents the magnetic field embedded in the solar wind and its magnitude is always 1 because all values of the magnetic field are scaled to its value $|\mathbf{B}_{\mathrm{IMF}}| = 1$. The orientation is given by an angle ϕ between projection of the field onto the x-y plane and the x-axis; and an angle θ between the field direction and the z-axis. We will always use purely north IMF because to change the direction of the IMF would shift the system to a reconnection scenario, which would violate 2D assumption. The magnetic field of the planet is given by

$$\mathbf{B}_{dip}(\mathbf{r}) = \frac{\mu_0 M}{4\pi r^3}(3\,\hat{\mathbf{r}}(\hat{\mathbf{m}}\cdot\hat{\mathbf{r}}) - \hat{\mathbf{m}}), \tag{5.1}$$

where M is a constant determined from the magnetic field at the surface of the planet and $\hat{\mathbf{m}}$ is a unit vector in a direction of the dipole.

The proton density (the only ion species used in the global model) is initially distributed uniformly throughout the simulation box. This allows the plasma to adjust naturally to the boundary conditions as the simulation time evolves. When the simulation progress, a region behind the planet becomes depleted of the plasma because it is shielded from the direct access of the solar wind.

The code allows to load the plasma with a bi-Maxwellian distribution function defined by the parallel plasma beta $\beta_\parallel$; the temperature anisotropy $A = T_\perp/T_\parallel$; and the bulk velocity $\mathbf{v}_0$ which shifts the distribution function in the velocity space. The both parameters can be defined in a configuration file or in a specialized function supplied by a user. The latter method is useful in the case when we require the parameters to vary spatially. In the global simulation of Mercury, we initialized the domain uniformly with the isotropic plasma of the temperature estimated from the third flyby of MESSENGER (8.62 eV). To jump start the simulation we may initialize the solar wind bulk velocity to be $v_{sw} = v_{0x}$ everywhere except of the inside of the magnetosphere described by a function from *Shue et al.* [1997]

$$r = r_0 \left(\frac{2}{1+\cos(\theta)}\right)^{\alpha}, \tag{5.2}$$

where r_0 represents the distance of the boundary in the Mercury-Sun direction and θ is an angle between the Mercury-Sun line and a local position. Although we performed several tests using the above setup, the benefits did not out weight the problems introduced by the artificial velocity gradients and we returned back to the uniform velocity distribution of the solar wind (390 km/s).

5.6.2 Boundary Conditions

We applied the boundary conditions at the end of each simulation step and after the calculation of each particle position. For the global model of Mercury we must specify additionally the boundary conditions at the surface of the planet. The plasma parameters at the edges of the simulation box correspond to the solar wind parameters because

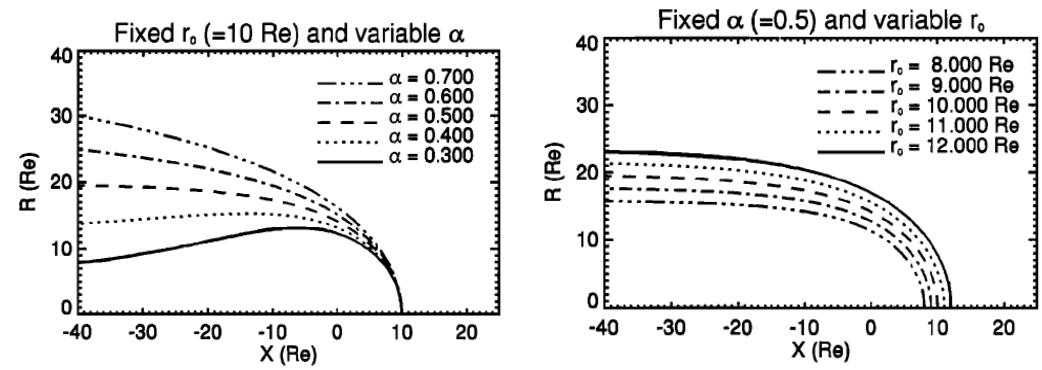

Figure 5.7: A representation of the magnetosphere boundary for constant $r_0 = 10$ (upper panel) and constant $\alpha = 0.5$ (bottom panel). Taken from *Shue et al.* [1997].

we used the open boundary conditions.

We turned on a field masking technique which is described in Chapter 3 at the planet's surface and at all four sides of the simulation box. We set a characteristic thickness of the layer to be $L_D = 3\ kc/\omega_p$. An artificial resistivity remains constant within the box, although other competing works of global modelling applied the increasing resistivity layer successfully. An electric field diffusion term is turned off completely. We imposed a special treatment of the bulk velocity at the planet's surface to mimic the free slip conditions. We artificially reduce the normal component of the bulk velocity in a vicinity of the planet so that at the surface the normal component of the bulk velocity is zero. If any particle hit the planet's surface, it is specular reflected back. The planet does not represent the source of a new plasma and it is treated as a perfect conductor. The electric field is set to zero and the magnetic field is forced to remain constant $\partial B/\partial t = 0$ inside of the planet. The boundaries of the simulation box are open for all particles to leave freely. New particles are injected every simulation time step with the distribution function of the solar wind.

Because we are limited by available computer resources, we are often forced to reduce the size of the simulation box. This can be achieved by reducing the size of the planet. We adopted an approach from *Trávníček et al.* [2009] who reduced the physical size of the planet and the strength of the magnetic dipole while preserving the magnetopause stand off distance in the units of planetary radii between the scaled and the full size of the planet. In consequence, we must be careful when interpreting the numerical results. First, the gyroradius becomes larger in respect to the size of the magnetosphere. Second, the timing of physical processes may change compared to the full scale of the planet. We show the results from the two simulations to demonstrate this fact by comparing the full scale and three times smaller size of the planet.

5.6.3 Results

	Scaled Size	Full Size
# cells	2240×2432	5004×5040
$\triangle x\ \omega_p/c$	0.3×0.3	0.3×0.3
$L\ \omega_p/c$	672×729.6	1501×1512
$R_{M,real}/R_{M,sim}$	3	1
$R_M\ \omega_p/c$	25.04	75.13
$\mu_0 M/4\pi$	153,126	4,134,390
$\triangle t\ \Omega_p$	0.008	
β_e	0.5	
$\beta_{\parallel p}$	0.3	
$T_\perp/T_\parallel$	1.0	
v_{0x}/v_A	6.27	
# pcles/cell	120	

Table 5.2: Initial parameters of global 2D simulations of planet Mercury.

In this section we present the results from two very similar numerical runs of the global model of Mercury with the input parameters appropriate to the third flyby of MESSENGER. The only parameter which differs between the runs is the radius of the planet and comparably scaled strength of the magnetic dipole. The first run represents three times scaled down size of the planet compared to the full size planet of the second run. The summary of the input parameters is given in Table 5.6.3.

All figures show an equatorial plane of Mercury with the x-axis pointing in the Mercury-Sun direction, the z-axis points in the northward direction and the y-axis complements the right hand coordinate system. When two panels are presented in a single figure, top and bottom panels represent scaled down and full size simulation runs, respectively. Because our calculations are two dimensional, we neglected the shift of the magnetic moment by 484 km in the north direction reported by *Anderson et al.* [2011]. The approximation have no effect on a scientific interpretation of the numerical results.

Figure 5.8 represents a color coded proton density in the units of cm^{-3}. A green solid line is a track of the third flyby of MESSENGER. The trajectory gives us a unique opportunity to study the Kelvin-Helmholtz instability at the dusk flank. The

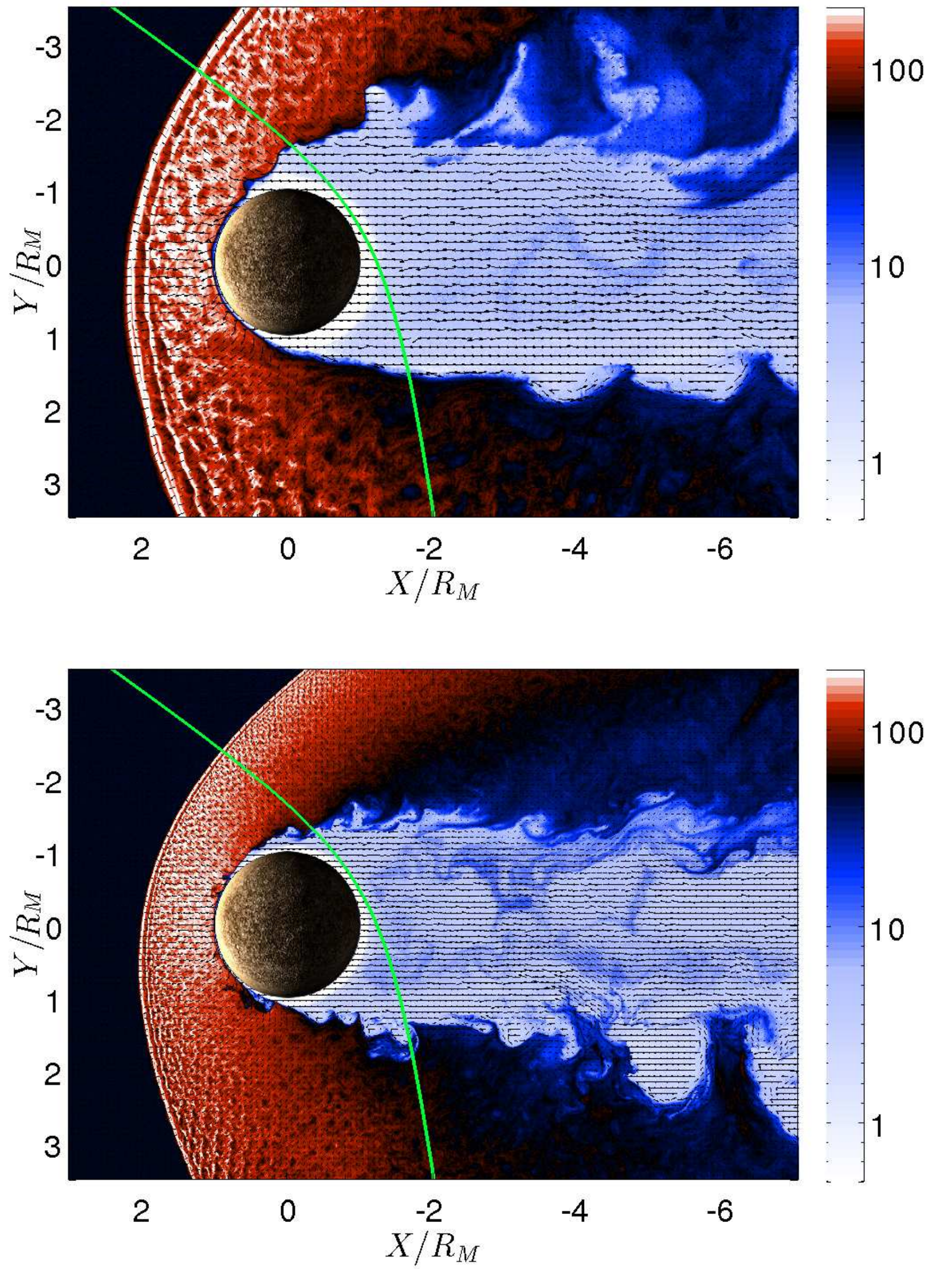

Figure 5.8: Scaled down (top) and full size (bottom) simulation runs respectively. Figures represent a color coded proton density n_p/cm^{-3} in the equatorial plane with the green line representing trajectory of the third flyby of MESSENGER. The arrows represent the bulk velocity in the frame reference of the solar wind.

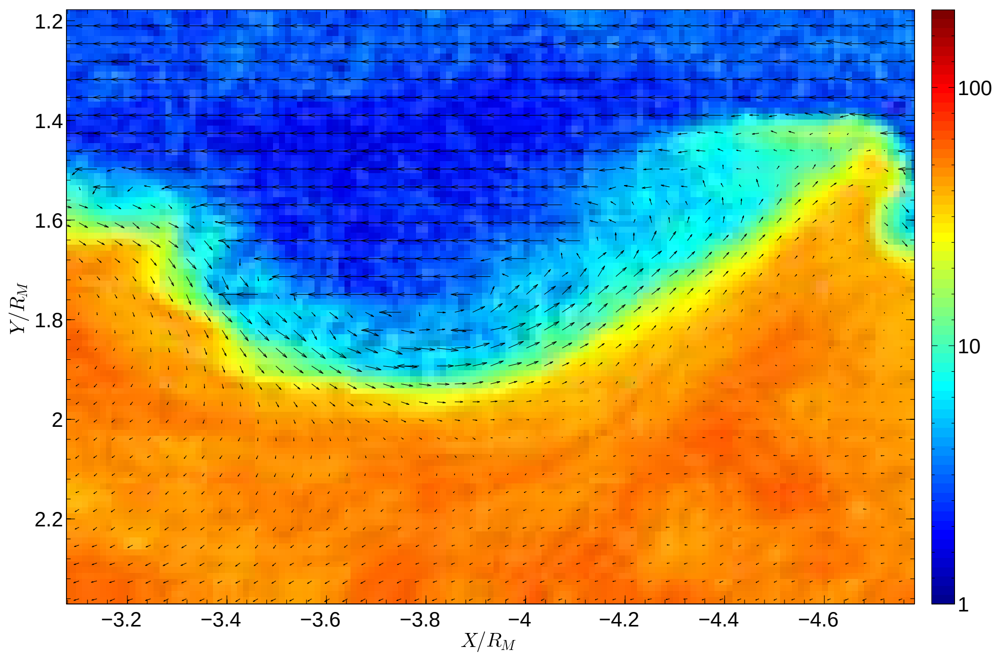

Figure 5.9: The color represents the proton density n_p/cm^{-3} of enlarged vortex with over-plotted bulk velocity, in the frame of reference of the solar wind, represented by the black arrows.

black arrows overlaid on top of the figure show the bulk velocity of the protons shifted into the frame of reference of the solar wind. Because of larger distances in the full scale simulation, the Kelvin-Helmholtz instability may destabilize the boundary for the longer times thus forming the larger vertices which appear relatively closer to the planet. Figure 5.9 shows a detail of the vortex overlaid with the arrows of the bulk velocity. The flow inside of the vortex wraps around and mix the plasma. The motion of the plasma inside of the vortex carry the frozen-in field lines with it and generates the shear Alfwén waves which propagate parallel to the field, towards the poles.

Figure 5.10 is analysis of a Kelvin-Helmholtz instability criteria. A simple approximation to the growth rate of the KHI for a step-like change in the plasma flow velocity can be obtained from an ideal MHD in the incompressible gas limit *Hasegawa* [1975]. This yields a threshold condition for the KHI that is defined by

$$(\mathbf{k} \cdot \mathbf{v}_0)^2 - \frac{n_1 + n_2}{n_1 n_2} \left[n_1 (\mathbf{k} \cdot \mathbf{v}_{A1})^2 + n_2 (\mathbf{k} \cdot \mathbf{v}_{A2})^2 \right] > 0. \tag{5.3}$$

In this expression, subscripts 1 and 2 denote quantities on either side of the velocity shear, which is regarded as a boundary of zero thickness. The quantities n and $\mathbf{v}_A$ denote number density and Alfven velocity respectively; $\mathbf{k}$ and $\mathbf{v}_0$ correspond to the KHI wave vector and plasma streaming velocity, respectively. Assuming $\mathbf{k}$ parallel to $\mathbf{v}_0$. We studied a clear dawn-dusk asymmetry of the Figure 5.10 in a separate manuscript presented in Chapter 6. We concluded that the asymmetry is caused by force imbalance at the magnetopause boundary which leads to the formation of the magnetic holes which resemble a Rayleigh-Taylor instability. This instability together with the broadening of the shear layer prevents a formation the laminar flows at the dawn which are necessary of the KHI.

Figure 5.11 is a color coded magnitude of the magnetic field $|\mathbf{B}|$ in the units of nT. A green contour at the magnetopause boundary outlines the unstable region of the Kelvin-Helmholtz waves detailed in the Figure 5.10. The unstable regions mark the area of high shear flow where the steady magnetospheric plasma and the fast flowing magnetosheath plasma interact with each other.

The thermal gyro-radius in respect to the spatial scales determine the regime in which the plasma operates. If the thermal gyroradius is comparable with the typical spatial scale than kinetic treatment is necessary. Figure 5.12 represents the color coded thermal gyro-radius in the units of c/ω_{pi}. The same spatial units were used on the x and y-axis to compare easily the spatial scale of the KH vortexes and the radius of

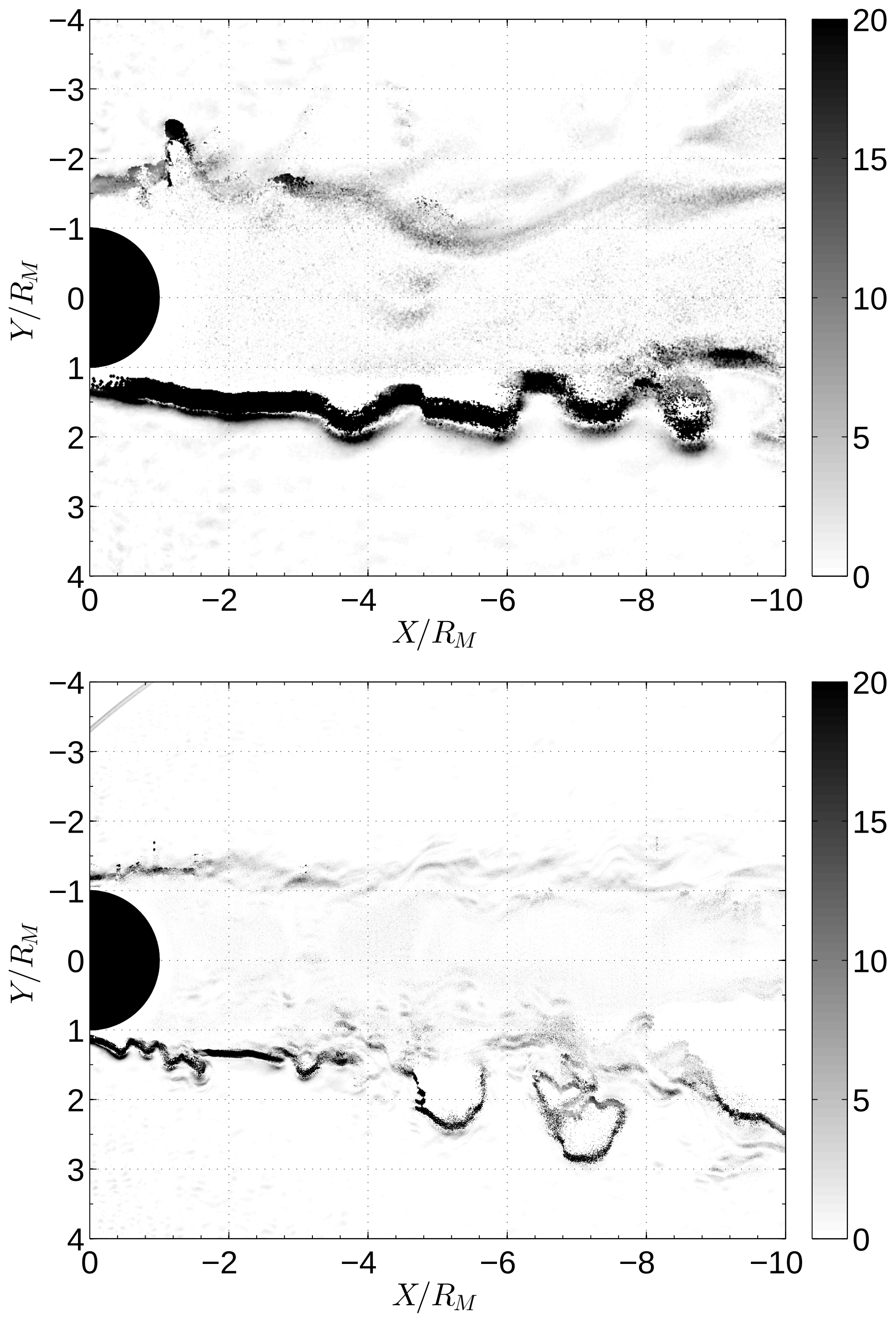

Figure 5.10: Scaled down (top) and full size (bottom) simulation runs respectively. The shade of black color represents the Kelvin-Helmholtz instability criteria of incompressible fluid evaluated in the equatorial plane.

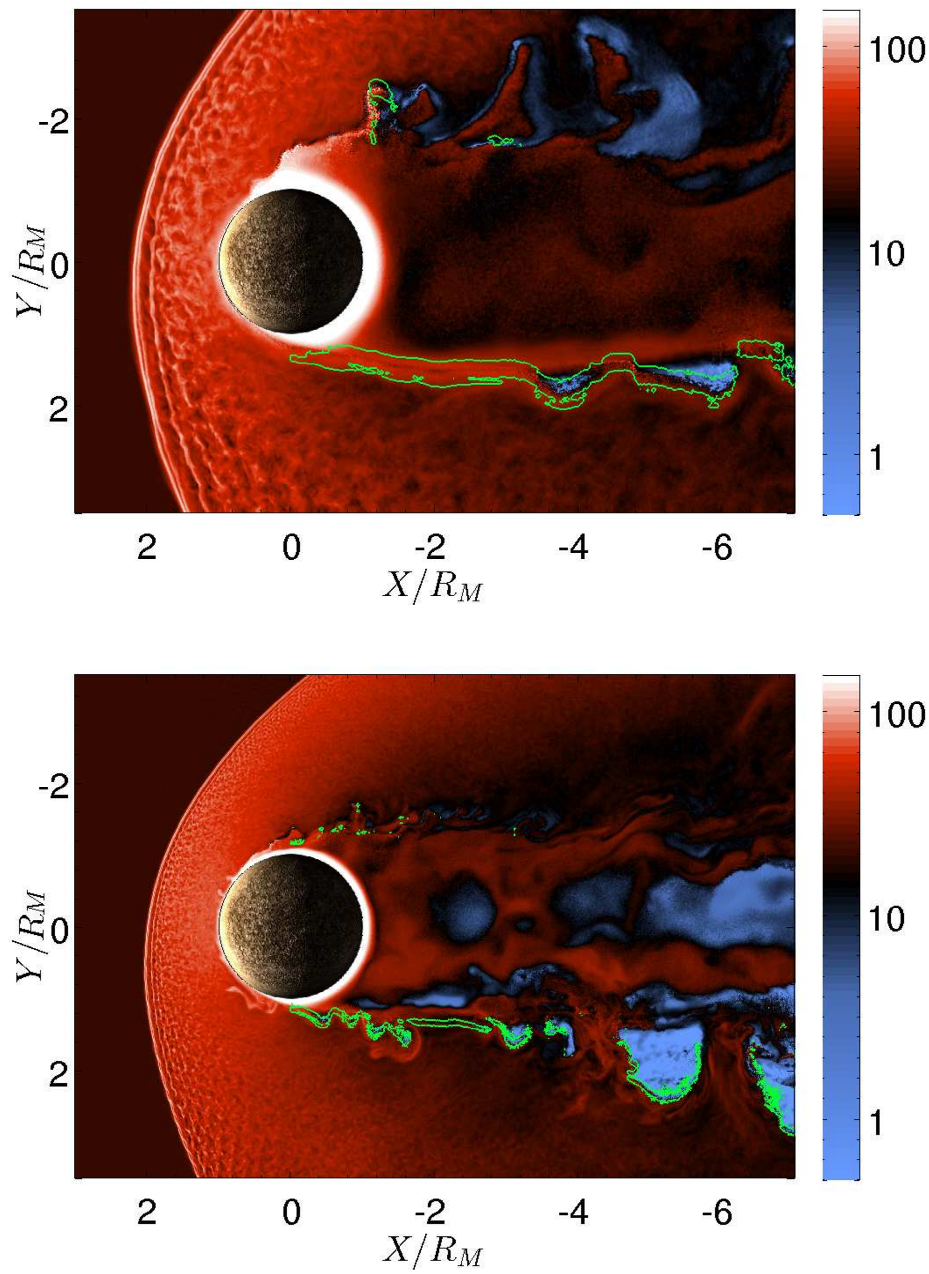

Figure 5.11: Scaled down (top) and full size (bottom) simulation runs respectively. Color coded magnitude of the magnetic field in the equatorial plane in the units of nT. The green lines highlight the regions which are unstable to the Kelvin-Helmholtz instability.

the thermal protons. The upstream gyro-radius is always equal to one because of the chosen scaling of the physical units. The upstream and the magnetosheet values of the gyro-radius are negligible but the magnetosphere, due to the much higher kinetic energy, has the gyro-radius which is comparable to the spatial size of the KH vortexes. The perpendicular temperature $T_\perp$ which is responsible for the high gyro-radius in the magnetosphere is visualized in Figure 5.13. Note that the absolute values of $T_\perp$ are similar between the scaled down (top panel) and the full size simulation (bottom panel). The black arrows represent a projection of the proton bulk flow onto the x-y plane.

Top panel of Figure 5.14 shows a magnitude of the magnetic field of the full scale simulation run at the time $t\Omega_P = 240$. Overlaid are the trajectories of 7 test particles traced from the upstream of the planet with the initial velocity of 390 km/s (the solar wind speed). A small size of the magnetosphere does not allow the particles to be trapped by the planet's own magnetic field and to form a ring current observed at Earth. The regions marked by green glow represents the regions which are Kelvin-Helmholtz unstable. The inset window shows a detail of one of the vertices which developed over time into a magnetic field hole. The lack of the magnetic field inside of the hole allows the particles to travel in the straight lines. The bottom panel of Figure 5.14 shows the synthetic data from the virtual flyby of the full scale simulation at the location (X,Y)/R_M = (-2.39, 1.73). The vertical dashed lines separate the vortexes as they pass by the probe. Interestingly, the time periods of 11.5, 14.4 and 31.5 seconds are in perfect agreement with the observations reported by ***Sundberg et al.*** [2012] who reported the values in the range between 10 and 20s. A separation between two consecutive vortexes is deduced from the saw-tooth pattern in the magnetic field data and a sudden jump in the perpendicular temperature signalling the magnetopause crossing.

5.7 Summary

The following two chapters summarize the findings from the numerical modelling of the planet Mercury. Each chapter represents a publication submitted into a scientific journal. Both papers build on the numerical models described above and each attempts to answer a scientific question raised by MESSENGER's science team. We combine observations from FIPS and MAG instruments described in Chap. 2 with numerical models developed in Chap. 3 and thoroughly tested in Chap. 4.

In the following Chapter 6, we provide a quantitative explanation of NASA MES-

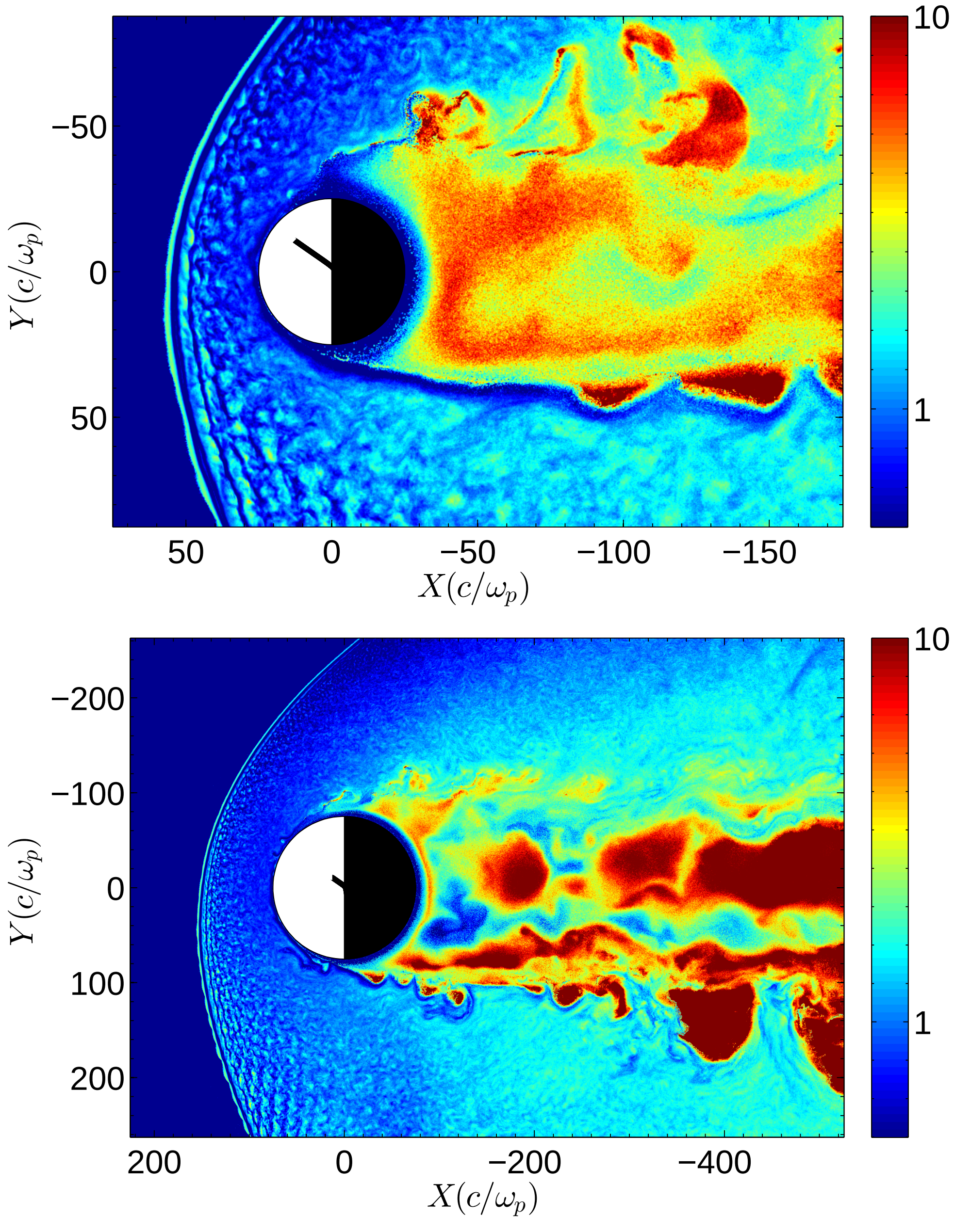

Figure 5.12: Scaled down (top) and full size (bottom) simulation runs respectively. A color coded thermal gyroradius of protons. Note, that the units of the radius r_L are same as the units used on the spatial axis.

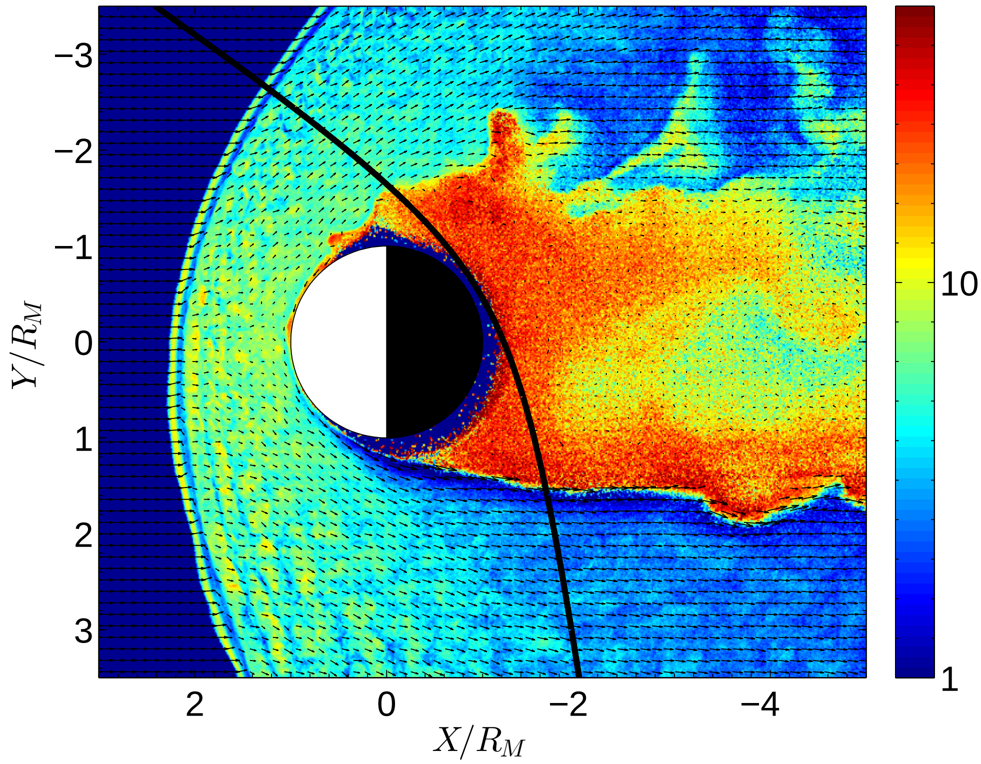

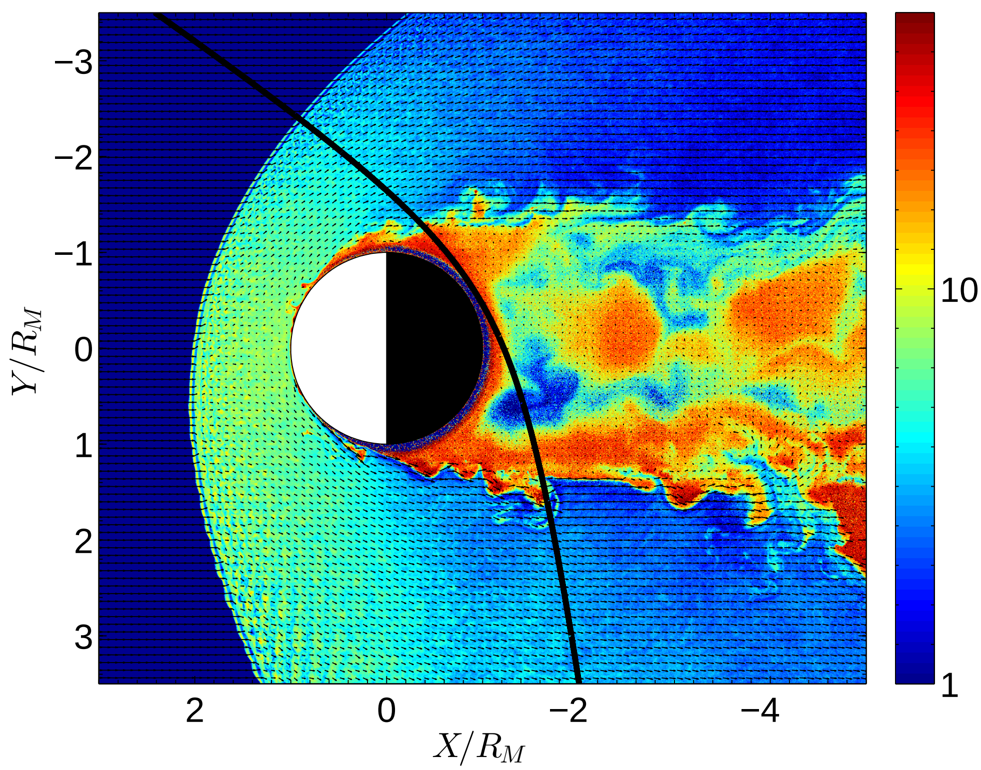

Figure 5.13: Scaled down (top) and full size (bottom) simulation runs respectively. A color coded perpendicular temperature of protons $T_\perp$ in the equatorial plane. The solid black line represents the third flyby of MESSENGER. The black arrows represent a projection of the proton bulk velocity into the X-Y plane.

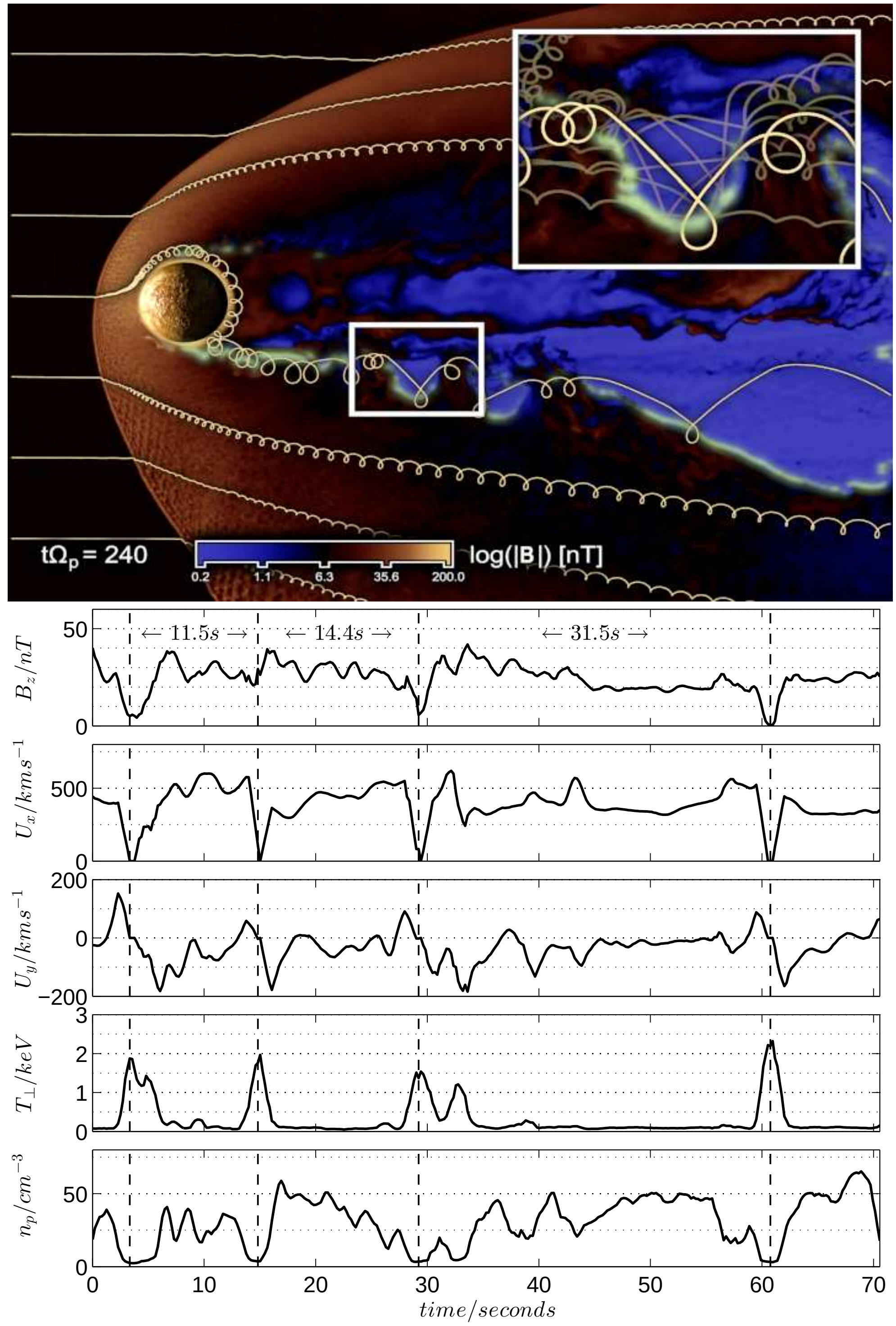

Figure 5.14: Top: A magnitude of the magnetic field $|B|$ at time $t\Omega_P = 240$ with the over-plotted trajectories of the sample particles. A green glow at the magnetopause represents a region unstable to the Kelvin-Helmholtz instability. Bottom: A virtual flyby at location (X,Y)/R_M = (-2.39, 1.73).

SENGER spacecraft observations of asymmetry in the dynamics of the dawn and dusk flanks of Mercury's magnetosphere. Through advanced global kinetic-hybrid computer simulations, we demonstrate that the Kelvin-Helmholtz instability (KHI) observed along the dusk magnetospheric flank is initiated near the sub-solar point, and that it grows convectively into large-scale vortices propagating anti-sunwards along the dusk-side magnetopause (MP). Time series extracted from the model along a simulated track approximating the third flyby of MESSENGER show a remarkable correspondence with real measurements: the numerical data contain saw tooth oscillations in the plasma density, flow, and magnetic field, and exhibit a dawn-dusk asymmetry in agreement with observations. It is shown that the observed asymmetry between dawn and dusk at Mercury is controlled by the finite gyro-radius of magnetospheric ions, their sense of rotation, and by magnetopause pressure gradients and large scale convection electric fields. Mercury's magnetosphere presents itself as a unique natural laboratory for studying kinetic-scale plasma regimes that are not present in other planetary magnetospheres, and not readily achievable in the laboratory.

In Chapter 7, we use particle tracing technique to study the spatial and energy distribution of heavy ions around Mercury which contribute to the exosphere of the planet. Two flybys of Mercury by the NASA MESSENGER spacecraft on January 14 and October 6, 2008 provide insight into the spatial distribution of the heavy ion exosphere around the planet. The relatively quiet solar wind conditions and interplanetary magnetic field (IMF) orientation allow us to compare "in-situ" observations with numerical simulations. During each flyby, the IMF had a strong radial Sun-Mercury direction but nonzero northward and southward component for the first (M1) and second (M2) flybys, respectively. We show that comparative studies of particle tracing in stationary electromagnetic fields from a self-consistent hybrid kinetic model provide a good characterization of Mercury's sodium ion exosphere when compared with MESSENGER observations.

Bibliography

Agre, C., J. Luhmann, D. Odstrcil, C. Schrijver, and Y. Li, Stream structure and coronal sources of the solar wind during the May 12th, 1997 CME, *J. Atmos. Sol.-Terr. Phy.*, *66*, 1295–1309, 2004.

Anderson, B. J., C. L. Johnson, H. Korth, M. E. Purucker, R. M. Winslow, J. A. Slavin, S. C. Solomon, R. L. McNutt, J. M. Raines, and T. H. Zurbuchen, The global magnetic field of Mercury from MESSENGER orbital observations., *Science*, *333*, 1859–62, 2011.

Andrews, G. B., T. H. Zurbuchen, B. H. Mauk, H. Malcom, L. A. Fisk, G. Gloeckler, G. C. Ho, J. S. Kelley, P. L. Koehn, T. W. LeFevere, S. S. Livi, J. M. Raines, and R. A. Lundgren, The Energetic Particle and Plasma Spectrometer Instrument on the MESSENGER Spacecraft, *Space Sci. Rev.*, *131*, 523–556, 2007.

Baker, D. N., D. Odstrcil, B. J. Anderson, C. N. Arge, M. Benna, G. Gloeckler, J. M. Raines, D. Schriver, J. A. Slavin, S. C. Solomon, R. M. Killen, and T. H. Zurbuchen, Space environment of Mercury at the time of the first MESSENGER flyby: Solar wind and interplanetary magnetic field modeling of upstream conditions, *J. Geophys. Res.*, *114*, A10,101, 2009.

Baker, D. N., D. Odstrcil, B. J. Anderson, C. N. Arge, M. Benna, G. Gloeckler, H. Korth, L. R. Mayer, J. M. Raines, D. Schriver, J. A. Slavin, S. C. Solomon, P. M. Trávníček, and T. H. Zurbuchen, The space environment of Mercury at the times of the second and third MESSENGER flybys, *Plan. Space Sci.*, *59*, 2066–2074, 2011.

Boardsen, S. A., T. Sundberg, J. A. Slavin, B. J. Anderson, H. Korth, S. C. Solomon, and L. G. Blomberg, Observations of Kelvin-Helmholtz waves along the dusk-side boundary of Mercury's magnetosphere during MESSENGER's third flyby, *Geophys. Res. Lett.*, *37*, L12,101, 2010.

Hasegawa, A., Plasma Instabilities and Non-linear Effects, in *Plasma Instabilities and Non-linear Effects*, p. chap. 3, Springer-Verlag, New York, 1975.

Ogilvie, K. W., J. D. Scudder, V. M. Vasyliunas, R. E. Hartle, and G. L. Siscoe, Observations at the planet Mercury by the plasma electron experiment: Mariner 10, *J. Geophys. Res.*, *82*, 1807–1824, 1977.

Raines, J. M., J. A. Slavin, T. H. Zurbuchen, G. Gloeckler, B. J. Anderson, D. N. Baker, H. Korth, S. M. Krimigis, and R. L. McNutt, MESSENGER observations of the plasma environment near Mercury, *Plan. Space Sci.*, *59*, 2004–2015, 2011.

Russell, C. T., and R. J. Walker, Flux transfer events at Mercury, *J. Geophys. Res.*, *90*, 11,067, 1985.

Shue, J.-H., J. K. Chao, H. C. Fu, C. T. Russell, P. Song, K. K. Khurana, and H. J. Singer, A new functional form to study the solar wind control of the magnetopause size and shape, *J. Geophys. Res.*, *102*, 9497–9511, 1997.

Slavin, J. A., Mercury's magnetosphere, *Adv. Space Res.*, *33*, 1859–1874, 2004.

Slavin, J. A., B. J. Anderson, M. H. Acuña, D. N. Baker, M. Benna, G. Gloeckler, R. E. Gold, G. C. Ho, R. M. Killen, H. Korth, R. L. McNutt, S. M. Krimigis, L. R. Nittler, J. M. Raines, S. C. Solomon, D. Schriver, P. M. Trávníček, R. D. Starr, T. H. Zurbuchen, and Others, Mercury's Magnetosphere After MESSENGER's First Flyby, *Science*, *321*, 85–89, 2008.

Slavin, J. A., R. P. Lepping, C.-C. Wu, B. J. Anderson, D. N. Baker, M. Benna, S. A. Boardsen, R. M. Killen, H. Korth, S. M. Krimigis, W. E. McClintock, R. L. McNutt, M. Sarantos, D. Schriver, S. C. Solomon, P. M. Trávníček, and T. H. Zurbuchen, MESSENGER observations of large flux transfer events at Mercury, *Geophys. Res. Lett.*, *37*, L02,105, 2010.

Sundberg, T., S. A. Boardsen, J. A. Slavin, B. J. Anderson, H. Korth, T. H. Zurbuchen, J. M. Raines, and S. C. Solomon, MESSENGER orbital observations of large-amplitude Kelvin-Helmholtz waves at Mercury's magnetopause, *J. Geophys. Res.*, *117*, 2012.

Trávníček, P. M., P. Hellinger, D. Schriver, D. Herčík, J. A. Slavin, and B. J. Anderson, Kinetic instabilities in Mercury's magnetosphere: Threedimensional simulation results, *Geophys. Res. Lett.*, *36*, L07,104, 2009.

Wang, Y.-M., and J. Sheeley, N. R., On potential field models of the solar corona, *The Astrophysical Journal*, *392*, 310, 1992.

Zurbuchen, T. H., G. Gloeckler, J. C. Cain, S. E. Lasley, and W. Shanks, A low weight plasma instrument to be used in the inner heliosphere, *SPIE conf. proc. Missions to the Sun II*, *3442*, 217–224, 1998.

Zurbuchen, T. H., J. A. Slavin, J. M. Raines, G. Gloeckler, S. M. Krimigis, P. L. Koehn, R. M. Killen, A. L. Sprague, R. L. McNutt, and S. C. Solomon, MESSENGER observations of the composition of Mercury's ionized exosphere and plasma environment., *Science*, *321*, 90–2, 2008.

Chapter 6

KHI Dawn-Dusk Asymmetry at Mercury

This chapter explains in detail observations by the NASA MESSENGER spacecraft, which reveal the presence of large amplitude plasma waves propagating along the dusk side flank of Mercurys magnetosphere. Results based on advanced computer simulations reveal why the plasma waves are observed where they are, and why they are precluded from the region where they might be expected to be present, but are not observed. The computer simulations are a first-of-a-kind in reproducing to a high degree the observations made by an actual spacecraft around a distant planet, and shed light on why Mercury is special in terms of being the closest planet to the Sun that has a magnetosphere. They provide synthetic data that is in agreement with the amplitudes of the waves observed by MESSENGER, their periodicity, and why they are initiated close to the subsolar point on the post noon magnetosphere. The chapter provides answers to important questions raised by the science teams in their publications, and through papers and presentations at international conferences, most notably the COSPAR meeting in Mysore, India, in July.

MESSENGER mission scientists anticipated the presence of large amplitude waves at Mercury, but they are ubiquitous to an extent that was not expected. For that reason, they are now viewed as being much more important in controlling how the magnetosphere of the planet responds to the solar wind, and how solar wind energy and particles are transferred to the magnetosphere, and how they sputter material off the surface. The observations by MESSENGER have revealed that the plasma waves at Mercury are initiated by a plasma instability known as the Kelvin-Helmholtz instability (KHI). This instability is driven by velocity shear between the solar wind flowing plasma, and plasma trapped within Mercurys magnetosphere. MESSENGER has shown that the KHI is much more common on the dusk side of the magnetosphere, and the prevalence of the waves and the asymmetry between dawn and dusk has become a hot topic. Observations of plasma waves and the KHI were elucidated in a special issue of Science devoted to MESSENGER, and important questions posed in the special issue (and referred to in our paper) are answered in our paper presented in this chapter.

6.1 Introduction

Mercury is the closest planet to the Sun, with an orbital radius that varies between 0.309-0.469 AU over a Mercury year (88 Earth days). It has a dipole-like magnetic field similar to Earth, but its dipole moment is smaller, in the range of 195 $\pm$ 10 nT R_M^3 *Anderson et al.* [2011]. Mercury is smaller than Earth at a radius R_M of 2439km (0.38 of Earth radii). It's proximity to the Sun means it is strongly affected *Slavin* [2004] by the solar wind, which creates a planetary magnetosphere with a size that is about 5% of that of Earth's magnetosphere. The density of solar wind particles and the strength of the Sun's magnetic field (IMF) are about an order of magnitude higher at Mercury. This means that the subsolar magnetopause stand-off distance is quite close to the surface of the planet, at a distance between 1.3 to 2.1 R_M *Slavin and Holzer* [1979] depending on the parameters of the solar wind. Physical processes at Mercury are much more dynamic *Fujimoto et al.* [2008] (timescales of seconds) due to the relatively high Alfvén speed in the solar wind at the orbit of the planet.

Prior to orbit insertion on March 18, 2011, the NASA MESSENGER (MErcury Surface, Space ENvironment, GEochemistry, and Ranging) spacecraft *Gold et al.* [2001] performed three *Slavin et al.* [2008]; *Zurbuchen et al.* [2008]; *Anderson et al.* [2011] nearly equatorial flybys. During the third flyby on September 29, 2009, MESSENGER recorded multiple magnetopause crossings that were interpreted as signatures of the Kelvin Helmholtz instability (KHI) *Boardsen et al.* [2010]. The KHI is of interest because it plays a strong role in controlling mass and energy transport throughout Mercury's as well as Earth's *Hasegawa et al.* [2004] magnetosphere. The observations reported by *Sundberg et al.* [2011, 2012] reveal that the KH-waves are routinely present, with a source region that is close to the subsolar point along the post-noon magnetopause. The KHI also produces disturbances over a large portion of the dayside magnetosphere *Sundberg et al.* [2012]. It is these observations that we attempt to explain here. It is demonstrated that Mercury's magnetic environment is dominated by kinetic-scale plasma dynamics that differentiate it from processes occurring in other planetary magnetospheres.

The methodology used to study the solar wind interaction with Mercury's magnetic field is "large scale hybrid-kinetic particle simulations" *Trávníček et al.* [2010]. The kinetic approach satisfies the requirement to resolve the finite gyro-radius *Nakamura et al.* [2010] of solar wind particles at Mercury, and provides synthetic particle and magnetic field data that can be compared directly with spacecraft observations. An important aspect of this comparison is that synthetic data contains statistical fluctuations related to how many particles are included in the simulation, whereas spacecraft data is limited by the characteristics of the instrument used to collect data, and the random fluctuations in the quantities being sampled. The statistical fluctuations in simulated data allow instabilities to form spontaneously out of noise that approximates that of the real system.

6.2 MESSENGER Spacecraft Observations of the KHI at Mercury

On September 29, 2009, MESSENGER was on an in-bound dusk-to-dawn trajectory in the night side equatorial magnetosphere, and had its first crossing of the magnetopause (MP) at around 21:27:10 MLT. As reported by *Boardsen et al.* [2010]; *Sundberg et al.* [2010], the spacecraft MAG instrument *Anderson et al.* [2007] recorded four saw-tooth patterns in the magnetic field in the intervening period from 21:28:10 to 21:29:50 MLT, during which time MESSENGER was at a radial distance of roughly 3 R_M (7320km), and slightly tail-ward of the dusk side flank. The saw-tooth oscillations observed by the spacecraft are evidence of the nonlinear stage of the KHI.

The IMF orientation in the magnetosheath prior to these saw-tooth oscillations varied from southward to northward *Boardsen et al.* [2010], but in the majority of cases where the KHI is observed the IMF is strongly northward *Sundberg et al.* [2012]. This configuration where the IMF is parallel to the planetary magnetic field in the magnetosphere is favorable for the KHI along the equatorial magnetospheric flanks *Fairfield et al.* [2000]. The September 29 and subsequent observations show a clear asymmetry in the KHI in favour of dusk *Sundberg et al.* [2012], which will be explained through consideration of asymmetries in the forces acting on the ions at dusk and dawn.

6.3 Hybrid Kinetic Model of the Solar Wind Interaction with Mercury

A hybrid-kinetic (particle ions and massless fluid electrons) computer model of the solar wind interaction with Mercury is used. The procedure and algorithm upon which the model is based is detailed in *Matthews* [1994]. The magnetosphere is assumed to be two-dimensional (2D) and oriented to lie in the equatorial plane of the planetary orbit of Mercury about the Sun. This approximation corresponds to a planet that is topologically a long cylinder with its axis perpendicular to the Sun-Mercury line in the equatorial plane. The distribution function of protons is initially Maxwellian and constructed using 120 particles in each numerical cell of rectangular size $\triangle_x$ = 0.3 c/ω_{pi} (9.7 km). Here, $\omega_{pi}^2 = n_p e^2/m_p \epsilon_0$ is the proton plasma frequency, c is the speed of light, e is the electron charge, ϵ_0 is the vacuum permittivity, and n_p and m_p are the proton density and mass, respectively. The size of the rectangular simulation domain is $L_x \times L_y \sim 750^2 c/\omega_{pi}$ (24000^2 km), and the time step for advancing particle positions is 0.008 Ω_{pi}^{-1} (4.2 ms), where $\Omega_{pi} = eB/m_p$ is the proton gyro-period. The IMF and solar wind velocity take values of 20 nT and 300 km/s, respectively *Baker et al.* [2011]. The boundary conditions are as described in *Trávníček et al.* [2010]. The only difference is that particles hitting the surface of the planet suffer specular reflection, and there is no injection from the surface. The planetary field is dipolar *Anderson et al.* [2011] at the start of the simulation, with a dipole moment of 195 nT R_M^3. A limitation set by computer resources is that the simulated planet is one third the size of the real system. The stand-off (bow-shock) distance of the solar wind from the surface, and solar wind velocities, are the same as the real system, but timescales are three times faster due to the scale difference between the simulated and actual planetary magnetosphere. Consequences of this are discussed later in the paper.

6.4 Kelvin-Helmholtz Instability (KHI) at Mercury

The KHI is driven by velocity shear and favors an orientation of the IMF that is parallel to the planetary magnetic field in the equatorial magnetosphere. At Earth, the instability is typically observed on the low latitude magnetospheric flanks *Foullon et al.* [2008] where fast flowing plasma in the magnetosheath transitions to slow moving less dense plasma earthward of the magnetopause (MP). The amplitude of KHI waves at Earth is reported to be in the range of 30-50 nT *Chen et al.* [1993], while amplitudes at Mercury are in excess of 40 nT *Boardsen et al.* [2010]; *Sundberg et al.* [2012]. Mercury is also more dynamic, with KHI characteristic timescales in the range of seconds *Boardsen et al.* [2010] compared to minutes at Earth. Finite ion gyro-radius effects play a more important role at Mercury because of the large difference in size of the respective magnetospheres, and the fact that the ion gyroradius at Mercury can be comparable to the size of the planet. This is important because the simulations reveal that the finite gyro-radius of magnetosheath ions and the convection electric field parallel to the velocity shear gradient at dawn, broaden the shear layer in which vortices start to form. This lowers the growth rate, and is consistent with results of 2.5D PIC simulations by Nakamura et al. (2010) *Nakamura et al.* [2010]. The opposite conditions apply at dusk, which is a factor in explaining why the KHI preferentially occurs at dusk.

Figure 1. shows two instances of time (10 gyroperiods apart) in the simulated evolution of plasma density around Mercury. The full animation of the density evolution is provided in supplementary material (S1), which shows clearly that the KHI is initiated close to noon and that it grows convectively along the flank magnetopause. The IMF is northward with solar wind flowing from the left compressing the dayside magnetosphere and moving it toward the planet. Material which accumulates in the vicinity of the sub-solar point escapes to the nightside through a relatively small opening or nozzle. This causes plasma to be accelerated tail-ward starting at low velocity, thus forming a velocity shear between the escaping plasma and slower moving less dense plasma adjacent to the planet. The relatively slow moving plasma in the vicinity of the subsolar point is unstable and evolves through the KHI on the dusk-side magnetospheric flank into large scale vortical structures that move with the direction of the bulk flow. It is the initiation and growth of these vortical structures that we would like to explain.

To understand the evolution of the KHI at Mercury, it is informative to consider what plasma conditions affect the instability growth rate. A simple approximation to the growth rate of the KHI for a step-like change in the plasma flow velocity can be obtained from ideal MHD in the incompressible gas limit *Hasegawa* [1975]. This yields a threshold condition for the KHI that is defined by,

$$(\mathbf{k}\cdot\mathbf{v}_0)^2 - \frac{n_1+n_2}{n_1 n_2}\left[n_1(\mathbf{k}\cdot\mathbf{v}_{A1})^2 + n_2(\mathbf{k}\cdot\mathbf{v}_{A2})^2\right] > 0 \tag{6.1}$$

In this expression, subscripts 1 and 2 denote quantities on either side of the velocity shear, which is regarded as a boundary of zero thickness. The quantities n and $\mathbf{v}_A$ denote number density and Alfven velocity respectively; $\mathbf{k}$ and $\mathbf{v}_0$ correspond to the KHI wave vector and jump in plasma streaming velocity, respectively. To identify the jump in velocity, the velocity gradient is monitored in the y-direction, assuming a finite thickness $\triangle$ that corresponds to conditions for maximum growth of the KHI defined by Miura and Pritchett *Miura and Pritchett* [1982], i.e., $k\triangle \sim 0.8$. Here k is defined by the wavelength of vortices in the simulations. Assuming $\mathbf{k}$ parallel to $\mathbf{v}_0$, the magnetospheric regions where the threshold condition is exceeded are indicated

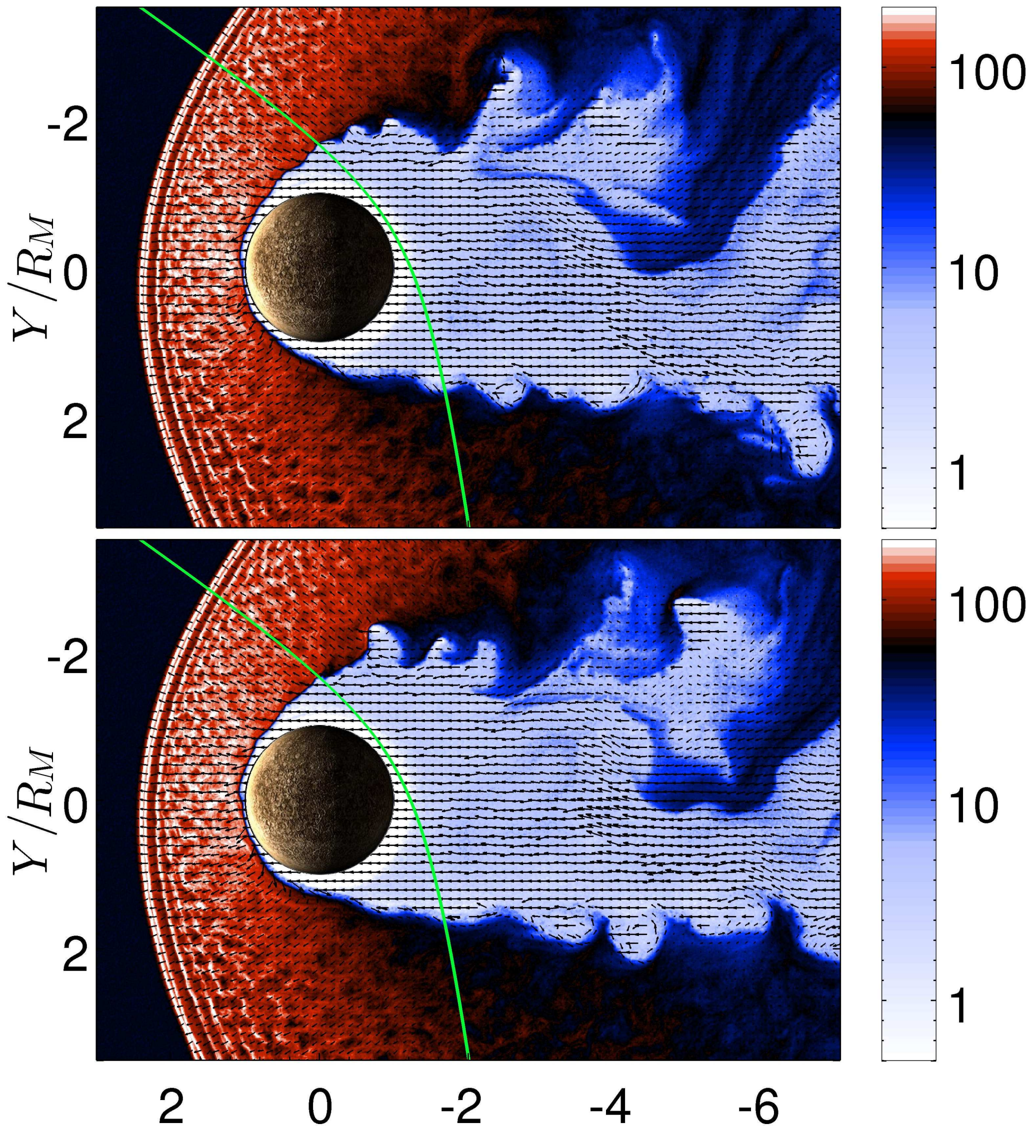

Figure 6.1: Figure 1: The ion density obtained from the computer model is shown on a logarithmic scale in the units cm^{-3} together with velocity vectors (represented by arrows) in the frame of the solar wind, and for different times $t\Omega_{pi} = 125$ and 135 respectively. The minimum number of velocity vectors is shown to make the vortices visible. The solid line represents the trajectory of the third flyby of MESSENGER on September 29, 2009.

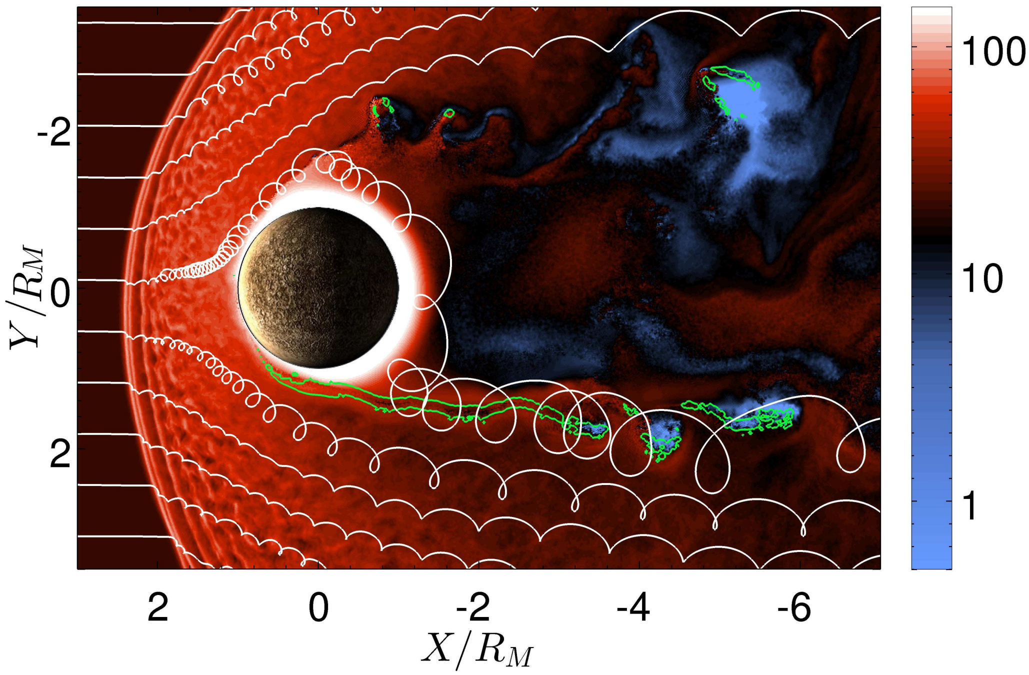

Figure 6.2: Figure 2: The magnitude of the magnetic field **B** at time $t\Omega_{pi} = 135$ is represented by a logarithmic color scale in the units of nT. Over-plotted are trajectories of particles traced from the solar wind as they interact with the magnetic field of the planet. The green curves extending tailward along the dawn (Y $\sim$ -1.5) and dusk (Y $\sim$ 1.5) magnetopause visualize regions most unstable to the Kelvin-Helmholtz instability (KHI). The asymmetry of the unstable regions favors a KHI along dusk. The flow is laminar in the region where the KHI forms because the convection electric field E_y is anti-parallel to the velocity-shear gradient. This acts to sustain the gradient by preventing drift of the ions out of the shear layer.

by the green lines on Figure 2. The post-noon MP extending from the dayside to the distant magnetotail (10 R$_M$) supports laminar-type flow. This implies that the KHI initiated on the dusk magnetospheric flank is able to grow convectively into large scale vortices. The dawn flank, on the other hand, exhibits only sporadic pockets of unstable growth and lacks the coherence that is necessary for the KHI to grow convectively with the solar wind flow over several cycles.

Figure 2. also shows the magnitude of the magnetic field around the planet, and spiral motion of selected test particle ions moving at approximately the solar wind flow velocity. Although plasma is diverted around the dayside boundary in the expected manner for a planetary magnetosphere, it penetrates significantly across the bowshock

with the result that the plasma density is high along dawn compared to dusk, and the bowshock position is moved outward relative to the dayside boundary. This implies plasma and magnetic field gradients are weaker at dusk than at dawn. The particle traces in Fig. 2 illustrate trajectories of protons with energies typical of the solar wind flow kinetic energy per ion. The gyroradius is comparable with the width of the simple ideal-MHD unstable region marked in green on the figure, which confirms that kinetic effects are important in the evolution of the KHI at Mercury.

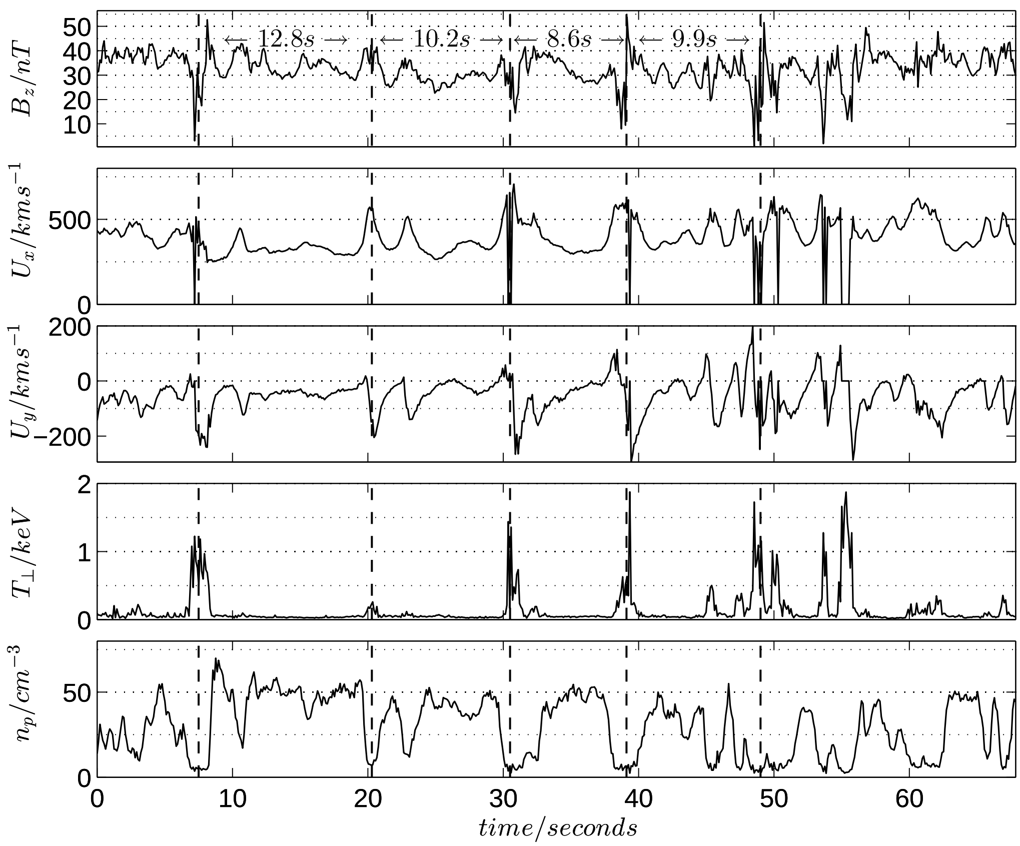

Figure 6.3: Figure 3: A virtual flyby through synthetic data at location X,Y = (-2.03, 1.74) R$_M$ of the B_z component of the magnetic field; bulk flow velocity U_x, U_y; perpendicular proton temperature $T_\perp$; and proton density n_p. The figure is based on a coordinate system in which the x-axis points from Mercury to the Sun; the z-axis is along the dipole-moment of the planet; the y-axis completes the right-hand system. Horizontal dashed lines represent boundaries of Kelvin-Helmholtz vortices as they pass over the virtual satellite. A saw-tooth pattern in B_z is typical for KH observations.

Figure 3. shows synthetic time series of $(B_z, U_x, U_y, T_\perp, n)$ obtained from the

simulation. The time series are extracted at a location on the dusk magnetopause where KHI vortices are observed to form, i.e., close to the trajectory of the third flyby illustrated by the solid line in Fig. 1. In the synthetic time series, there are obvious regular saw-tooth patterns in the density, and similar features in the x-component bulk velocity. The periodicity is on the order of 8-13 seconds, and is a consequence of the magnetopause boundary sweeping back and forth across the spacecraft as KHI waves move past it. The amplitude of the magnetic perturbations in the first panel of Figure 3. is on the order of 15-20 nT, while the transverse $y-$component velocity is about 100km/s. The bottom two panels of Figure 3. show, respectively, magnetopause crossings of high temperature, low density magnetospheric plasma with low temperature, high density magnetosheath plasma. Taking account of the one-third scale difference between the modelled and real magnetosphere, these values compare favourably with those reported by MESSENGER. The perpendicular components of the magnetic field perturbations B_x and B_y are not shown because the IMF is purely northward in the simulation, and is performed in the equatorial plane. Although the pattern of magnetic saw-tooth oscillations is similar to that of the velocity perturbations, their amplitude is very small because of the assumed geometry.

6.5 Discussion

Computer simulation results reproduce quantitative aspects of the KHI observed by MESSENGER. The asymmetry of the KHI and its preference for the dusk-side flank is shown to be a consequence of asymmetry in dawn and dusk particle motions. On the dusk side of Mercury's magnetosphere, the convection electric field E_y is anti-parallel to the velocity shear gradient and acts to maintain it. The maintenance of laminar flow at dusk then allows the KHI to grow convectively in the tail-ward direction. The direction of the convection electric field E_y acting parallel to the shear gradient reinforces outward plasma motion at dawn, which leads to broadening of the region in which vortices try to form. Although the KHI is not excluded from the dawn flank, the expectation is that conditions resulting in instability should be less common around dawn. The possibility of an asymmetry in the KHI at Earth also exists, but the evidence is not so clear. For example, toroidal mode plasma waves on the dawn side of the magnetosphere, as reported by Anderson et al. (1990) *Anderson et al.* [1990], and Takahashi et al. (2002) *Takahashi* [2002], have been attributed to the KHI. This is supported by global MHD simulations reported by Claudepierre et al. (2008) *Claude-*

pierre et al. [2008]. On the other hand, Taylor et al. (2012) *Taylor et al.* [2012] have suggested that the KHI is more prevalent around dusk, which is in agreement with observations at Mercury. On the dawn flank at Mercury, the dynamics of the plasma is such that plasma bubbles form in a a manner that is suggestive of a Rayleigh-Taylor-like (RT) instability. Such a possibility has been considered by Gratton et al. (1996) *Gratton et al.* [1996], but for the solar wind interaction with Earth's geomagnetic field.

The hybrid-kinetic simulations show agreement with MESSENGER observations in that the KHI is first initiated in the vicinity of the subsolar point where the plasma flow is still accelerating tailward. This is supported by a simplified analysis of the ideal-MHD instability condition for the KHI. Another potential contribution to the onset of the KHI that we have not considered arises due to the finite gyroradius of ions in the vicinity of the subsolar point, where shear in the diamagnetic drift velocity $v_{di} = (\rho\Omega_{ci}B_0)^{-1}\mathbf{B}_0 \times \nabla P_i$ can be unstable to the KHI *Miura* [2003]. In either situation, global-hybrid kinetic simulations reveal that as vortices move along the dusk flank, they continue to grow convectively within the bulk flow. Another important aspect of Mercury's magnetosphere that we have not considered is the presence of heavy ions. It has been suggested *Sundberg et al.* [2011] that increased mass loading will enhance the KHI along the dusk flank and create a barrier to the KHI along the dawn flank. The simulations reported here suggest that vortices can form in the absence of heavy ions. It can be concluded that the small scale of Mercury's magnetosphere in comparison to Earth reveals important differences that will be interesting to assess in the context of other planetary magnetospheres influenced by kinetic scale plasma physics.

Bibliography

Anderson, B. J., M. J. Engebretson, S. P. Rounds, L. J. Zanetti, and T. A. Potemra, A statistical study of Pc 35 pulsations observed by the AMPTE/CCE Magnetic Fields Experiment, 1. Occurrence distributions, *J. Geophys. Res.*, *95*, 10,495, 1990.

Anderson, B. J., M. H. Acuña, D. A. Lohr, J. Scheifele, A. Raval, H. Korth, and J. A. Slavin, The Magnetometer Instrument on MESSENGER, *Space Sci. Rev.*, *131*, 417–450, 2007.

Anderson, B. J., C. L. Johnson, H. Korth, M. E. Purucker, R. M. Winslow, J. A. Slavin, S. C. Solomon, R. L. McNutt, J. M. Raines, and T. H. Zurbuchen, The global magnetic field of Mercury from MESSENGER orbital observations., *Science*, *333*, 1859–62, 2011.

Baker, D. N., D. Odstrcil, B. J. Anderson, C. N. Arge, M. Benna, G. Gloeckler, H. Korth, L. R. Mayer, J. M. Raines, D. Schriver, J. A. Slavin, S. C. Solomon, P. M. Trávníček, and T. H. Zurbuchen, The space environment of Mercury at the times of the second and third MESSENGER flybys, *Plan. Space Sci.*, *59*, 2066–2074, 2011.

Boardsen, S. A., T. Sundberg, J. A. Slavin, B. J. Anderson, H. Korth, S. C. Solomon, and L. G. Blomberg, Observations of Kelvin-Helmholtz waves along the dusk-side boundary of Mercury's magnetosphere during MESSENGER's third flyby, *Geophys. Res. Lett.*, *37*, L12,101, 2010.

Chen, S.-H., M. G. Kivelson, J. T. Gosling, R. J. Walker, and A. J. Lazarus, Anomalous Aspects of Magnetosheath Flow and of the Shape and Oscillations of the Magnetopause During an Interval of Strongly Northward Interplanetary Magnetic Field, *J. Geophys. Res.*, *98*, 5727–5742, 1993.

Claudepierre, S. G., S. R. Elkington, and M. Wiltberger, Solar wind driving of magnetospheric ULF waves: Pulsations driven by velocity shear at the magnetopause, *J. Geophys. Res.*, *113*, 2008.

Fairfield, D. H., A. Otto, T. Mukai, S. Kokubun, R. P. Lepping, J. T. Steinberg, A. J. Lazarus, and T. Yamamoto, Geotail observations of the Kelvin-Helmholtz instability at the equatorial magnetotail boundary for parallel northward fields, *J. Geophys. Res.*, *105*, 21,159, 2000.

Foullon, C., C. J. Farrugia, A. N. Fazakerley, C. J. Owen, F. T. Gratton, and R. B. Torbert, Evolution of Kelvin-Helmholtz activity on the dusk flank magnetopause, *J. Geophys. Res.*, *113*, A11,203, 2008.

Fujimoto, M., W. Baumjohann, K. Kabin, R. Nakamura, J. A. Slavin, N. Terada, and L. Zelenyi, Hermean Magnetosphere-Solar Wind Interaction, *Space Sciences Series of ISSI*, *26*, 347–368, 2008.

Gold, R. E., S. C. Solomon, R. L. McNutt, A. G. Santo, M. H. Acuña, J. B. Abshire, B. J. Anderson, R. S. Afzal, G. B. Andrews, P. D. Bedini, J. C. Cain, A. F. Cheng, L. G. Evans, W. C. Feldman, R. B. Follas, G. Gloeckler, J. O. Goldsten, S. E. Hawkins, N. R. Izenberg, S. E. Jaskulek, E. A. Ketchum, M. R. Lankton, D. A. Lohr, B. H. Mauk, W. E. McClintock, S. L. Murchie, C. E. Schlemm, D. E. Smith, R. D. Starr, and T. H. Zurbuchen, The MESSENGER mission to Mercury: scientific payload, *Plan. Space Sci.*, *49*, 1467–1479, 2001.

Gratton, F. T., C. J. Farrugia, and S. W. H. Cowley, Is the magnetopause Rayleigh-Taylor unstable sometimes?, *J. Geophys. Res.*, *101*, 4929–4937, 1996.

Hasegawa, A., Plasma Instabilities and Non-linear Effects, in *Plasma Instabilities and Non-linear Effects*, p. chap. 3, Springer-Verlag, New York, 1975.

Hasegawa, H., M. Fujimoto, T.-D. Phan, H. Rème, A. Balogh, M. W. Dunlop, C. Hashimoto, and R. Tandokoro, Transport of solar wind into Earth's magnetosphere through rolled-up Kelvin-Helmholtz vortices., *Nature*, *430*, 755–8, 2004.

Matthews, A., Current advance method and cyclic leapfrog for 2D multispecies hybrid plasma simulations, *J. Comput. Phys.*, *112*, 102–116, 1994.

Miura, A., Nonideal high-β magnetohydrodynamic Kelvin-Helmholtz instability driven by the shear in the ion diamagnetic drift velocity at the subsolar magnetopause, *J. Geophys. Res.*, *108*, 1076, 2003.

Miura, A., and P. L. Pritchett, Nonlocal Stability Analysis of the MHD Kelvin-Helmholtz Instability in a Compressible Plasma, *J. Geophys. Res.*, *87*, 7431–7444, 1982.

Nakamura, T. K. M., H. Hasegawa, and I. Shinohara, Kinetic effects on the Kelvin-Helmholtz instability in ion-to-magnetohydrodynamic scale transverse velocity shear layers: Particle simulations., *Phys. Plasmas*, *17*, 2010.

Slavin, J. A., Mercury's magnetosphere, *Adv. Space Res.*, *33*, 1859–1874, 2004.

Slavin, J. A., and R. E. Holzer, The Effect of Erosion on the Solar Wind Stand-Off Distance at Mercury, *J. Geophys. Res.*, *84*, 2076–2082, 1979.

Slavin, J. A., B. J. Anderson, M. H. Acuña, D. N. Baker, M. Benna, G. Gloeckler, R. E. Gold, G. C. Ho, R. M. Killen, H. Korth, R. L. McNutt, S. M. Krimigis, L. R. Nittler, J. M. Raines, S. C. Solomon, D. Schriver, P. M. Trávníček, R. D. Starr, T. H. Zurbuchen, and Others, Mercury's Magnetosphere After MESSENGER's First Flyby, *Science*, *321*, 85–89, 2008.

Sundberg, T., S. Boardsen, J. A. Slavin, L. Blomberg, and H. Korth, The Kelvin-Helmholtz instability at Mercury: An assessment, *Plan. Space Sci.*, *58*, 1434–1441, 2010.

Sundberg, T., S. A. Boardsen, J. A. Slavin, L. G. Blomberg, J. A. Cumnock, S. C. Solomon, B. J. Anderson, and H. Korth, Reconstruction of propagating Kelvin-Helmholtz vortices at Mercury's magnetopause, *Plan. Space Sci.*, *59*, 2051–2057, 2011.

Sundberg, T., S. A. Boardsen, J. A. Slavin, B. J. Anderson, H. Korth, T. H. Zurbuchen, J. M. Raines, and S. C. Solomon, MESSENGER orbital observations of large-amplitude Kelvin-Helmholtz waves at Mercury's magnetopause, *J. Geophys. Res.*, *117*, 2012.

Takahashi, K., Toroidal wave frequency at L = 610: Active Magnetospheric Particle Tracer Explorers/CCE observations and comparison with theoretical model, *J. Geophys. Res.*, *107*, 1020, 2002.

Taylor, M. G. G. T., H. Hasegawa, B. Lavraud, T. Phan, C. P. Escoubet, M. W. Dunlop, Y. V. Bogdanova, A. L. Borg, M. Volwerk, J. Berchem, O. D. Constantinescu, J. P. Eastwood, A. Masson, H. Laakso, J. Soucek, A. N. Fazakerley, H. U. Frey, E. V. Panov, C. Shen, J. K. Shi, D. G. Sibeck, Z. Y. Pu, J. Wang, and J. A. Wild, Spatial distribution of rolled up Kelvin-Helmholtz vortices at Earth's dayside and flank magnetopause, *Ann. Geophys.*, *30*, 1025–1035, 2012.

Trávníček, P. M., D. Schriver, P. Hellinger, D. Herčík, B. J. Anderson, M. Sarantos, and J. A. Slavin, Mercurys magnetospheresolar wind interaction for northward and southward interplanetary magnetic field: Hybrid simulation results, *Icarus*, *209*, 11–22, 2010.

Zurbuchen, T. H., J. A. Slavin, J. M. Raines, G. Gloeckler, S. M. Krimigis, P. L. Koehn, R. M. Killen, A. L. Sprague, R. L. McNutt, and S. C. Solomon, MESSENGER observations of the composition of Mercury's ionized exosphere and plasma environment., *Science*, *321*, 90–2, 2008.

Chapter 7

Sodium Exosphere of Mercury

In this chapter we employ numerical hybrid code developed in Chapter 3 to model magnetospheric environment of the planet Mercury. We use electromagnetic field obtained from hybrid simulations to trace sodium ions during two virtual flybys of the MErcury Surface, Space ENvironment, GEochemistry and Ranging (MESSENGER) spacecraft. Although the electromagnetic fields were produced using the self-consistent hybrid code, in this chapter we use only a static snapshot of the fields. Advancing algorithm for the particles is described in the Chapter 3 and is the same algorithm which is used for the hybrid code. The results were published in Geophysical Research Letters 2010 with as a collaboration of following authors: Jan Paral, Pavel M. Trávníček, Robert Rankin, and David Schriver. The paper "Sodium ion exosphere of Mercury during MESSENGER flybys" [*Paral et al.*, 2010] is included below.

7.1 Introduction

An extensive study of planet Mercury began after the discovery of its intrinsic magnetic field by Mariner 10 in 1974/75 [*Ness et al.*, 1974]. It was also revealed that Mercury has an exospheric environment [*Broadfoot et al.*, 1976] not very different from Earth. Recently, the NASA MESSENGER spacecraft visited Mercury by performing three equatorial flybys on January 14, 2008 (M1), October 6, 2008 (M2), and September 29, 2009. These predate the orbital phase of the mission, which is scheduled to begin on March 18, 2011. During M1 and M2, the interplanetary magnetic field (IMF) had a strong radial Sun-Mercury component with nonzero northward component B_z during M1, and south-pointing B_z during M2. The solar wind conditions were relatively quiet for both flybys, providing two typical but quantitatively different cases of IMF orientation to investigate. From the information already provided by MESSENGER, it has been found that the intrinsic magnetic field of the planet is dipole-like, with a magnetic moment of 250 nT R_M^3 [*Slavin et al.*, 2009]. Because of sun shadowing of the spacecraft, there are no direct measurements of solar wind parameters, and estimates must come from solar wind expansion models. Nevertheless, the flybys have revealed that Mercury's magnetosphere has a striking resemblance to Earth, with similar phenomena such as Kelvin-Helmholtz vortexes on the flanks, plasmoid formation, and other phenomena [*Slavin et al.*, 2008, 2010].

The MESSENGER spacecraft carries instruments relevant to the study of the heavy ion exosphere of Mercury, including Fast Imaging Plasma Spectrometer (FIPS) as a part of the Energetic Particle and Plasma Spectrometer (EPPS). The FIPS-EPPS instrument counts heavy ions for various ranges of m/q ratio, where m and q are particle mass and charge, respectively. The FIPS instrument covers an energy range from tens of eV to 13.5 keV, and provides coverage of approximately 1.4π steradians solid angle. The actual field of view is limited by the fact that the instrument is shielded from the Sun and so caution is necessary when the sunshade is between the instrument's field of view and the bulk plasma flow direction, because only the supra-thermal population of plasma contributes to the measurement. A summary of measurements taken during the M1 flyby is given by *Zurbuchen et al.* [2008], who concluded that the most abundant heavy ion species is sodium. Although note that instrument can not differentiate between atomic masses 23 and 24. During the M1 flyby FIPS recorded an accumulation of Na^+ on the dusk side in the equatorial plane and in the vicinity of the inbound magnetopause crossing. Note that data from M2 were not published as of this writing.

The source of Mercury's sodium exosphere is the surface of the planet, which refills the planetary environment by ejecta from the regolith. At least two major releasing processes contribute to the source of this new material: Photo-Stimulated Desorption (PSD) and Solar Wind Sputtering (SWS). The PSD process is active on the dayside of the planet, with the maximum flux of ejected particles occurring at the sub-solar point because of solar wind photons that directly excite surface atoms. The SWS process is due to solar wind ions and energetic atoms that impinge on the surface at highly localized auroral and mid-latitude regions, as discussed in *Paral et al.* [2009].

The objective of this paper is to carry out quantitative numerical studies of two cases that are similar to the M1 and M2 flybys. We model the spatial distribution of the sodium ion exosphere, and compare it with data taken by MESSENGER during the first flyby. The methodology involves test-particle ion tracing in the electromagnetic fields provided by a self-consistent Hybrid model. This extends previous work by *Sarantos et al.* [2009].

7.2 Initialization

7.2.1 Hybrid simulation

In our studies, we use the hybrid self-consistent numerical model, where ions are treated kinetically and electrons are described as a massless charge neutralizing fluid. The system consists of a 3D rectangular cartesian grid with spatial resolution $dL = 0.4 \times 1.0 \times 1.0\ c/\omega_{p,sw}$, where c is the speed of light and $\omega_{p,sw}$ is the solar wind proton plasma frequency. The simulation box domain length is $L = 237.6 \times 286 \times 286 c/\omega_{p,sw}$. We use background fields obtained from two simulations described in detail by *Trávníček et al.* [2007]. The IMF is defined through its Cartesian components with northward $\mathbf{B}^{IMF} = (0.94, 0, 0.34)B_{sw}$ and southward IMF $(0.94, 0, -0.34)B_{sw}$ corresponding to HYB1 and HYB2, respectively. We assume solar wind parameters: magnitude of IMF $B_{sw} = 18$ nT; solar wind density of protons $n_{sw} = 32$ cm^{-3} for both study cases.

7.2.2 Particle tracing

We consider photo-stimulated desorption (PSD) and solar wind sputtering (SWS) to be two major release mechanisms responsible for refilling the exosphere of Mercury with neutral and ionized sodium. Each process releases particles as neutral atoms but 1% of sodium is already ionized when ejected [*Milillo et al.*, 2005]. We neglect micro-meteorite vaporization because the contribution to the total content of exospheric sodium is not expected to exceed ∼20% and ∼4% of SWS and PSD, respectively [*Killen et al.*, 2004].

The spatial distribution of solar wind sputtering is highly dependent on the orientation of the IMF [*Delcourt et al.*, 2003]. The orientation and magnitude of the IMF is also a key parameter responsible for opening the magnetosphere to entry of solar wind ions along open field lines. The energy transmitted during each sputtering interaction is $T = T_m \cos^2(\alpha_r)$, where α_r is the recoil angle and the maximal transmitted energy T_m between an incident particle with energy E_i and mass m_1, and sputtered particle of mass m_2, is given by $T_m = E_i(4m_1m_2)/(m_1 + m_2)^2$. We only consider H^+ and Na/Na^+ to be the interacting species. The energy distribution function is described by

$$f_s(E_e, T_m) = \frac{E_e}{(E_e + E_b)^3}\left[1 - \left(\frac{E_e + E_b}{T_m}\right)^{1/2}\right], \tag{7.1}$$

where $E_b = 2$ eV is the surface binding energy, E_e is the energy of the emitted particle. We consider T_m to be 500 eV in both cases. The angular distribution function is $\cos^\gamma(\alpha_n)$, where γ is a number between 1 and 2 (in our case, we use 1) and α_n is the angle between the normal to the surface and the initial velocity. The total number of particles ejected from the surface per second Φ^{SWS} was estimated by ***Killen et al.*** [2004] to be between 6.0×10^{21} and 3.8×10^{24} s^{-1} particles, based on solar wind parameters that range from $n_{sw} = 10 - 90$ cm^{-1}, $v_{sw} = 350 - 750$ km s^{-1}, and $5 - 30\%$ of the surface open to the solar wind. Assuming the solar wind conditions to be $n_{sw} = 32$ cm^{-1}, $v_{sw} = 350$ km s^{-1}, and surface open to the solar wind to be 17.0 % and 13.7 %, respectively, we set the flux Φ_0^{SWS} to be 9.6×10^{23} and 8.0×10^{23} s^{-1} for HYB1 and HYB2, respectively. We apply a self-consistent flux distribution of solar wind protons over the planet surface using results of the hybrid simulations of ***Trávníček et al.*** [2007] as initial conditions for our model, as well as in determining the surface area which is open to solar wind protons.

The energy distribution function of photon stimulated desorption can be closely approximated [*Johnson et al.*, 2002] by the energy distribution function:

$$f(E) = x(1 + x)\frac{EU^x}{(E + U)^{2+x}}, \tag{7.2}$$

where $x = 0.7$ and $U = 0.052$ eV. This function has its maximum at approximately half of the binding energy U, and contains a long high energy tail as compared to the Maxwell-Boltzmann energy distribution [***Mura et al.***, 2007]. The surface flux of ejected particles is dependent on the angle ϕ between zenith and the subsolar point and is defined as $\Phi_n(\phi) = \Phi_n^* \cos(\phi)(R/R^*)^2$. The number of particles through the surface Φ^{PSD} is unknown but was estimated by ***Killen et al.*** [2004] to be between 5.0×10^{24} and 1.0×10^{25} s^{-1}. We choose a PSD rate of $\Phi_0^{PSD} = 5.0 \times 10^{24}$ s^{-1} for both simulations as it provides a baseline fit to the MESSENGER UV measurements of emission from neutral Na [***Burger et al.***, 2010]. Note, however, the PSD flux must be increased by a factor of 4 on areas open to the solar wind to match the sodium enhancements observed by MESSENGER above Mercurys polar regions.

Peak ion densities in Fig. 7.2a,b along the virtual trajectory are normalized by the factor $M_{1,2} = max(n_{SWS} + n_{PSD})$ where M_1 = 13.7 and M_2 = 4.7 ions cm^{-3} for HYB1 and HYB2, respectively. The factors M_1 and M_2 correspond to the values of Φ_0^{PSD} and Φ_0^{SWS} defined earlier, assuming the density scales linearly with the surface flux.

The photoionization life time τ_p for sodium was estimated to be $5\times10^4-4\times10^5$s at a mean orbit of 0.386 AU [***Milillo et al.***, 2005]. Because photoionization is dependent on photon flux, we scale the ionization time using the actual distance from the Sun during the given flyby using $\tau = \tau^*(R/R^*)^2$ where $R^* = 0.386$ AU and R is the distance from the Sun (0.307 - 0.467 AU). We use values of 0.353 and 0.341 AU for M1 and M2, respectively. For both simulations we use $\tau_p^* = 5\times10^4$s. Each neutral particle carries a weight w of unity at the time of surface ejection. This value is decreased every timestep by $\mathrm{d}w/\mathrm{d}t = w(t)\tau_p^{-1}$, where τ_p is a typical photoionization time. We neglect ionization due to charge exchange which has a much longer ionization time. The weight decrement dw is accumulated on the mesh and when it reaches unity an ion is released in the given cell with the local velocity distribution of the neutral particles. In the neutral state, only gravitation and acceleration pressure forces act on particles. The gravity force is approximately 3.697 m/s^2 but the radiation pressure acceleration a_{rp} varies due to the Doppler shifted photon flux, and can be between 0.2 to 2 m/s^2. To account for the relative velocity of the planet and Sun during the flybys we assume a_{rp} to be ~ 1.8 m/s^2 for both simulations.

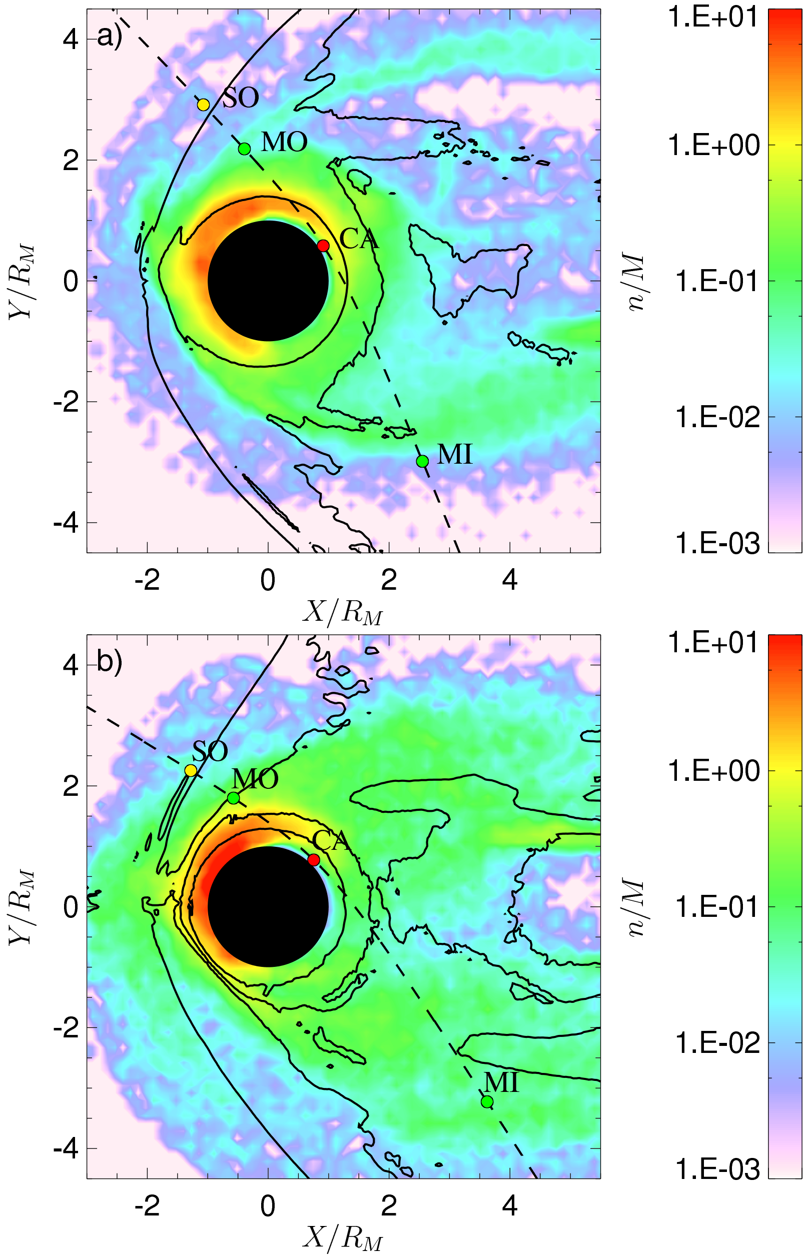

Figure 7.1: Color representation of sodium ion (Na^+) density in equatorial plane (X,Y). Panels (a) and (b) represent solar wind conditions which we refer to as HYB1 and HYB2, respectively. Dashed line on panels (a) and (b) represent projection of trajectory of M1 and M2 flybys of MESSENGER on equatorial plane, respectively. Colored markers show position of magnetopause inbound (MI), closest approach (CA), magnetopause outbound (MO) and shock outbound (SO) crossings as determined from hybrid simulations. The iso-contours represent constant magnetic field $|B|$ of 1.6 and 5 B_{sw}.

7.3 Results

The spatial distribution of neutral atoms is governed by gravitation and radiation pressure forces as well as the energy distribution and source spatial distribution of releasing processes. In the case of SWS the energy of neutral particle ejecta is high enough to easily escape bounding forces and forms a corona-like envelope. On the other hand, the PSD process releases relatively low energy particles with energy distribution peak at 0.1 eV [*Yakshinskiy and Madey*, 1999]. These particles are bound by gravitational force to the planetary surface and form a thin layer with a maximal altitude of ≈ 80 km at the nose of the planet. This layer is a rich source of ions because of the increased chance of photoionization. Ionized particles are governed only by electromagnetic fields and so the orientation of the IMF plays a dominant role in determining the ion distribution.

Figure 7.1 presents the spatial distribution of sodium ions (Na^{+}) in the equatorial plane. Panels (a) and (b) represent HYB1 and HYB2 simulation results respectively, with MESSENGER trajectories from the first and second flybys represented by a dashed line. The color markers MI, CA, MO and SO represent magnetopause inbound, closest approach, magnetopause outbound and shock outbound, respectively (as observed from the hybrid simulation). The color scale represents sodium ion density scaled in arbitrary units defined above. The axes are scaled to the radius of Mercury R_M with the Sun in the -X direction. The solid line contours represent constant magnitude of the magnetic field of 1.6 B_{sw} and 5 B_{sw} for easy identification of magnetosphere structure.

As a result of the different orientation of the IMF, sodium distribution in the equatorial plane in Figure 7.1 differs between HYB1 and HYB2. Particles easily leak upstream at the subsolar point in the case of south-pointing IMF as seen from panel (b) of Fig. 7.1. The prominent feature of northward pointing IMF in panel (a) corresponds to an accumulation of sodium ions in the downstream predawn magnetosphere sector. This is in agreement with observations from the FIPS instrument during the first flyby. Particles near closest approach have average energy per bin of 3 keV. On the other hand, a high energy ion population, with average energy 10 keV, can be observed upstream of the magnetopause. This distribution of energetic ions is different for HYB1 and HYB2; for north pointing IMF (i.e. HYB1) energetic particles are accumulated at the dawn flank whereas for south pointing IMF they are present from the dayside to post-dusk sector.

In general, ionized particles are carried westward and are transported to the nightside where they can escape into the tail or back-scatter on the surface. Note the differences for both cases of IMF in Fig 7.1. For northward B_z we can clearly see that the ion population is confined downstream of the magnetopause. On the other hand, southward pointing IMF allows particles to escape at the nose of the magnetosphere due to reconnection.

Ions released by SWS are originally localized at auroral mid-latitude regions. The velocity distribution points in the direction normal to the surface and thus the parallel velocity with respect to the local magnetic field is greater than the perpendicular velocity. Such particles are partially trapped and undergo mirror motion with a relatively high latitude mirror point. The remaining particles escape and are lost to the tail where they follow a meandering motion.

In the case of PSD, particles have rather small energy after being released and form a thin layer of neutral particles on the dayside which acts as a source of photo-ions. Ionized particles have small parallel velocity as compared to their perpendicular velocity and thus PSD ions equatorialy mirror before back-scattering to the surface. Because of the different removal mechanism, PSD is responsible for filling lower altitudes with low energy particles. SWS, on the other hand, is most likely filling the higher altitude regions.

Figure 7.2 represents a virtual flyby through simulated data. Panels (a) and (b) represent the two study cases HYB1 and HYB2 that correspond approximately to the solar wind conditions appropriate to M1 and M2 flybys of MESSENGER, respectively. The error bars represent one standard deviation of simulated data using a sequence of time slices of EM fields taken from hybrid model. The fields are taken exactly one gyroperiod apart. The large error bars in Fig. 7.2 reveal the importance of wave-particle interactions in determining the observed sodium density. As expected, the high density region near the closest approach is more susceptible to plasma dynamics. In the near Mercury environment, magnetically trapped particles undergo bouncing motion between conjugate hemispheres while interacting with low frequency waves. These waves have frequency close to the proton gyrofrequency and affect the topology of electromagnetic fields which in turn change the local distribution of sodium ions.

Direct measurements of M1 *Zurbuchen et al.* [2008] reveal several ion density accumulation regions along the flyby trajectory that qualitatively agree with our models: First, increased density in the inbound leg when crossing the magnetopause; second, a gradual increase of density as the spacecraft approaches the planet, followed by a

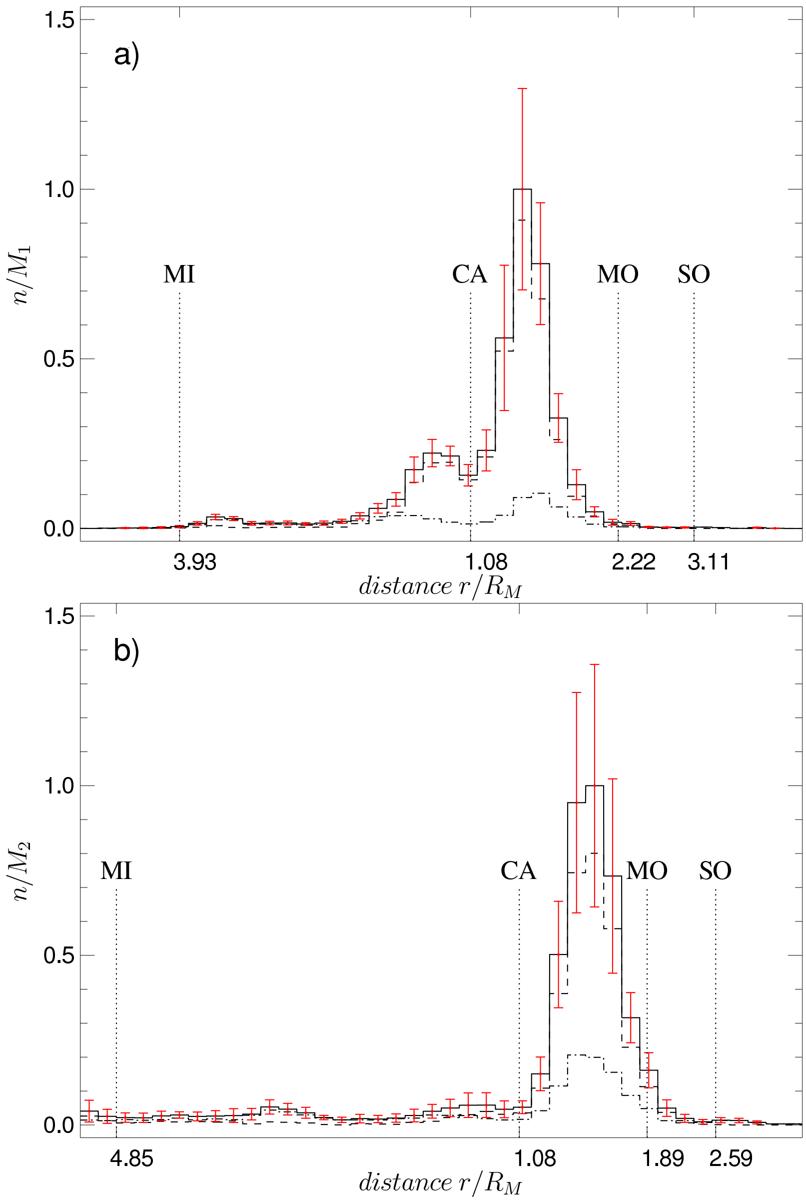

Figure 7.2: Measurements of sodium ion density in arbitrary units of virtual flyby using the trajectory from the first and second flyby of MESSENGER on panel (a) and (b), respectively. Ejecting mechanisms PSD and SWS are represented by dashed and dashed-dotted lines, respectively, and the sum of both is represented by the solid line. Locations of magnetopause inbound, closest approach and magnetopause outbound are marked on the figure as MI, CA and MO, respectively. Scaling factors $M_{1,2}$ = 13.7 and 4.7 ions/cc for the first and second flyby, respectively.

sudden decrease before crossing the CA. This decrease is due to the large particle gyroradius, which diffuses particles to higher L-shell as they drift into the night sector. Diffusion is likely responsible for density depletion near the noon sector of the planet, as seen in the vicinity of closest approach in the FIPS measurements as well as our virtual flyby.

7.4 Conclusions

Simulations reveal that in the near Mercury environment, photon stimulated desorption (PSD) is the dominant source of the exosphere (c.f. Fig. 7.2). This results from a relatively high density source of low energy neutral particles on the dayside, although we note that thermal desorption that is difficult to quantify with our model may reduce the PSD process. Photoionization on the dayside acts as a fountain which replenishes the exosphere with new Na^+ ions. On the other hand, SWS ejects particles from a narrow band of high latitudes in the auroral region that fill the tail of Mercury with new Na^+.

By comparing numerical results with data from the MESSENGER FIPS instrument published by *Zurbuchen et al.* [2008], we conclude that our numerical studies are in good agreement compared to M1, where a comparison can be made. Density accumulation occurs downstream of the dusk magnetopause, with maximum density occurring after closest approach as MESSENGER moves outbound toward the magnetopause, which is located in the dawn sector of the equatorial plane. Peak ion densities along the MESSENGER orbit correspond to ~ 14 and 5 ions cm^{-3} in our model for the first and second flyby, respectively, if the rate of 5×10^{24} Na neutrals s^{-1} is assumed for PSD. The model then predicts ~ 0.3 and 0.8 cm^{-3} ion densities at the outbound magnetopause for HYB1 and HYB2, respectivelly. Such high ion densities may explain the boundary layer feature that corresponds to the diamagnetic decrease of the magnetic field observed by *Slavin et al.* [2008, 2009] during MESSENGER flybys. The dynamic nature of our simulations reveals that plasma within 1.3 R_M radius is affected by wave-particle interactions. This region ranges from the predawn to postnoon sector.

Several factors potentially contribute to differences between the observations of *Zurbuchen et al.* [2008] and our results: First, because the resolution of the "in situ" data measurements is somehow small due to the selected bin size, it is difficult to localize the peaks and valleys. Second, several species are included with rather large

m/q range as compared to our results, where we include only sodium ions. Third, limitations of the FIPS instrument caused by instrument orientation, and the fact that it is on the sun shaded side of the spacecraft. Also, we include a full spectrum of ion energies, whereas FIPS is limited by its energy range sensitivity. The energy sensitivity will play an important role in the regions where low energy ions dominate such as downstream of the magnetopause on the portion of the outbound leg.

Bibliography

Broadfoot, A. L., D. E. Shemansky, and S. Kumar, Mariner 10: Mercury Atmosphere, *Geophys. Res. Lett.*, *3*, 577–580, 1976.

Burger, M. H., R. M. Killen, R. J. Vervack Jr., E. T. Bradley, W. E. McClintock, M. Sarantos, M. Benna, and N. Mouawad, Monte Carlo modeling of sodium in Mercurys exosphere during the first two MESSENGER flybys, *Icarus*, *209*, 63–74, 2010.

Delcourt, D. C., S. Grimald, F. Leblanc, J.-J. Berthelier, A. Milillo, A. Mura, S. Orsini, and T. E. Moore, A quantitative model of the planetary Na+ contribution to Mercury's magnetosphere, *Ann. Geophys.*, *21*, 1723–1736, 2003.

Johnson, R. E., F. Leblanc, B. V. Yakshinskiy, and T. E. Madey, Energy distributions for desorption of sodium and potassium from ice: The Na/K ratio at Europa, *Icarus*, *156*, 136–142, 2002.

Killen, R. M., M. Sarantos, A. E. Potter, and P. Reiff, Source rates and ion recycling rates for Na and K in Mercury's atmosphere, *Icarus*, *171*, 1–19, 2004.

Milillo, A., S. Orsini, D. Delcourt, E. Kallio, R. M. Killen, H. Lammer, F. Leblanc, S. Massetti, A. Mura, P. Wurz, S. Barabash, G. Cremonese, I. A. Daglis, E. D. Angelis, A. M. D. Lellis, S. S. Livi, and V. Mangano, Surface-exosphere-magnetosphere system of Mercury, *Space Sci. Rev.*, *117*, 397–443, 2005.

Mura, A., A. Milillo, S. Orsini, and S. Massetti, Numerical and analytical model of Mercury's exosphere: Dependence on surface and external conditions, *Plan. Space Sci.*, *55*, 1569–1583, 2007.

Ness, N. F., K. W. Behannon, R. P. Lepping, Y. C. Whang, and K. H. Schatten, Magnetic Field Observations near Mercury: Preliminary Results from Mariner 10., *Science*, *185*, 151–60, 1974.

Paral, J., P. M. Trávníček, K. Kabin, R. Rankin, and T. H. Zurbuchen, Spatial distribution and energy epectrum of heavy ions in the Hermean magnetosphere with applications to MESSENGER flybys, *Adv. in Geosci.*, *15*, 1–16, 2009.

Paral, J., P. M. Trávníček, R. Rankin, and D. Schriver, Sodium ion exosphere of Mercury during MESSENGER flybys, *Geophys. Res. Lett.*, *37*, L19,102, 2010.

Sarantos, M., J. A. Slavin, M. Benna, S. A. Boardsen, R. M. Killen, D. Schriver, and P. M. Trávníček, Sodium-ion pickup observed above the magnetopause during MESSENGER's first Mercury flyby: Constraints on neutral exospheric models, *Geophys. Res. Lett.*, *36*, L04,106, 2009.

Slavin, J. A., B. J. Anderson, M. H. Acuña, D. N. Baker, M. Benna, G. Gloeckler, R. E. Gold, G. C. Ho, R. M. Killen, H. Korth, R. L. McNutt, S. M. Krimigis, L. R. Nittler, J. M. Raines, S. C. Solomon, D. Schriver, P. M. Trávníček, R. D. Starr, T. H. Zurbuchen, and Others, Mercury's Magnetosphere After MESSENGER's First Flyby, *Science*, *321*, 85–89, 2008.

Slavin, J. A., B. J. Anderson, D. N. Baker, T. H. Zurbuchen, S. M. Krimigis, M. H. Acuña, M. Benna, S. A. Boardsen, G. Gloeckler, R. E. Gold, and Others, MESSENGER observations of Mercury's magnetosphere during northward IMF, *Geophys. Res. Lett.*, *36*, L02,101, 2009.

Slavin, J. A., R. P. Lepping, C.-C. Wu, B. J. Anderson, D. N. Baker, M. Benna, S. A. Boardsen, R. M. Killen, H. Korth, S. M. Krimigis, W. E. McClintock, R. L. McNutt, M. Sarantos, D. Schriver, S. C. Solomon, P. M. Trávníček, and T. H. Zurbuchen, MESSENGER observations of large flux transfer events at Mercury, *Geophys. Res. Lett.*, *37*, L02,105, 2010.

Trávníček, P. M., P. Hellinger, and D. Schriver, Structure of Mercury's magnetosphere for different pressure of the solar wind: three dimensional hybrid simulations, *Geophys. Res. Lett.*, *34*, L05,104, 2007.

Yakshinskiy, B. V., and T. E. Madey, Photon-stimulated desorption as a substantial source of sodium in the lunar atmosphere, *Nature*, *400*, 642–644, 1999.

Zurbuchen, T. H., J. A. Slavin, J. M. Raines, G. Gloeckler, S. M. Krimigis, P. L. Koehn, R. M. Killen, A. L. Sprague, R. L. McNutt, and S. C. Solomon, MESSEN-

GER observations of the composition of Mercury's ionized exosphere and plasma environment., *Science*, *321*, 90–2, 2008.

Chapter 8

Conclusions

The primary objective of this thesis was to quantify dynamic interactions of the solar wind with the planet Mercury at the spatial scales where the ion-gyroradius effects are important. To achieve this goal numerical modelling techniques were used. A considerable amount of computer resources are available to researchers through the Westgrid supercomputer network (www.westgrid.ca) of western universities in Canada. Also, technical support offered by the University of Alberta is at the level which allowed us to attempt the development of more technically sophisticated models than otherwise possible. Thus, a secondary objective was to develop numerical models that are efficient in utilizing HPC computer resources to achieve the most realistic description of the plasma. In this work we choose to study the planet Mercury because of its importance and because the size of the planet and the strength of the intrinsic magnetic field is just right to fit entirely inside of a simulation box. At the same time, the orientation and the topology of the field is the same as the field of Earth only scaled down by a factor of 8. The similar characteristics allow us to generalize our findings to Earth. The lack of an ionosphere at Mercury gives an insight into what degree its presence is important in the terms of global dynamic processes of solar wind interaction. A perfect timing of NASA's MESSENGER mission provided us with a wealth of in situ measurements that was a very important aspect in choosing Mercury for our project.

Two numerical models were developed with the objectives stated above. The first numerical model traces particle trajectories by solving the Lorentz force equation. The code is a continuation of the work started during my masters program. The model requires two different inputs: static electric and magnetic fields for force evaluation; and initial positions and velocities of all particles. After the initialization, the code traces particles in time without a feedback to the fields, and periodically stores the moments of the distribution function. We employed the model to study the dynamic processes in Mercury's exosphere - a comet like cloud of neutrals and ionized species which originated mostly from regolith of the planet through sputtering. Several physical processes contribute to the formation of the exosphere, but the most important are solar wind sputtering and photo-stimulated desorption. We implemented a model which can vary the spatial distribution of particle flux from the planet, particle velocity distribution, temperature and bulk velocity. By using current research findings on sputtering processes forming the exosphere of Mercury, and data observations from the first flyby of MESSENGER, we reconstructed the exosphere numerically and compared the results with real observations. Our findings enabled us to explain the importance of different sputtering mechanisms from the perspective of spatial distribution and energy content. The conclusions of our work also contributed to understanding of the limitations of the instruments on board MESSENGER. The exosphere consist of many ion species but our model studied only ionized sodium Na^+ which is the most abundant. The importance of exosphere in the dynamics of the planet's interaction with the solar wind was already confirmed by other publications. It generates a layer of cold plasma with non-negligible density.

The second model is a self-consistent kinetic description of plasma which allows multiple ion species. All ions are treated using a particle-in-cell method and electrons are treated as a charge neutralizing fluid described by a momentum equation. This approach is also called a hybrid model for mixing together two different plasma descriptions. The advantage is a physically more correct treatment of ions which include a wide range of wave-particle interactions and gyro-radius effects. At the same time, it allows us to lower the requirements on computer resources because of the simplified description of electrons. Because the model is very complex, we spent a considerable amount of time testing various physical properties and so we devoted an entire chapter to the results. These include behavior under unstable conditions, like anisotropy micro-instabilities, which can be predicted to a certain degree analytically and using linear kinetic theory. The hybrid model can run on parallel computer architectures partially thanks to collaboration with IBM T.J. Watson Research Centre. IBM provided us with access to their BlueGene/P supercomputer and expertise in code optimization for high performance computers. We set up the code to model interaction of solar wind with a dipole moment placed inside of a spherical conductor. The parameters, like strength of the dipole and size of the sphere, are consistent with the parameters reported by NASA's MESSENGER mission during the third flyby. After more than a year of MESSENGER surveying the planet Mercury, the data suggest a clear dawn-dusk asymmetry in Kelvin-Helmholtz observations at the magnetopause boundary. The findings were surprising because at Earth, KHI observations are reported at both flanks with approximately the same probability. We used the data from our global model of Mercury to explain the source of asymmetry. Because of the small size of the magnetosphere, kinetic effects and the finite gyroradius become important. The asymmetry is a result of force imbalance at the magnetopause boundary which controls the competition between Kelvin-Helmholtz and Rayleigh-Taylor (RT) instabilities. A dusk-to-dawn convection electric field, together with gradient of pressure, acts in the same direction at dawn and triggers a RT-like instability to disrupt laminar flows required by KHI.

Future research may take different directions but we outline only two imminent goals: improvements to the code and further analysis of the data acquired till now. The implementation of the parallel scheme lacks a load balancing capability that would speed up the execution of the global model. For example, the accumulation of density at the nose of the magnetosphere inevitably slows down the simulation because the processors assigned to that location require more processing time. Although the speed of the code is not optimal, it has produced already a wealth of data. We only analyzed a small fraction of information stored in the data files by visually inspecting the output. A single simulation run produces more than 200 GB of data, which contain information about temporal and spatial distribution of output variables $(B, E, n,..)$ with high precision. Analysis of data in the frequency domain could reveal other unexpected discoveries. For example, analysis of shock wave formed as a response of solar wind and Mercury's magnetic field.